CR:FORSTERITE LASER FREQUENCY COMB STABILAZATION AND DEVELOPMENT OF PORTABLE FREQUENCY REFERENCES INSIDE A HOLLOW OPTICAL FIBER.

by

RAJESH THAPA

M.S., Kansas State University, USA, 2005
M.Sc. Tribhuvan University, NEPAL, 1998

AN ABSTRACT OF A DISSERTATION

submitted in partial fulfillment of the requirements for the degree

DOCTOR OF PHILOSOPHY

Department of Physics
College of Arts and Sciences

KANSAS STATE UNIVERSITY
Manhattan, Kansas

2008

Abstract

We have made significant accomplishments in the development of portable frequency standard inside hollow optical fibers. Such standards will improve portable optical frequency references available to the telecommunications industry. Our approach relies on the development of a stabilized Cr:forsterite laser to generate the frequency comb in the near-IR region. This laser is self referenced and locked to a CW laser which in turn is stabilized to a sub-Doppler feature of a molecular transition. The molecular transition is realized using a hollow core fiber filled with acetylene gas. We finally measured the absolute frequency of these molecular transitions to characterize the references. In this thesis, the major ideas, techniques and experimental results for the development and absolute frequency measurement of the portable frequency references are presented.

A prism-based Cr:forsterite frequency comb is stabilized. We have effectively used the prism modulation along with power modulation inside the cavity in order to actively stabilize the frequency comb. We have also studied the carrier-envelope-offset frequency (f_0) dynamics of the laser and its effect on laser stabilization. A reduction of f_0 linewidth from ~2 MHz to ~20 kHz has also been observed. Both our in-loop and out-of-loop measurements of the comb stability showed that the comb is stable within a part in 10^{11} at 1-s gate time and is currently limited by our reference signal.

In order to develop this portable frequency standard, saturated absorption spectroscopy is performed on the acetylene $\nu_1 + \nu_3$ band near 1532 nm inside different kinds of hollow optical fibers. The observed linewidths are a factor 2 narrower in the 20 μm fiber as compared to 10 μm fiber, and vary from 20-40 MHz depending on pressure and power. The 70 μm kagome fiber shows a further reduction in linewidth to less than 10 MHz. In order to seal the gas inside the hollow optical fiber, we have also developed a technique of splicing the hollow fiber to solid fiber in a standard commercial arc splicer, rather than the more expensive filament splicer, and achieved comparable splice loss.

We locked a CW laser to the saturated absorption feature using a Frequency Modulation technique and then compared to an optical frequency comb. The stabilized frequency comb, providing a dense grid of reference frequencies in near-infrared region is used to characterize and measure the absolute frequency reference based on these hollow optical fibers.

CR:FORSTERITE LASER FREQUENCY COMB STABILAZATION AND DEVELOPMENT OF PORTABLE FREQUENCY REFERENCES INSIDE A HOLLOW OPTICAL FIBER.

by

RAJESH THAPA

M.S., Kansas State University, USA, 2005
M.Sc. Tribhuvan University, NEPAL, 1998

A DISSERTATION

submitted in partial fulfillment of the requirements for the degree

DOCTOR OF PHILOSOPHY

Department of Physics
College of Arts and Sciences

KANSAS STATE UNIVERSITY
Manhattan, Kansas

2008

Approved by:

Major Professor
Kristan Corwin

Abstract

We have made significant accomplishments in the development of portable frequency standard inside hollow optical fibers. Such standards will improve portable optical frequency references available to the telecommunications industry. Our approach relies on the development of a stabilized Cr:forsterite laser to generate the frequency comb in the near-IR region. This laser is self referenced and locked to a CW laser which in turn is stabilized to a sub-Doppler feature of a molecular transition. The molecular transition is realized using a hollow core fiber filled with acetylene gas. We finally measured the absolute frequency of these molecular transitions to characterize the references. In this thesis, the major ideas, techniques and experimental results for the development and absolute frequency measurement of the portable frequency references are presented.

A prism-based Cr:forsterite frequency comb is stabilized. We have effectively used the prism modulation along with power modulation inside the cavity in order to actively stabilize the frequency comb. We have also studied the carrier-envelope-offset frequency (f_0) dynamics of the laser and its effect on laser stabilization. A reduction of f_0 linewidth from ~2 MHz to ~20 kHz has also been observed. Both our in-loop and out-of-loop measurements of the comb stability showed that the comb is stable within a part in 10^{11} at 1-s gate time and is currently limited by our reference signal.

In order to develop this portable frequency standard, saturated absorption spectroscopy is performed on the acetylene $\nu_1 + \nu_3$ band near 1532 nm inside different kinds of hollow optical fibers. The observed linewidths are a factor 2 narrower in the 20 μm fiber as compared to 10 μm fiber, and vary from 20-40 MHz depending on pressure and power. The 70 μm kagome fiber shows a further reduction in linewidth to less than 10 MHz. In order to seal the gas inside the hollow optical fiber, we have also developed a technique of splicing the hollow fiber to solid fiber in a standard commercial arc splicer, rather than the more expensive filament splicer, and achieved comparable splice loss.

We locked a CW laser to the saturated absorption feature using a Frequency Modulation technique and then compared to an optical frequency comb. The stabilized frequency comb, providing a dense grid of reference frequencies in near-infrared region is used to characterize and measure the absolute frequency reference based on these hollow optical fibers.

Table of Contents

List of Figures

List of Tables

Acknowledgements

My deepest gratitude is due to my main supervisor, Dr. Kristan L. Corwin, for giving me the opportunity to participate in a wonderful research project. She has been an excellent mentor, insightful researcher and good friend too. She has always had time to share small and big, happy and sad things with me. This dissertation could not have been completed without her supervision, encouragement and guidance. I would like to thank you the members of my advisory committee, Dr. Zhengu Chang, Dr. Viktor Chikan, Dr. Akira Tokuhiro, Dr. Brian Washburn and Dr. Larry Weaver. I would especially like to thank Dr. Washburn for his great help and co-ordination in laser related matter in lab. Dr Weaver has been great help to me in theoretical aspects of saturation spectroscopy. I am very grateful to Prof. Dean Zollman who was very supportive when I needed help. My thanks to Jane Peterson and Peggy Matthews who were very helpful with office work.

I owe my special thanks to the people who worked closely with me within last 5 years: Mohammad Faheem, Andrew Jones, Kevin Knabe, Jin Kang Lim, Dr. Ahmer Naweed and Dr. Karl Tillman. I especially like to acknowledge Kevin Knabe and Andrew Jones who made the setup for Frequency Modulation Spectroscopy possible.

I want to thank Mike Wells and the J. R. Macdonald Lab staff for help building the experiment. We would also like to thank you Dr. Kurt Vogel for suggesting the AOM and sending us a complete layout of the frequency modulation spectroscopy, S. Diddams, K. Read, and H. Kapteyn for their efforts in designing the laser, N. Newbury, Sarah Gilbert, Dirk Müller, and Bill Swann for their helpful discussion, and J. W. Nicholson and M. F. Yan for providing us with highly non-linear fiber with which to produce the supercontinuum spectrum, Phil Light, Francois Couny, Fetah Benabid and University of Bath for providing Kagome fiber.

We gratefully acknowledge funding from the Air Force Office of Scientific Research, the National Science Foundation CAREER and EPSCoR programs, and Kansas Technology Enterprise Corporation.

Finally, I express my sincere thanks to my wife Sunita for her continuous support and co-operation throughout my graduate study and my little son Samyak where I see my own reflection.

Dedication

I dedicate this work to my parents:

my father **Bharat Bahadur Thapa** and my mother **Shanti Devi Thapa**

and to my family:

my wife **Sunita Parajuli** and my little son **Samyak Raj Thapa**.

CHAPTER 1 - Introduction and background

1.1. Introduction

Interest in time has evolved as a part of human civilization. Until the last centuries, only a small subset of lucky people got some "leisure time" to treat time as an experimental parameter. In 1967, the General Conference on Weights and Measures defined one second as the duration of 9 192 631 770 periods of the radiation corresponding to the transition between the two hyperfine levels of the ^{133}Cs atom. The definition of time can be used to derive the unit of frequency, the Hertz. The future of time and frequency metrology was changed fundamentally by the invention of the laser. The central concept of these advances is that a pulse train generated by a mode-locked laser has a frequency spectrum which consists of a series of discrete, regularly spaced sharp lines known as a frequency comb. In 2005, John L. Hall and Theodor W. Hänsch shared half the Nobel Prize for their contributions to the development of laser-based precision spectroscopy, including the optical frequency comb technique.

These frequency combs now can measure frequency stability of less than 1 part in 10^{16} [1-3] at 1s of averaging time whereas relative uncertainties of the combs can be as good as 1 part in 10^{20} [4]. Now we are in an era of such precise and accurate capability to measure time and frequency that one may be able to see slow variation of the fundamental constants, if there is any, over time and may well be able to test fundamental physical laws more accurately that eventually will have long term impact on the development of science and technology. Additionally, frequency comb techniques provide a key to extreme nonlinear optics, ultrafast science, and attosecond science, an emerging field in physics, by offering control of the electric field of the ultrafast laser. However, these precise and accurate measurements of optical frequency are not yet very useful for commercial and military applications, including optical telecommunications, because of their cost, lack of portability, and requirement for extremely accurate and stable references. The telecom industry still relies on portable optical frequency references with uncertainties of $\sim 5\times10^{-7}$. We investigate a portable frequency reference based on acetylene-filled optical photonic band gap fiber to provide uncertainties with at least one to two orders of magnitude better. We have also developed a frequency comb in near-IR region in order to measure and characterize the absolute frequencies of these portable frequency references.

Any device to measure time (or frequency) needs a reference element such as the quartz crystal in a wrist watch. Frequency standards are based on crystal or atomic oscillators. A crystal oscillator such as quartz has good short term stability (~1 s) but poor long term stability. These crystals produce RF signals that serve as the standard. Atomic transitions in oscillators such as rubidium and cesium also produce RF signals and they offer higher performance over quartz crystals. There are many atomic oscillators such as neutral calcium and neutral ytterbium which produce optical signals instead of RF signals. These optical standards offer much higher improvement over their RF counterparts by virtue of much higher oscillation frequencies, ($\nu_{optical}/\nu_{rf} \approx 10^6$). But these optical standards are very expensive and owned by very few laboratories or standards organizations. In our laboratory, we use a GPS-disciplined Rb clock which takes advantage of short terms stability of Rb and the long term stability of the GPS satellite network of Cs atomic clocks. For a portable frequency comb, one can use the GPS-disciplined clock which needs to be in satellite contact all the time and requires several hours of continuous connection to achieve maximum stability and accuracy. In contrast, an on-board CW laser locked to the molecular transition can offer good short term and long term stability without access to any external reference or source.

Table 1.1. Stability of crystal and atomic standard references.

Oscillator Type	Stability in 1 s	Aging/year	Cost	Portable?
Temperature-compensated quartz oscillator	1×10^{-9}	5×10^{-7}	$100	Yes
Microcomputer-compensated quartz oscillator	1×10^{-10}	5×10^{-8}	$1000	Yes
Oven-controlled quartz oscillator	1×10^{-12}	5×10^{-9}	$2000	Yes
Rubidium	5×10^{-11} to 5×10^{-12}	2×10^{-10}	$5000	Yes
Cesium	5×10^{-11} to 5×10^{-12}	None	$50,000	Yes
Hydrogen maser	1×10^{-12}	1×10^{-13}	$250,000	No
Cryogenic sapphire	~2×10^{-16}	$<10^{-13}$	~$250,000	No
Calcium optical clock transition	1×10^{-16}	?	>$500,000	No

The telecommunication industry uses absorption spectra of different molecular gases as optical frequency references (Fig 1.1) [5-8]. Some of these molecular gases have served as a

standard reference material (SRM). Some of them have been created and characterized by the National Institute of Science and Technology (NIST).

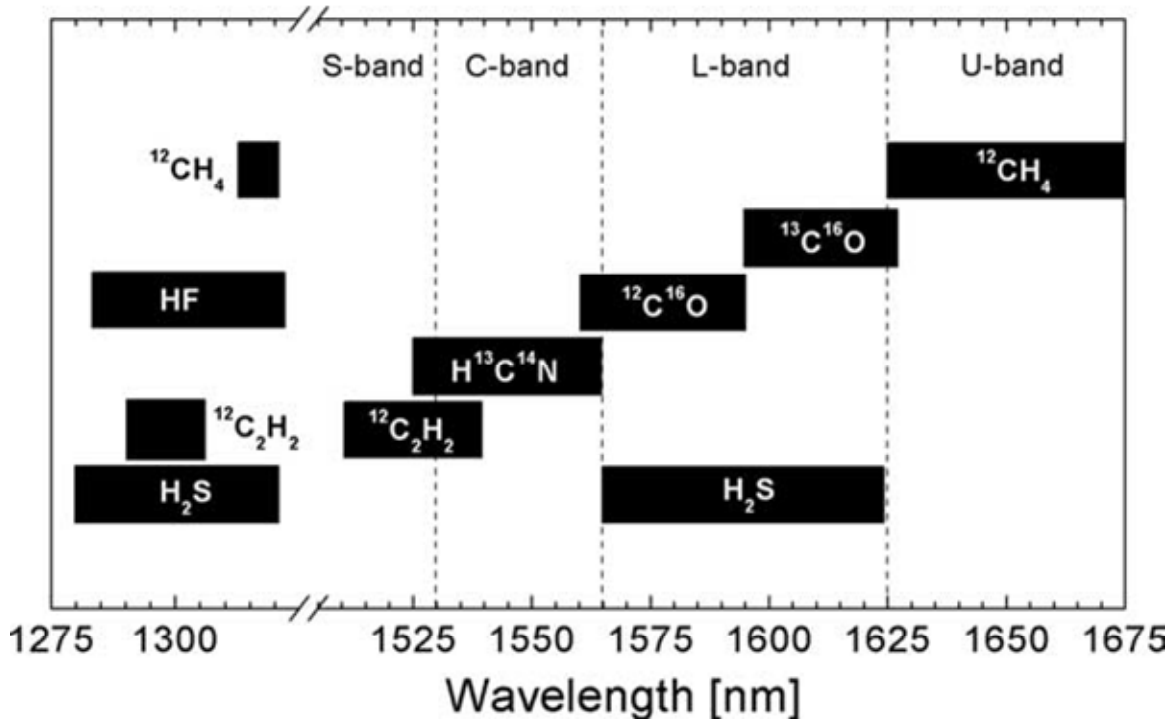

Figure 1.1. Common gases used by international telecommunication union (ITU) for referencing the wavelength used [9].

Currently, there are several methods to precisely measure frequency and wavelength for metrology purposes. The Burleigh Wavemeter [10] is a travelling Michelson based interferometer that offers the best commercially available CW laser wavelength measurement. This method can give uncertainty of ~40 MHz at 1.5 μm (~200 THz) wavelength. Other commercial devices are optical spectrum analyzers (OSA) which are basically diffraction-grating based spectrometers. Some of the high-end spectrometers contain built-in calibration in the form of a glass cell filled with a reference gas such as acetylene ($^{12}C_2H_2$) [6, 7], hydrogen cyanide ($H^{13}C^{14}N$) [5, 11], and carbon monoxide ($^{12}C^{16}O$ and $^{13}C^{16}O$) [8]. These molecular gas filled cells are also called standard reference materials (SRM) and can have intrinsic frequency uncertainty of ~13 MHz on some lines and ~130 MHz on most features. These glass cells are generally filled to pressures of ~50 Torr at which pressure broadening and Doppler broadening of around ~500 MHz are dominant factor for frequency uncertainty. Relative accuracies of some of the best commercially systems are shown in Table 1.2.

Table 1.2. Relative accuracy of some of the best commercially available systems.

Product	Accuracy at 1500 nm		Technology
Agilent 8191A [12] All-parameter Analyzer	± 1.5 pm (typ) ± 4.0 pm (spec)	± 200 MHz ± 530 MHz	NIST HCN cell
Agilent 8614xB OSA [13]	± 10.0 pm	±1300 MHz	NIST HCN cell
ANDO 6317B OSA [14]	± 20.0 pm	±2600 MHz	NIST HCN cell
EXFO/Burleigh [10] WA-1500 Wavemeter	± 0.3 pm (2σ)	± 40 MHz	I_2-stabilized HeNe laser
Precision Photonics TLSA1000 [15]	± 0.4 pm (rms)	± 50 MHz	NIST HCN cell
NIST SRM's [5, 6] [16]	± 0.1 pm C_2H_2 ± 0.4 pm HCN	± 13 MHz ± 53 MHz	Molecular abs.

As I mentioned above, the development of frequency comb metrology dramatically improved the precision and accuracy of optical frequency in research laboratories. The phase stabilized frequency comb can easily measure optical frequency eight orders of magnitude better than the best commercially available system. Ti:sapphire laser frequency combs are the most researched and well-developed system to which all other combs are compared. Ti:sapphire laser combs can produce an optical or RF signal with more precision than the cesium standard so the best method to characterizing a Ti:sapphire comb is to compare with another Ti:sapphire comb. So the best reported optical to optical comparasion gives a relative frequency uncertainty of 8×10^{-20} [4] between two optical frequencies generated by two separate Ti:sapphire frequency combs locked to the same optical reference. But the Ti-sapphire laser based frequency comb does not extend into the near-IR region. Thus, the Ti:sapphire laser system is not convenient for frequency metrology near 1550 nm. While 1550 nm can be frequency doubled into the Ti:sapphire band, such doubling requires significant power and stability as well as availability of bandwidth requirement on the doubling crystal to cover the entire C_2H_2 spectrum from 1510 to 1540 nm. Both diode-pumped solid state laser systems and fiber-based systems can fulfill this criterion and each type has their own associated advantages and disadvantages. For example, all fiber based systems offer the potential for compact and robust systems requiring little fine tuning with very reliable operation at modest costs. But there are currently inherent limitations in the repetition rates they can achieve because of the need to exactly manage the fiber lengths

necessary for mode-locked operation. Diode pumped solid state systems on the other hand can overcome this issue as they are primarily free-space propagating systems. Therefore, we use a Cr:forsterite laser as an alternative laser source. Cr:forsterite (Cr^{+4}:Mg_2SiO_4) readily covers the 1150-1350 nm region and is capable of producing 14 fs pulses [17] at relatively high output powers. Consequently its second harmonic partially fills the gap between the fundamental and second harmonic of Ti:sapphire and enables it to bridge the gap between Ti:sapphire combs and fiber combs [18]. Furthermore, the supercontinuum produced by its pulse propagation through highly nonlinear fiber (HNLF) can readily span an optical octave often ranging from 1000 nm to 2300 nm.

Although very high frequency references already exist in a few laboratories across the world, robust and portable frequency references have a resolution of ~100 MHz, and commercially available wavelength measurement devices are limited to about 10 - 100 MHz in accuracy. In contrast, gas-filled fiber references have the potential to be at least 1 or 2 orders of magnitude more accurate.

These hollow core photonic bandgap fibers (PBGF) allow light to be confined at high intensities in a hollow air or gas-filled region with very low loss [19] and they are extremely portable. These fibers are vastly superior to capillary fibers for small core diameters [20], and have therefore been used in many recent demonstrations of nonlinear light-gas interactions. Examples include gas sensors [21], Raman scattering in hydrogen-filled fiber as a tunable light source [22], and electromagnetically induced transparency (EIT) in PBGF filled with acetylene and rubidium [23-25]. We characterize the accuracy of the gas-filled PBGF cells by locking an extended cavity diode laser to the acetylene absorption feature, and then measure the absolute value of that locked CW laser frequency. We will investigate the shift in the center frequency with temperature, gas pressures, fiber length, laser polarization, and other parameters that may drift during the operation of such a reference. These measurements are initially made on a gas inside the 20 μm fiber core. Now we use much larger core kagome fiber since they offer much narrower transition. To characterize the short-term stability we replace the extended-cavity diode laser with a narrow linewidth fiber laser, commercially available and beat two of the similar system together. To demonstrate the stability of the locked laser, we compare it to a frequency comb from Cr:forsterite laser.

1.2. Thesis outline

We have made significant accomplishment in the development of the portable frequency references. We described the state-of-the art capabilities in many technical areas that form the basis of this thesis. Our approach relies on the development of a stabilized Cr:forsterite laser to generate the frequency comb in near-IR region. This laser is self referenced and locked to a CW laser which is in turn stabilized to a molecular transition. The molecular transition is realized using a hollow core fiber, an extremely portable device. We finally measure absolute frequency of these molecular transitions to characterize of the stability of these references. In this thesis, the major ideas, techniques and experimental result for development and absolute frequency measurement of the portable frequency references are presented.

In Chapter 2, we review historical perspective of Cr:forsterite laser as well as some of the inherent properties of the Cr:forsterite crystal and its overall effect on mode locking. It will then be followed by dispersion of Cr:forsterite crystal, cavity configuration as well as ABCD matrix analysis for the stable mode locking operation.

In Chapter 3, design and building of Cr:forsterite laser stabilization is presented. An overall scheme of control of carrier envelope offset frequency, f_0 and, repetition frequency, f_r of the mode-locked laser using 4 different servo system is discussed. A prism servo inside the laser cavity is one of the unique ways to stabilize the laser. Here we also discuss the dramatic narrowing of the width of the carrier envelope offset frequency by two orders of magnitude.

In Chapter 4, saturation spectroscopy of acetylene inside hollow core fiber is investigated. Larger core fiber gives narrower linewidth and it also offers significant advantage in reduction of background noise of the sub-Doppler feature. We also characterize narrow sub-Doppler features in terms of pressure, power and fiber diameter. Saturation spectroscopy in much larger core, recently developed kagome fiber is also discussed.

In Chapter 5, a new method to splice microstructured fibers with step index single-mode fiber (SMF) is presented. This is an important step to get rid of the vacuum chamber and one step closer to realizing an all fiber setup for the development of portable frequency references. A simplified setup of pump probe spectroscopy by exploiting the reflection of light from spliced interface is also discussed.

In Chapter 6, a common technique, called Frequency Modulation Spectroscopy for frequency stabilization of CW laser is presented. We lock CW laser to peak of the narrow sub-

Doppler feature realized in hollow core fiber. We also beat different kinds of CW laser to characterize the stability of the locked laser. (Note: The particular experimental setup for this FM modulation spectroscopy is done by my colleagues Kevin Knabe and Andrew Jones)

In Chapter 7, the phase stabilized Cr:forsterite frequency comb is used to provide a dense grid of reference frequencies to measure and characterize the absolute frequency of molecular lines of acetylene inside a hollow core optical fiber to develop frequency references in near-IR region. This in fact measures stability of both the comb as well as the CW laser locked to the molecular transition.

CHAPTER 2 - Cr: forsterite laser

2.1. Cr: forsterite laser: a history

Cr:forsterite (Cr^{+4}:Mg_2SiO_4) is a solid state laser material lasing in the range of 1150-1350 nm, which is just above the Ti:sapphire tuning range and important for fiber communication applications. The second harmonic of Cr:forsterite partially fills the gap between the fundamental and second harmonic of Ti:sapphire. Besides allowing access to telecommunication wavelengths. The Cr:forsterite gain medium is of significance due to its relevance to optical coherence tomography [26], biophotonics [27], two-dimensional transillumination imaging, and potentially in two-photon focusing microscopy.

There are several possible gain materials in which chromium plays a role, including Cr:YAG, Cr:forsterite, Cr:LiSaf, Cr:ZnSe and Cr:sapphire. In the beginning it was thought that Cr^{3+} was responsible for the lasing action [28, 29]. However, spectroscopic analysis supported the theory that Cr^{4+} was the lasing ion and showed that the presence of Cr^{3+} in the host lattice actually decreased the efficiency of the laser due to two-photon absorption of the pump wavelength [30, 31]. Lasing action in the Cr^{4+}:forsterite gain material was first reported in 1988 [28, 30, 32] .In Cr^{4+} doped forsterite (Mg_2SiO_4) the lasing transition takes place between the electronic energy levels of the 3d electrons. The active laser ions are not shielded from the surrounding host lattice and, as such, strong electron-phonon coupling will take place and give rise to a broadly tunable output [33]. The output is compatible with telecommunications wavelengths and its gain bandwidth makes it a good alternative to Ti:sapphire systems for longer wavelength configurations. Furthermore, at room temperature Cr^{4+}:forsterite has upper state lifetime of 2.7 μs. This upper-state lifetime is sensitive to temperature and by cooling to liquid nitrogen temperatures (77K) the upper-state lifetime can be increased to 20 μs [34-37]. The thermal load from the pump beam inside the crystal can have a detrimental effect on this duration, because an increase of the crystal temperature causes a decrease in the upper-state lifetime. This necessitates a heat removal mechanism to keep the crystal at a constant temperature.

Mode-locked operation of Cr^{4+}:forsterite in the picoseconds domain (31 ps pulses) was first achieved in 1991 using an intracavity loss modulator in the form of an acousto-optic device [38]. To achieve shorter pulses, passive mode-locking techniques must be used, and in 1992

150 fs pulses from a Cr^{4+}:forsterite laser were realized using additive pulse mode locking [36]. This technique was not pursued further due to the development of Kerr-lens mode locking and semiconductor saturable absorbers. Both of these provide a more versatile and simpler path into the femtosecond domain. The technique of Kerr-lens mode locking initiated by an acousto-optic modulator was used to mode lock a Cr^{4+}:forsterite laser producing pulses initially of 60fs [39] before careful management of the dispersion compensation allowed 36fs [40] pulses to be realised. This mode-locked operation was sustained even after the acousto-optic modulator was turned off indicating that the laser was self-mode-locked [36, 39-42]. Kerr-lens mode locking has also provided the shortest pulses from a Cr4+:forsterite laser, with the crystal cooled to -10 °C and, using a combination of chirped mirrors and prisms to compensate for higher-order dispersion, pulses of 14 fs in duration were produced [17].

The starting and stabilization of Cr:forsterite laser is quite difficult as compared to other solid state lasers. Besides the necessity of heat removal mechanism to increase the life time of the excited states, it was also realized that the low thermal conductivity of the Cr:forsterite gain medium is another drawback to having poor CW laser performance [43]. Thermal conductivity can be dramatically increased by cooling the crystal up to 77K and as much as 3W of average power can be obtained [44]. But the high power CW laser pumping gives rise to the thermal lensing effect [45, 46] and thereby degrades the laser performance. This thermal effect also contributes to increasing the lasing threshold of Cr:forsterite [47-49]. A higher lasing threshold increases the pump power requirement, resulting in a significant increase in the overall system cost and also increases the thermal effects. Moreover, the figure of merit of this material, generally defined as a ratio of absorption at the pump and lasing wavelength, is an order of magnitude lower than that of the Ti:sapphire laser. It is therefore very important to build a very stable and broadband Cr:forsterite laser by careful design and implementation.

Besides being prone to environmental perturbations, thermal lensing arising from poor thermal conductivity of Cr:forsterite, a 20 years history of this material development resulted in a significant progress. Much work has been done with Cr:forsterite active crystals for optimizing laser efficiency and minimizing thermal problems. [47-49]. Very recently, the development of techniques to enable low-threshold operation of end-pumped tunable solid-state lasers has received a great deal of attention in both Ti:sapphire and Cr:forsterite lasers [47, 48, 50-52]. The

most straightforward approach is to lower the laser threshold by employing tighter focusing, smaller crystal size and optimum doping concentration [53].

2.2. Tunable solid-state laser

Solid state laser are categorized into two main classes depending upon the output spectral characteristics: rare-earth ion-doped solid-state laser, and transition metal ion-doped solid-state laser. In the former case the laser active 4f electron is shielded from the surrounding lattice by higher lying electrons which form a closed loop xenon cell with the $5s^2 5p^6$ configuration. This screening greatly reduces electron-phonon coupling resulting in a very weak interaction between the ion and the surrounding lattice. As a result, optical amplification is obtained over a narrow spectral range and the emission wavelengths do not vary significantly in different host media. The best known member of this group is the Nd:YAG laser [54] which can operate at many wavelengths in the near infrared including 946, 1064, and 1319 nm, besides others. In the second group of solid-state lasers, also known as tunable solid-state lasers, the host medium is doped with transition metal ions such as Ni^{2+} , V^{2+}, Co^{2+}, Ti^{3+} , Cr^{3+} , Cr^{4+} and so on. Here, lasing occurs as a result of the transitions between the electronic levels of the 3d electrons. Because the laser active ion is not shielded from the surrounding lattice, strong electron-phonon coupling takes place, giving rise to broadly tunable output. The tuning range of some of the Cr^{4+} doped lasers are given in Table 2.1. (Note: Some of the pictures in Section 2.2 and 2.3 are reproduced with permission from author Alphan Sennaroglu.)

Table 2.1. Tuning range obtained with some of the Cr:doped laser [33]

Cr^{4+} laser	Tuning range (nm)
Cr^{4+}:forsterite	1130-1367
Cr^{4+}:YAG	1309-1596
$Cr^{4+}:Y_3Sc_{0.5}Al_{4.5}O_{12}$	1394-1628
$Cr^{4+}:Y_3ScAl_40_{12}$	1464-1604
$Cr^{4+}:Ca_2Ge0_4$	1348-1482

Let us consider a transition metal ion embedded in a laser crystal. In presence of the vibrating lattice, the total Hamiltonian of the non-ionic system is contribution due to both the static lattice and vibrating lattice,

$$H_T = H_s + H_l \tag{2.1}$$

Here, H_l represent energy due to the vibrating crystal,

$$H_L = V_L + \sum_i \frac{P_i^2}{2M_i} \tag{2.2}$$

where, V_L is the inter-ionic potential energy, P_i, the momentum operator of ion of mass M_i

Let us assume that each ion has one vibrational mode and oscillates around the equilibrium point; in this case, the eigenvalues of H_L can be treated as those of an harmonic oscillator.

$$H_L|n\rangle = E_L|n\rangle$$

$$H_L|n\rangle = h\nu_L(n+\frac{1}{2})|n\rangle$$

Here ν_L is treated as classic frequency of the ionic vibration mode and also referred to as the phonon frequency.

Under Born-Oppenheimer approximation, the electronic and ionic states are treated independently in which case the total energy eigenvalue E_T is given by,

$$E_T = E_e + h\nu_L\left(n+\frac{1}{2}\right) \tag{2.3}$$

This is an important result which shows that the total energy of the ion-lattice system is due to electron-phonon coupling. This can be represented by so called "configuration-coordinate" diagram. In the picture below, the configuration coordinate refers to the distance between the central active ion and the neighboring ion. The lowest eigenenergy of the lattice-ion system is given by, $E_{e1} + \frac{1}{2}h\nu_L$. When the system get excited to higher electronic states with static electron eigenenergy E_{e2}, the coupling between ion-lattice also changes and equilibrium point Q_{01} shifts to Q_{02}. When pump wavelength at λ_P excites the system to ground state to the excited vibronic states $|3\rangle$, the system quickly returns back to upper laser states $|2\rangle$ by emitting phonon, which is referred to as non-radiative decay. From the state $|2\rangle$ ion can make a transition to $|1\rangle$ states either by spontaneous emission or by stimulated emission. Once the system is in the $|1\rangle$ state, it undergoes rapid non-radiative decay to the ground state $|g\rangle$. Typically, non-radiative

transitions occur at a much faster rate. Hence, ions excited to the $|3\rangle$ states rapidly decay to $|2\rangle$ and the population in number $|1\rangle$ is negligible. So vibronic states behave with a very good approximation like a 4-level system and lasing can be obtained at reasonably low pumping levels.

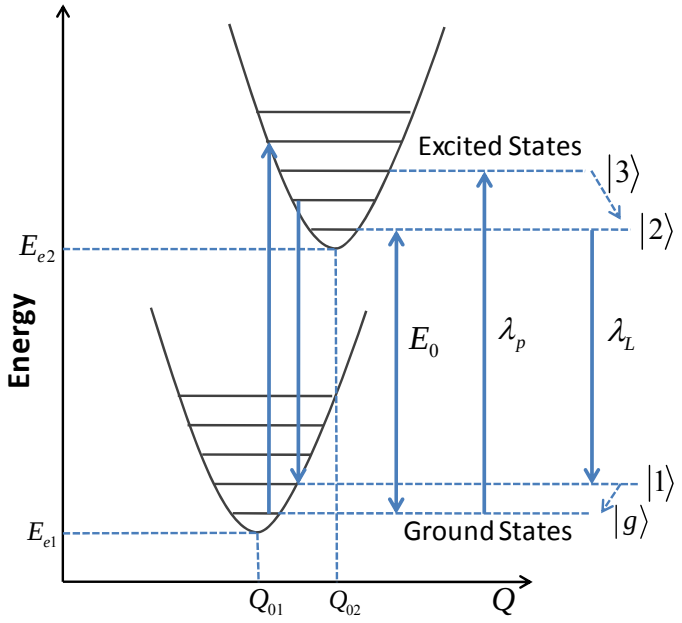

Figure 2.1. Single Configuration coordinate diagram showing coupling between transition metal ion to vibrating lattice. This system can be well approximated as four level systems. Q represents distance between central active ion and the neighboring ion. This Fig. is reproduced from Ref. [33].

The lattice vibration consists of a large number of modes. Every mode has its own phonon frequency. The result of the large number of frequencies is to broaden absorption and emission bands. This effect is more pronounced at higher temperature since the upper vibronic level becomes populated to some degree which gives rise to the transition at different wavelengths. It is shown in the Fig. 2.2 that the emission spectra of Cr^{4+} doped YAG crystal at the temperatures of 293 K is very broad as compare to the temperature at 77 K.

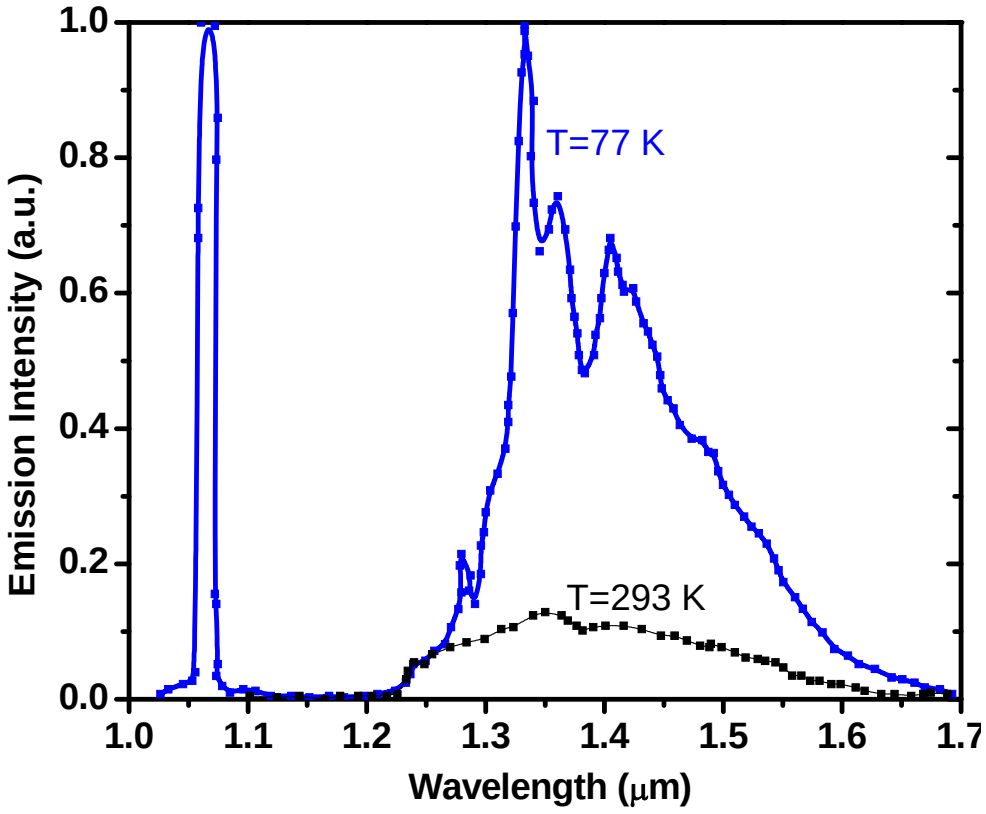

Figure 2.2. Emission spectrum of Cr^{4+} doped YAG at different temperatures [33].

So the electron-phonon interaction enables both the 4-level energy structure and tunability. But it also has some undesirable effect at higher temperature since it gives rise to the non-radiative component of the spontaneous decay between states $|2\rangle$ to $|1\rangle$. The consequence of this is to reduce the population inversion and hence lowers the emission strength. Moreover, the increase in non-radiative decay decreases the efficiency of the gain medium by heating the crystal. For the higher laser performance this heat has to dissipate quickly. Therefore thermal conductivity of the crystal is an important parameter to decide the overall power performance of vibronic lasers such as Ti^{3+}: sapphire and a variety of chromium-doped laser. Sometime we may need to employ cryogenic cooling to get higher laser output. Figure 2.3 below shows the wavelength tuning range of some of the tunable solid state lasers.

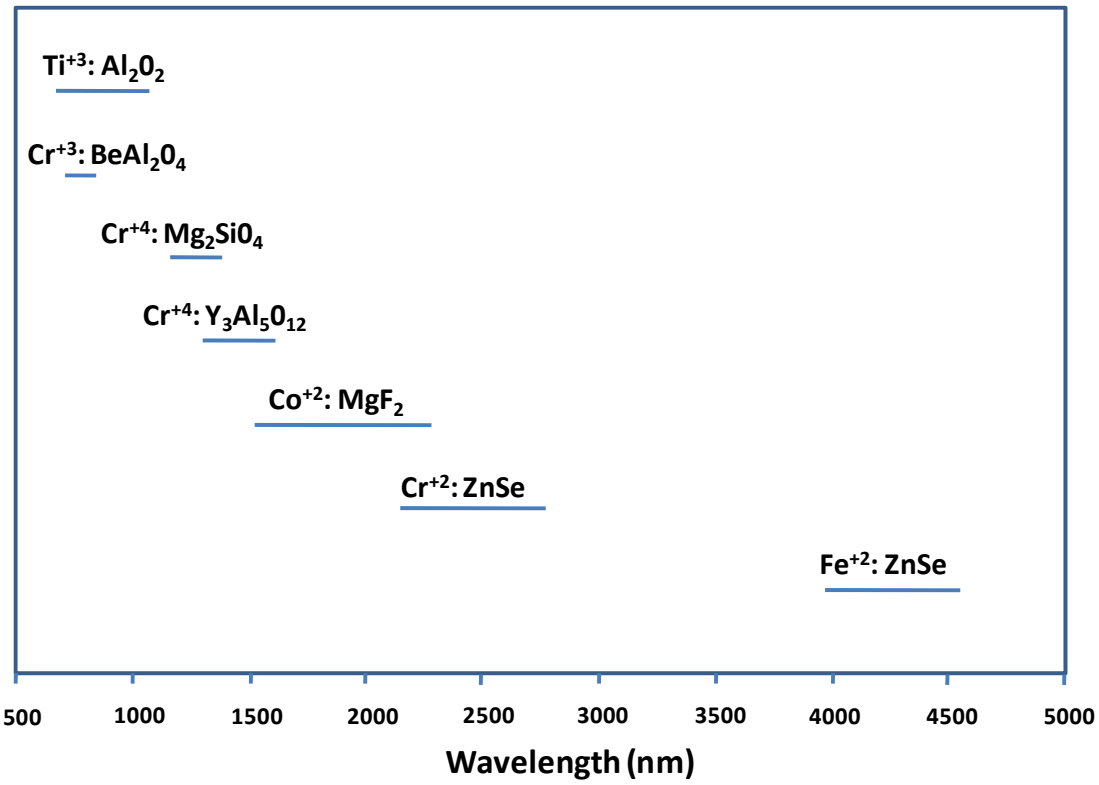

Figure 2.3. Tuning range of some of the tunable solid state lasers. Whole tuning range from 665 nm to 4500 nm is covered by various ion-host combinations. Figure is reproduced from reference [33].

We can see the almost whole tuning range from 665 nm to 4500 nm is covered by using different ion-host combinations. Among these transition metal ion, besides Ti:sapphire, Cr-doped lasers have been extensively studied because of the ionic charges and broad absorption band.

2.3. Characteristic of Cr: forsterite crystal

Cr:forsterite laser is named after the German naturalist Johan Forster. The host material forsterite (Mg_2SiO_4) is a naturally occurring crystals belongs to the orthorhombic class of crystals, commonly known as olivines. Cr:forsterite is a biaxial crystal. The three different crystal axes can be specified according to the lattice constants as the *a* axis 4.76 Å, *b* axis 10.22 Å, and *c* axis 5.99 Å [28]. Here we use the Pbnm crystallographic notation. When the host material forsterite is doped with the chromium ion, Cr^{3+} can substitute for the octahedral coordinated Mg and Cr^{4+} substitute for the tetrahedral coordinated Si [55].

2.3.1. Absorption and fluorescence

The Cr:forsterite laser covers an important wavelength range in near-infrared spectral region from 1100 nm to 1400 nm. Figure below shows the absorption and emission spectra of Cr:forsterite crystal at room temperature [28],

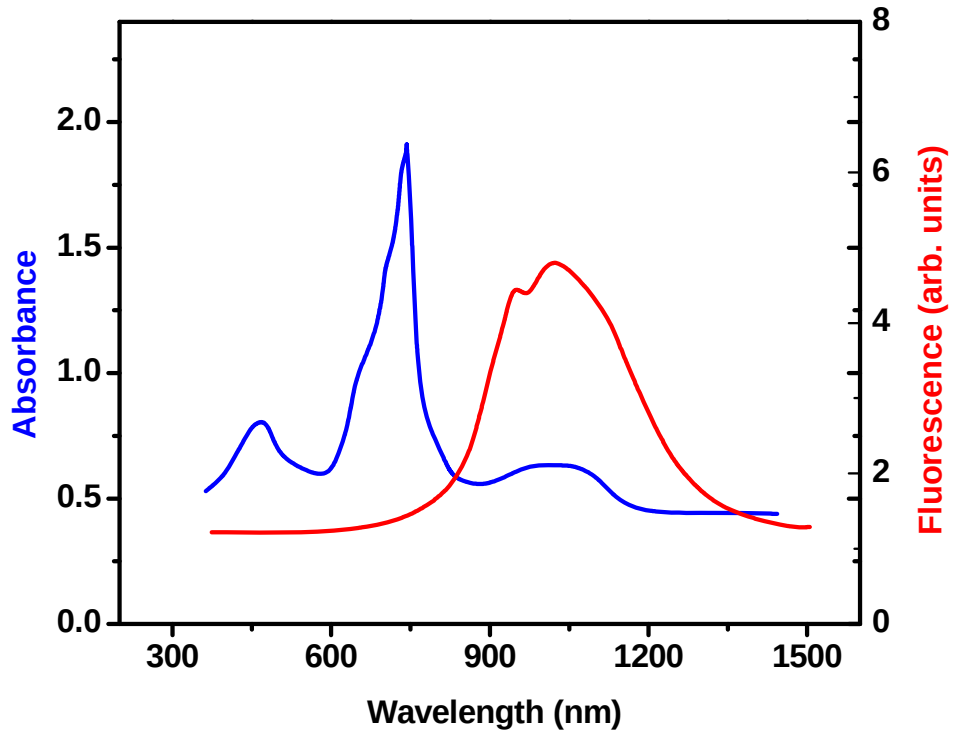

Figure 2.4. Absorption and fluorescence spectra of Cr:forsterite at room temperature [28].

There are two broad peaks in absorption spectra as shown in Fig. 2.4, one at 780 nm and the other ranging between 900-1150 nm. This allows the crystal to be pumped optically by various commercially available lasers. Among them Nd:YAG laser at 1064 nm and ytterbium-doped fiber lasers at 1075 nm are two mostly used.

2.3.2. Lifetime thermal loading and lensing

As mentioned earlier, enhancement of non-radiative decay at higher temperature decreases the fluorescence lifetime. Cr:forsterite suffers most from the degradation of the lifetime of the pumping states and poor thermal conductivity [48]. These effects cause subsequent reductions in population inversion and quantum efficiency of the laser crystal which thereby raise the lasing

threshold and lower output efficiency. Furthermore, this detoriation of the lifetime due to thermal loading is particularly important for the gain media with low heat conductivity. Despite the use of various cooling methods to stabilize the crystal boundary temperature, the heat load due to unused pump power can still lead to a considerable amount of local heating inside the crystal. Because of the temperature dependence of the refractive index, the heat loss due to unused pump power can also cause thermal lensing which can change the beam profile and power transmission inside the cavity [33]. But these problems can be minimized to some extent by choosing a crystal rod with reduced transverse dimensions [33]. Figure 2.5 below shows the temperature dependent lifetime for Cr:forsterite, Cr:YAG and Ti:sapphire crystal reproduced from Ref. [48].

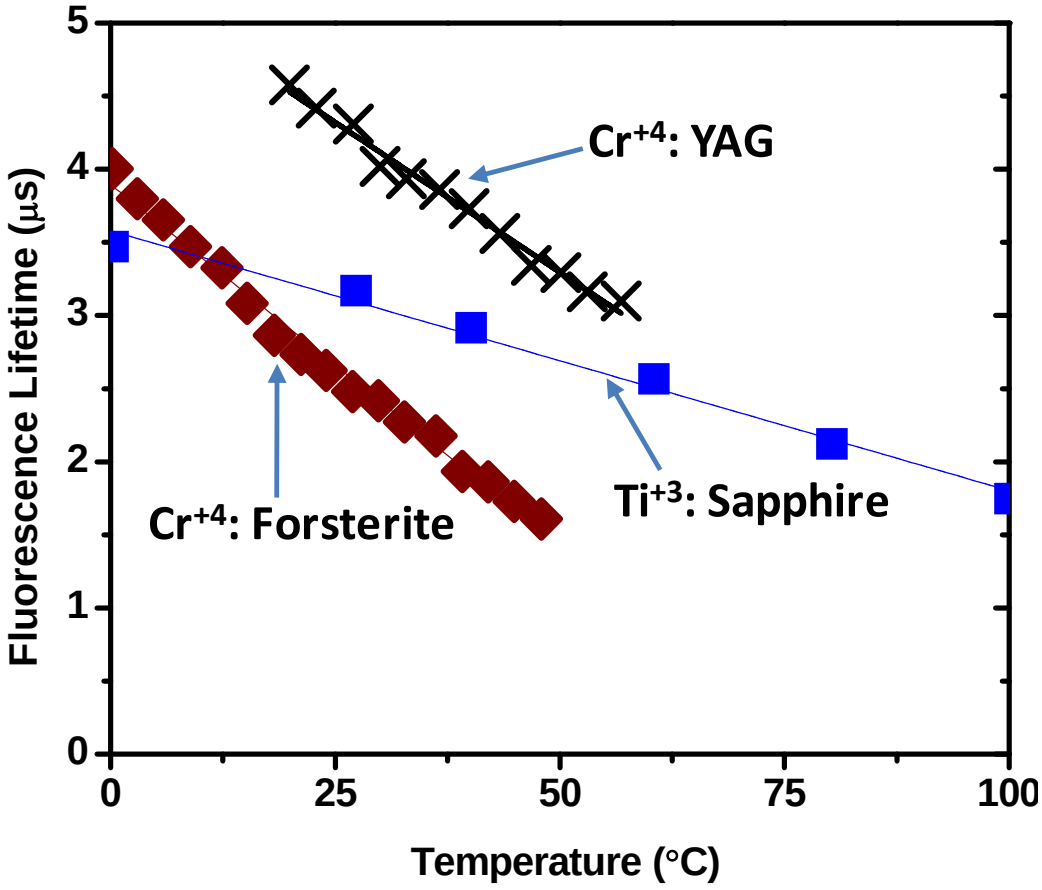

Figure 2.5. Temperature dependent lifetime data for Cr:forsterite, Cr:YAG and Ti:sapphire gain media. We can see that Cr:forsterite has steeper slope and it suffers most from the change in temperature. In fact, cooling to 77K from room temperature changes life time of the excited state from 2.4 μs to 20μs. Figure reproduced from reference [48].

Thermal and spectroscopic parameters of various vibronic lasers used in the calculation of figure of merit for lifetime thermal loading is performed by Alphan Sennaroglu in Ref. [56].

2.4. Dispersion

This Section focuses on the mathematical development of an ultrashort laser pulse and its interaction with the medium through which it propagates. The nature of this interaction depends upon the intensity of the pulse and the properties of the material. Higher intensity of the pulse gives various nonlinear effects that can be utilized even in the process of mode locking. In the laser cavity, there are many optical components such as laser crystal, prism, chirped mirror, air and output coupler where laser pulse is generated and interacts with medium itself. This gives rise to various effects such as dispersion, self phase modulation etc.

An optical pulse in the time domain can be written as,

$$E(t) = A(t)\exp i((\omega_0 t - \phi(t)) \tag{2.4}$$

where *A(t)* is time varying electric field envelope, $\phi(t)$ is the temporal phase variation across the pulse and ω_0 is the optical carrier frequency.

When these pulses propagate through the dielectric medium of neutral charge, the individual atom experiences a dipole force. As a result each atom develops a dipole moment and the sum of all these dipole moments within the medium is called polarization. Depending upon the intensity of the beam and the nature of the material, we can get all sorts of linear and nonlinear effects inside the medium. So, a dielectric medium under the influence of electromagnetic field produces an intensity-dependent polarization of the form,

$$P = \varepsilon_0 \left[\chi^{(1)} E + \chi^{(2)} E^2 + \chi^{(3)} E^3 + ... \right] \tag{2.5}$$

where ε_0 is the permittivity of free space, E is the applied electric field and $\chi^{(n)}$ is the nth order susceptibility. The exact description of how an intense pulse interacts with a medium depends on the strength of its electric field and one common approach is consider a linear response due to the first term of Eq. (2.7) separately from the nonlinear response arising from the higher order terms. Generally, a linear response arises at lower laser intensity than the nonlinear response does.

In the expression (2.7), $\chi^{(1)}$ is the linear susceptibility and is used to describe the linear optical effects such as refraction, reflection and dispersion. Similarly, nonlinear effects due to second order susceptibilities, $\chi^{(2)}$ describe second harmonic generation (SHG) and sum-frequency mixing (SFG). The third term, $\chi^{(3)}$ describes third order nonlinear effects such as third harmonic generation (THG) and the optical Kerr effect.

2.4.1. Material dispersion: linear effect

When an ultrashort laser pulse with a specific spectral bandwidth propagates through a linear dielectric medium, the spectral components will travel at different speeds in the medium due to a wavelengths dependence of the index of refraction. The material dispersion will cause the ultrashort pulse to broaden in time but its spectral width remains the same. Only nonlinear effects or wavelength-dependent gain or loss can cause change in a pulse's spectral width.

The dispersion is characterized by the mode propagation constant, $\beta(\omega)$ which is typically written as a Taylor series

$$\beta(\omega) = \beta_0 + \beta_1 \frac{\omega-\omega_0}{1!} + \beta_2 \frac{(\omega-\omega_0)^2}{2!} + \beta_3 \frac{(\omega-\omega_0)^3}{3!} + \sum_m \frac{1}{m}\beta_m (\omega-\omega_0)^m \qquad (2.6)$$

$$\text{where, } \beta_m = \left(\frac{d^m\varphi}{d\omega^m}\right)_{\omega=\omega_0} \qquad (2.7)$$

ω_0 represents carrier frequency. The mode propagation constant, $\beta(\omega)$ represents the component of the wave vector k along the direction of propagation. The first term, $\beta_0(\omega)$ describes a change in the phase of the central carrier frequency as it propagates through the material and has no effect on the pulse shape itself. The second term, $\beta_1 = \frac{d\varphi}{d\omega}$ describes a linear phase ramp in frequency that corresponds to a temporal delay in the pulse as it travels through the medium. It is related to the group velocity, v_g which defines the velocity of the pulse in the medium.

$$v_g = \frac{1}{\beta_1} = 1/\frac{d\varphi}{d\omega} \qquad (2.8)$$

This definition of group velocity is consistent with a slightly different approach in which the phase velocity of a wave is defined by:

$$v_p = \left(\frac{k}{\omega}\right)^{-1} \tag{2.9}$$

where k is the wave vector and ω its frequency. The third term or quadratic spectral phase term is responsible for introducing a linear chirp into the pulse; this effect is temporally broadens a pulse. The fourth term or cubic chirp is responsible for introducing the quadratic frequency chirp into the pulse, which can temporally extend one end of the pulse and sharpen the other end and can lead to pulse break up. All of these processes in effect are to limit the minimum attainable pulse duration by a system such as a laser cavity.

For a bulk medium, β_1, β_2 and β_3 are related to the index $n(\lambda)$ by,

$$\beta_1 = \frac{1}{c}\left[1 + \omega\frac{dn}{d\omega}\right] = \left(\frac{n}{c}\right)\left(1 - \frac{\lambda}{n}\frac{dn}{d\lambda}\right) \tag{2.10}$$

$$\beta_2 = \frac{1}{c}\left(2\frac{dn}{d\omega} + \omega\frac{d^2n}{d\omega^2}\right) \approx \frac{\lambda^3}{2\pi c^2}\frac{d^2n}{d\lambda^2} \tag{2.11}$$

$$\beta_3 \approx -\frac{\lambda^4}{2\pi c^2}\left(3\frac{d^2n}{d\lambda^2} + \lambda\frac{d^3n}{d\lambda^3}\right) \tag{2.12}$$

where, $n(\lambda)$, is wavelength dependent refractive index, can be described by the empirical relation called Sellmeier equation of the general form,

$$\mathrm{n}^2(\lambda) = 1 + \frac{A_1\lambda^2}{\lambda^2 - B_1} + \frac{A_2\lambda^2}{\lambda^2 - B_2} + \frac{A_3\lambda^2}{\lambda^2 - B_3} \tag{2.13}$$

where $A_{1,2,3}$ and $B_{1,2,3}$ are material dependent coefficients that are determined by experiment. Figure 2.6 shows the effect of dispersion on a Gaussian pulse.

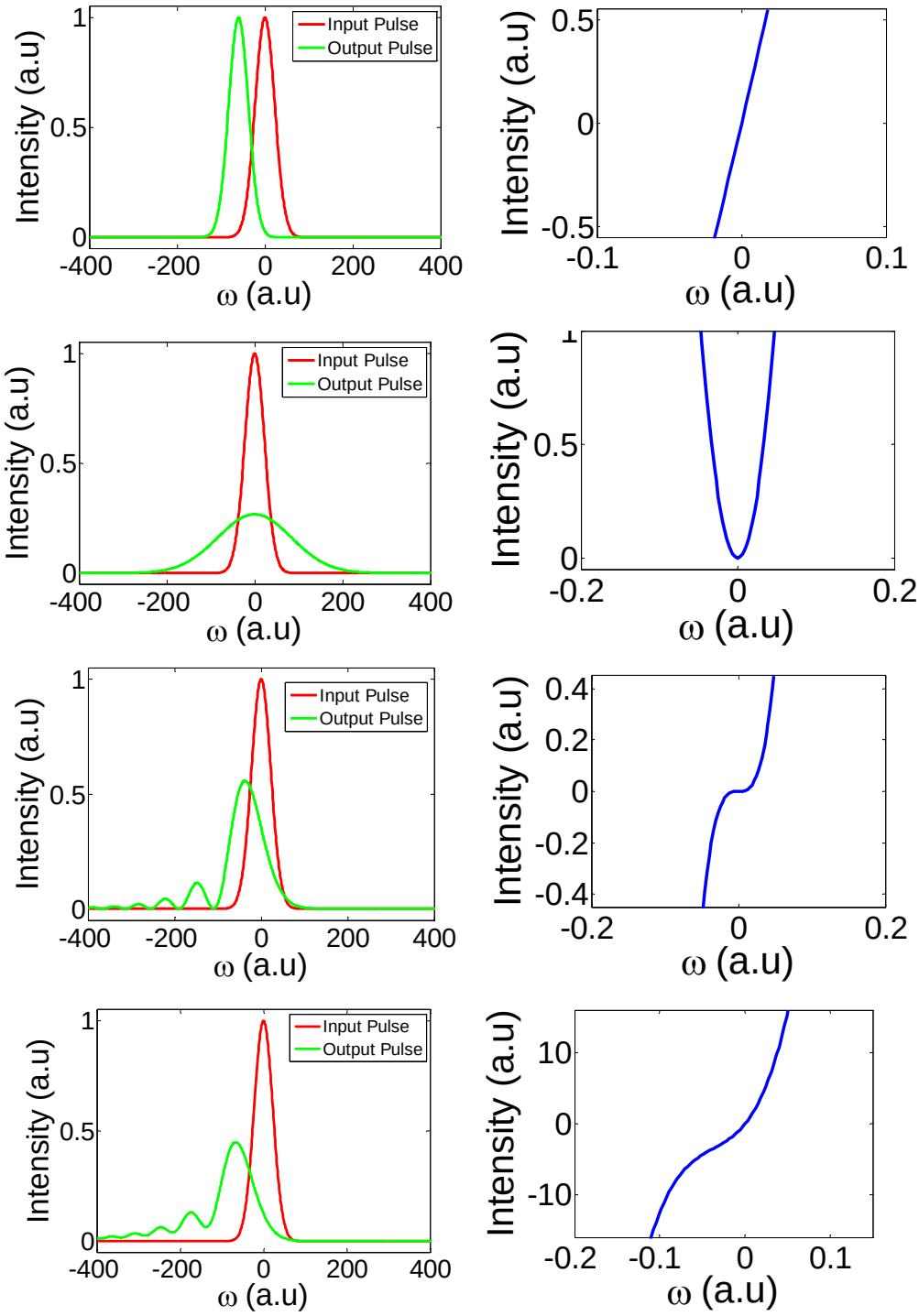

Figure 2.6. Simulation shows the effect of first, second, third and all three terms of expansion of mode propagation constant; $\beta(\omega)$ from Eq. (2.7) on temporal profile of the Gaussian pulse. These plots clearly show that the effect of higher order dispersion is not only to broaden the pulse but it also can lead to significant pulse distortion even to the point of pulse break up. Plot on right side (blue line) of each plot shows the instantaneous phase of the pulse.

2.4.2. Dispersion due to Cr:forsterite crystal inside the cavity

Generation of the shortest femtosecond pulse requires accurate dispersion data for the material inside the laser cavity. This requires a slightly negative net cavity dispersion and minimum third order dispersion. The largest dispersion source in the Cr:forsterite laser is still the crystal and pair of prisms provides the necessary negative dispersion. The selection of the material for the prism is determined by the crystal dispersion itself. Most of the dispersion data for Cr:forsterite has been reported in the context of femtosecond pulse generation[42, 57-60]. To the best of my knowledge, there is only one measurement of the index of refraction of the Cr:forsterite at different wavelength from which required dispersion can be computed [61]. But the data of refractive index dispersion for Cr:forsterite shows little agreement with any of the other studies and there are significant discrepancies among many of these measurements. To make accurate dispersion data available for broadband dispersion compensation, Thomann *et al* [62] made some independent determination of Group-delay dispersion (GDD) and Third-order dispersion (TOD) of Cr:forsterite using a white-light Michelson interferometer. The crystal used by Thomann was purchased in the same batch as ours. In this section, here we briefly review some of these dispersion measurements.

The refractive index dispersion allows access to the group velocity dispersion. Burshtein *et al.* measured the room temperature refractive dispersion of the Cr^{4+}:forsterite in the 0.35-2.0 μm spectral range for all crystallographic orientations, a, b and c. First of all they showed the dispersion curve for n_a, the data points are best fitted to a Sellemeier function of the form,

$$n^2 = 1 + \frac{A\lambda^2}{B + \lambda^2 + C\lambda^{-2}} \tag{2.14}$$

Where, $A_a = 1.6595 \pm 0.002$, $B_a = -0.0162 \pm 0.001$ μm^2 and $C_a = (5 \pm 0.4)10^{-4}$ μm^4

The data for n_b and n_c are best fitted to the Sellemeier function of the form,

$$n^2 = 1 + \frac{A\lambda^2}{B + \lambda^2 + C\lambda^{-1.6}} \tag{2.15}$$

Where,$A_b = 1.608 \pm 0.0025$, $B_b = -0.0185 \pm 0.0002$ μm^2 and $C_b = (11.0 \pm 0.6) \times$ $10-4$μm4

$A_c = 1.7145 \pm 0.0025$, $B_c = -0.0175 \pm 0.0002$ μm^2, $C_c = (9.9 \pm 0.8) \times 10^{-4}$μm^4

The plots of all of these three values of refractive index dispersion curve is shown in Fig. 2.7,

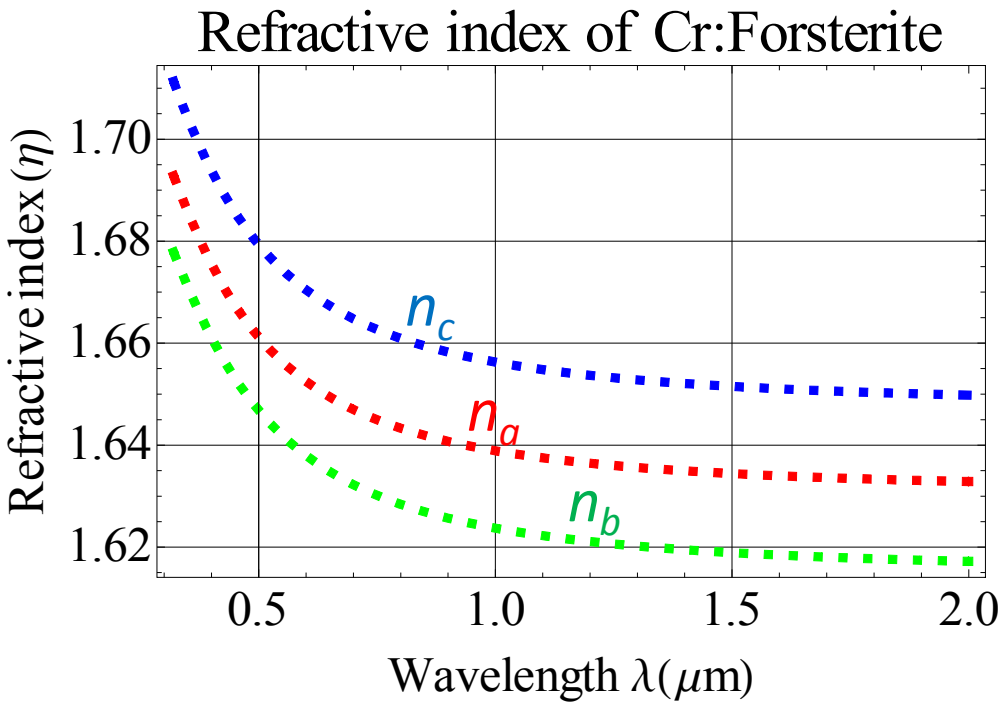

Figure 2.7 Spectral dispersion of refractive indices in Cr^{4+}:Mg_2SiO_4 (reproduced from Ref.[61]).

From the measurements of spectral dispersion of refractive indices as given in Eq. 2.14 and 2.15, we can easily find the GDD and TOD by using Eq. 2.11 and 2.12; the plot of GDD and TOD is shown in Fig. 2.8 and Fig. 2.9 below to compare with the other measurements.

Zhang *et al*. [58] made an independent measurement of group delay of Cr:forsterite crystal from which we can easily calculate GDD and TOD of the material. He has given an analytic function for the group delay (in fs) as a function of frequency (in THz). The expression of Zhang is for 7 mm of Cr:forsterite which is double passed (i.e. 14 mm total) so I have normalized this expression to compare with other by dividing by 14 mm. Zhang claims this is for propagation along the c axis with the E-field parallel to the a-axis. However, he does not define his axis system, so it may be difficult to compare to other results.

$$\mathrm{GD}_{\mathrm{zhang}}(\mathrm{fs}) = 1388.97 - 15.293f + 0.049809f^2 - 3.9805 \times 10^{-5} f^3 \qquad (2.16)$$

where f is in THz. From this expression we can simply calculate GDD and TOD by taking successive differentiation of group delay which I have plotted in Fig. 2.8 and Fig. 2.9 below. The GDD calculated from Eq. (2.16) is found to be in close agreement with one that is measured by

Thomann *et al* using white light interferometry techniques, which we believe is the most reliable one. Thomann has given expression for GVD and TOD for b-axis of crystal in Ref. [62],

$$\text{GVD}_{\text{Thomann}} = \frac{1}{2*L*10^{-3}}(2k_2 + 6k_3(\omega - \omega 0) + 12k_4(\omega - \omega 0)^2 + 20k_5(\omega - \omega 0)^3)$$

(in fs^2/mm) (2.17)

$$\text{TOD}_{\text{Thomann}} = \frac{1}{2*L}(6k_3 + 24k_4(\omega - \omega 0) + 60k_5(\omega - \omega 0)^2)(\text{in fs}^3/\text{mm}) \quad (2.18)$$

Where, $k_2 = 84.42\text{fs}^2, k_3 = 116.7\text{fs}^3, k_4 = -101.21\text{fs}^4, k_5 = 125.08\text{fs}^5$

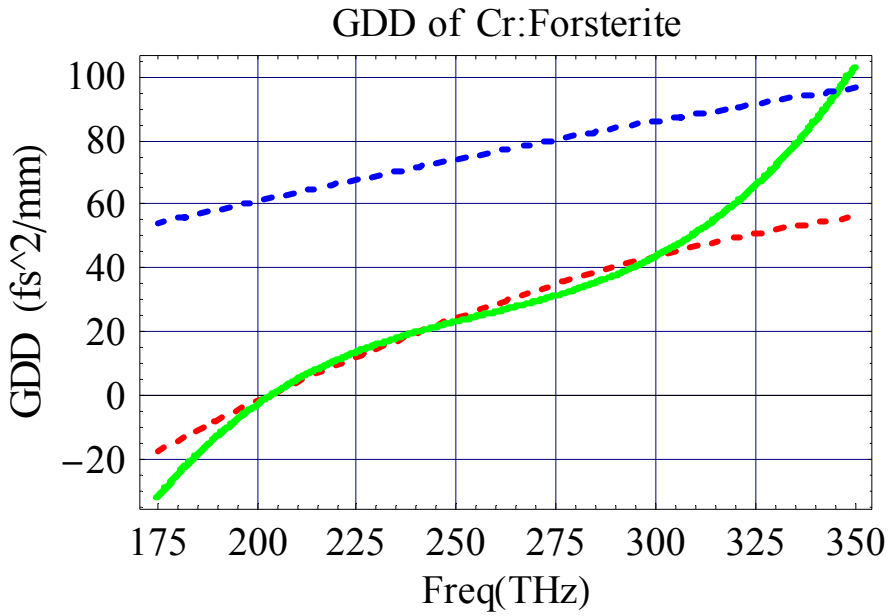

Figure 2.8. Group delay dispersion of Cr:forsterite crystal vs. frequency. We can see very large discrepancy in different measurement performed by different group. Blue line is the GDD derived from the Sellemeier function of Cr:forsterite crystal [61] which is given in Eq. (2.15) . Thomann [62] measurement (green solid line) is in reasonably good agreement with Zhang [58] measurement (red dotted line).

When we compare all of these measurements for GDD, we can infer that the measurement done by Thomann is in reasonably good agreement with Zhang. Even though Thomann and Zhang measurements agree pretty well in terms of GDD, there is a discrepancy of at least 50% in the measurement of TOD between them. Although the crystal orientation is not

specified in the Zhang measurements, we assume that the most common orientation for all previous measurements was for light polarized along the *b* axis.

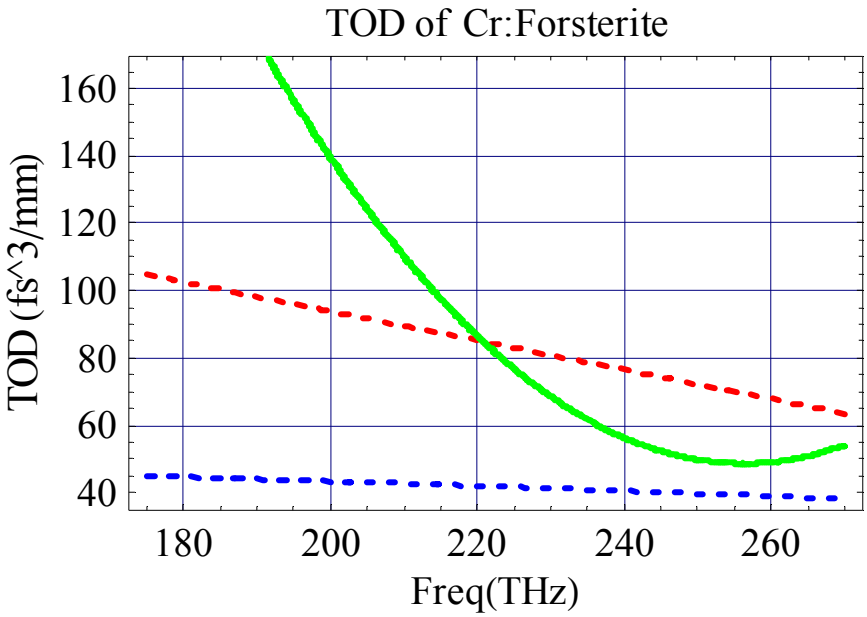

Figure 2.9. Third order dispersion of Cr:forsterite crystal vs. frequency in THz. Blue dotted line is the TOD derived from the Sellemeier function of Cr:forsterite crystal [61] which is given in Eq. (2.15) . There is a discrepancy of at least 50% in the measurement of TOD between Thomann measurement (green solid line) and Zhang measurement (red dotted line).

Even though the crystal used by Thomann *et al.* in their measurement is exactly similar to ours, it should be noted that the theory described in white light interferometry does not take into account the possible nonlinear refractive index of Cr:forsterite. For mode-locked laser operation when beam is focused to the crystal, peak intensities can become so large that nonlinear refractive index might contribute to dispersion.

2.4.3. Dispersion compensation using SF6 Prism

Cr:forsterite crystal has low gain. Therefore, we need to choose longer crystal to get sufficient pump absorption for lasing. We use a 15 mm long crystal. The longer crystal has larger group delay dispersion (GDD) and third order dispersion (TOD); therefore, Cr:forsterite crystal itself is the dominant source of dispersion inside the laser cavity. Precise control of GDD and TOD is extremely important to get reliable and stable modelocking. The calculation and

measurement for dispersion compensation shows that a pair of SF6 prism inside the cavity can compensate both the GDD and TOD of Cr:forsterite laser cavity.

Here, we would like to calculate quadratic (related to GDD) and cubic phase distortion (related to TOD) due to SF6 prism pairs. TOD is not as dominant as GVD inside the cavity unless we are dealing with pulse shorter than ~20 fs. Net dispersion due to prism pairs is the sum of dispersion due to material itself and angular dispersion due to the geometry of the prism separation. Material dispersion is generally positive whereas prism separation gives negative dispersion inside the cavity. For ultrashort pulses to be realized, a net cavity dispersion should be negative. By choosing the correct separation between the prisms, an overall negative dispersion can be introduced inside the cavity where shorter wavelength components experience a shorter physical path length through the prism system as compared to longer wavelength component. The arrangements of prisms are shown in Fig.2.10; both the prisms have been cut so that the angle of minimum deviation is also Brewster's angle. The arrangement of prism with mirror acts like a four prism in sequence where light exactly follows the same path in both directions.

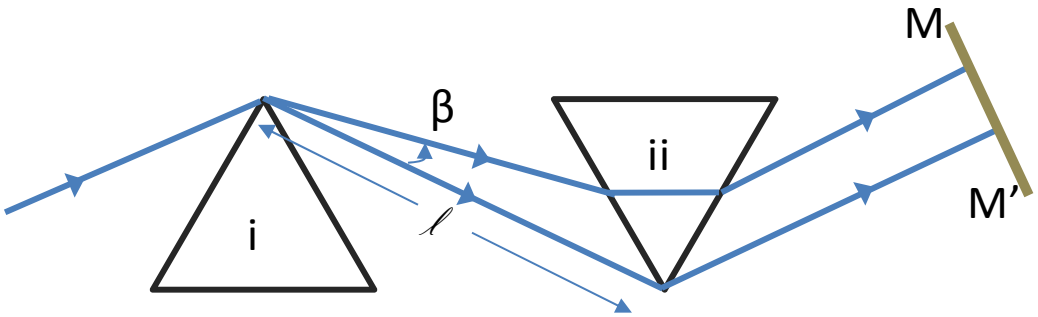

Figure 2.10. A sequence of prisms and mirror which can be adjusted to give a net negative dispersion. The prisms are used at angle of minimum deviation and the rays enter and leave at Brewster's angle.

Sellemeier equation and coefficients for SF-6 glass are given below,

$$n(\lambda) := \sqrt{1 + \frac{B_1\lambda^2}{\lambda^2 - C_1} + \frac{B_2\lambda^2}{\lambda^2 - C_2} + \frac{B_3\lambda^2}{\lambda^2 - C_3}} \tag{2.19}$$

Where the coefficients are,

$B_1 = 1.72448482$ $B_2 = 0.390104889$

$B_3 = 1.04572858$ $C_1 = 0.0134871947$ (2.20)

$C_2 = 0.0569318095$ $C_3 = 118.557185$

The detail of the theoretical calculation of net cavity dispersion due to prism pair is given in Ref. [63]. Let us consider the Cr:forsterite laser cavity where we use an SF6 prism pair separated by a distance of ℓ = ~300 mm. The beam size of the laser inside the cavity is d = ~1.5 mm. The amount of prism inserted inside the laser beam is d = 15 mm. The material dispersion due to insertion of prism inside the laser beam can be calculated by using the expression 2.11 and 2.12,

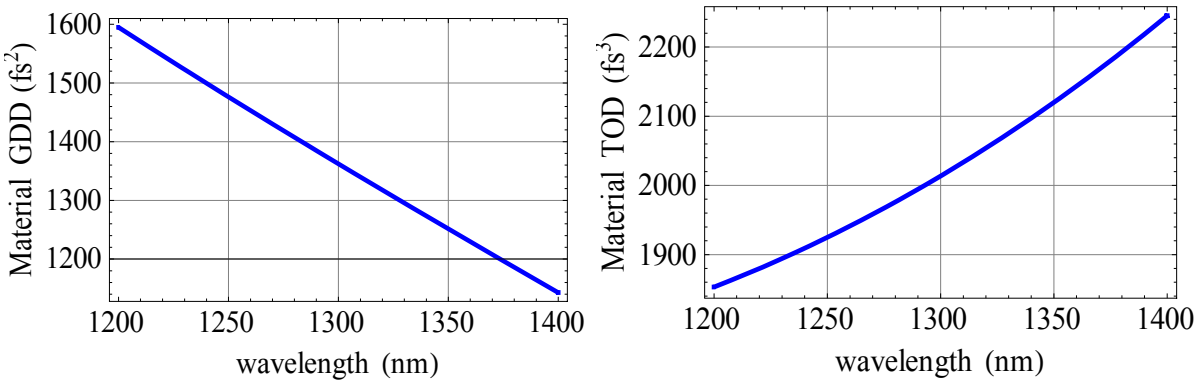

Figure 2.11. Material dispersion due to prism pairs inside the cavity.

Now the angular dispersion due to separation of the prism can be calculated by using the expression given in Ref. [63]. Let P be the optical path length. The dispersion parameter *D* is related to the second derivative of the optical path length with respect to wavelength,

$$D = -\frac{\lambda}{cL}\frac{d^2P}{d\lambda^2} \tag{2.21}$$

$$\text{where, } \frac{d^2P}{d\lambda^2} = 4l\left[\left\{\frac{d^2n}{d\lambda^2} + \left(2n - \frac{1}{n^3}\right)\left(\frac{dn}{d\lambda}\right)^2\right\}\sin\beta - 2\left(\frac{dn}{d\lambda}\right)^2\cos\beta\right] \tag{2.22}$$

Here, L is physical length of the light path and l is the physical distance between prisms in meters. However, the spot size is related to l and β. The term l sinβ should be on the order of twice the spot size d. Thus,

$$\sin\beta = \frac{2d}{l} \quad \text{and} \quad \cos\beta = \sqrt{1-\sin^2\beta} \tag{2.23}$$

The phase change due to the prisms can be related by the change in optical path length with wavelength. The second and third order phase derivative is represented in units of fs^2 and fs^3 respectively.

$$\beta_2 = \frac{\lambda^3}{2\pi c^2}\frac{d^2P}{d\lambda^2} \tag{2.24}$$

And, $$\beta_3 = -\frac{\lambda^4}{2\pi c^2}\left(3\frac{d^2P}{d\lambda^2} + \lambda\frac{d^3P}{d\lambda^3}\right) \tag{2.25}$$

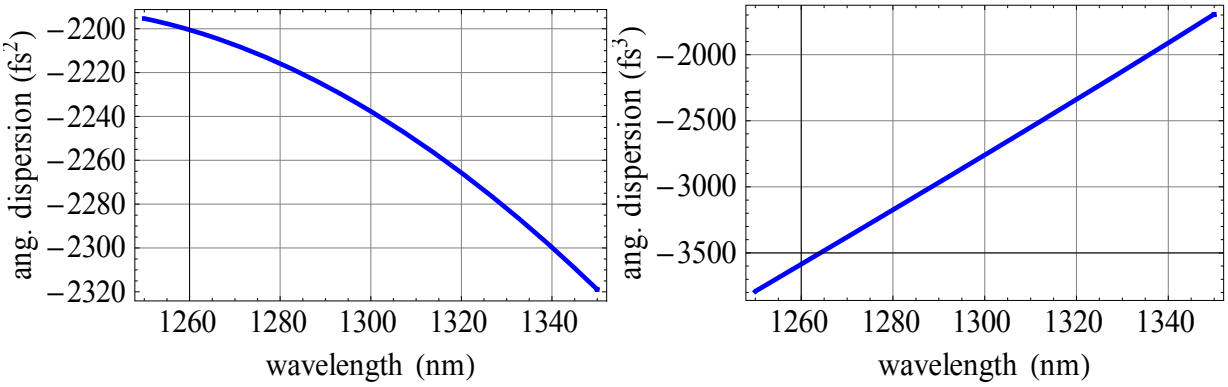

Figure 2.12. Angular dispersion due to prism separation.

Figure 2.11 and 2.12 shows that the SF6 prism pair with separation of ~30 cm not only compensates the material dispersion due to the prism itself but it also provides sufficient negative GDD and TOD to compensate both second order and third order dispersions due to the Cr:forsterite crystal.

2.5. Cr: forsterite cavity design

The cavity configuration of the prism-based Cr:forsterite laser is shown in Fig. 2.13 below. The Cr:forsterite crystal we used has the same bulk properties as that used in Ref. [62] (doping of 0.2% by weight, absorption coefficient α = 1.1 cm^{-1} at 1075 nm, dimension 2 mm×4 mm×15 mm). The general resonator configuration of the solid state laser is a 4 mirror resonator consisting of two flat mirror and two curved mirrors that focus the fluorescence into the laser crystal. One of the flat mirrors is a high reflector mirror and another is an output coupler. We can insert one or more flat mirrors between the curved mirror and the high reflector without changing the laser characteristics. Since the Cr:forsterite crystal has low gain, in order to have optimum output power, there must be extremely good mode matching of the pump beam and laser beam. Due to the short upper-state lifetime of the Cr:forsterite crystal, a high intensity pump beam is

required to obtain sufficient population inversion for lasing. Such a high intensity can be achieved by tight focusing of the pump beam inside the crystal. We have used the ABCD matrix simulation to figure out the optimum beam profile inside the crystal for optimum cavity mirror position. The program written in Mathematica can calculate the positions of the cavity mirrors that allow stable operation. We can also plot the stability region inside the cavity as well as beam shape inside the cavity for particular mirror separation values.

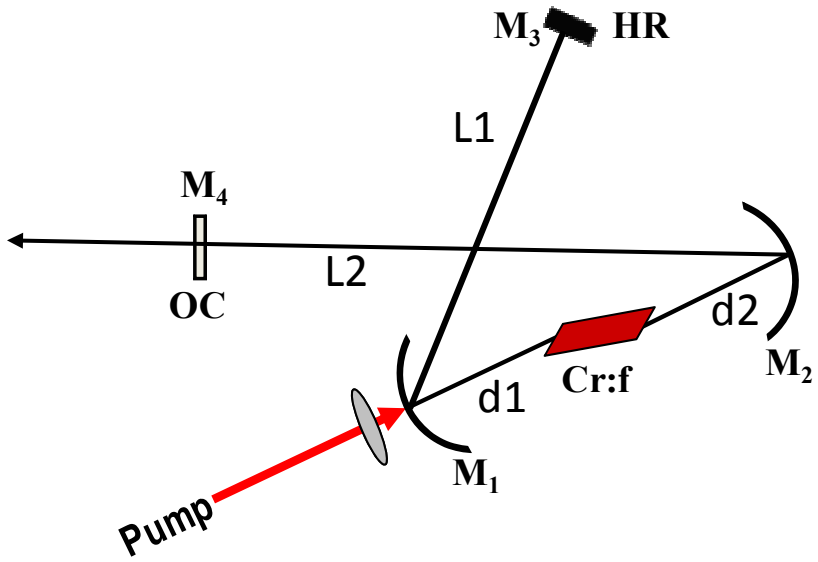

Figure 2.13. Sketch of 4 mirror cavity design of Cr:forsterite laser cavity.

The effect of the asymmetric devices such as a Brewster cut crystal is to produce astigmatic Gaussian beams. The beams have different spot sizes, wavefront curvatures and beam waist positions in the two orthogonal planes called the sagittal plane and the tangential plane. In other word, because of a lack of axial symmetry in our cavity, the beam waist along the sagittal and tangential planes may not necessarily overlaps spatially due to astigmatism. Therefore, the effects of astigmatism must be taken into account in cavity stability analysis.. There are two focusing lengths of the crystal depending upon the plane in which beam is focused,

$$f_x = f\cos\theta \text{ and } f_y = \frac{f}{\cos\theta} \tag{2.26}$$

where θ is the angle between the incident beam and the normal to the mirror. The effect of this astigmatism is also to lift the frequency degeneracy between the TEM_{mn} modes with the same

value of m+n. One way to compensate these effects is to use another source of astigmatism such as off-axis reflection from the curved mirror into the crystal.

In this way, for the tangential plane, the exit beam parameters from the crystal to air differ from the entrance-beam parameters from air to crystal in the same ways as if beam had traveled the free space distance of $\frac{t}{\left(n^2-\sin^2\theta\right)^{1/2}}$ and for tangential plane it is $\frac{t\,n^2(1-\sin^2\theta)}{\left(n^2-\sin^2\theta\right)^{3/2}}$

[64]

Hence for the tangential plane, the ray transfer matrix for air to crystal interface is,

$$\begin{pmatrix} 1 & \frac{t\,n^2(1-\sin^2\theta)}{\left(n^2-\sin^2\theta\right)^{3/2}} \\ 0 & 1 \end{pmatrix} \tag{2.27}$$

Similarly, for the sagittal plane, the ray transfer matrix is,

$$\begin{pmatrix} 1 & \frac{t}{\left(n^2-\sin^2\theta\right)^{1/2}} \\ 0 & 1 \end{pmatrix} \tag{2.28}$$

If we assume that light get incident under Brewster angle, $\theta = \arctan\left(\frac{n_2}{n_1}\right)$, for the air-to-crystal interface, n_1=1 and n_2= n, $\Rightarrow \tan\theta = n \quad \Rightarrow \sin\theta = \frac{n}{\sqrt{n^2+1}}$, so both the above expression 2.27 and 2.28 reduces to,

$$\begin{pmatrix} 1 & \frac{t\sqrt{n^2+1}}{n^4} \\ 0 & 1 \end{pmatrix} \text{ and} \tag{2.29}$$

$$\begin{pmatrix} 1 & \frac{t\sqrt{n^2+1}}{n^2} \\ 0 & 1 \end{pmatrix}, \tag{2.30}$$

both of these effects can be compensated by varying θ. The astigmatically corrected cavity not only has lower threshold but also gives close to circular output beam as compared to the uncorrected cavity.

2.4.1 Rays in periodic focusing systems

We need to figure out the stability criteria for the laser cavity. Laser cavities are in fact a periodic focusing system which can be divided into either stable or unstable periodic systems depending only on the properties of the eigenvalue of the ABCD matrices,

Let us suppose a ray matrix, M, propagation through one period in such a system,

$M = \begin{bmatrix} A & B \\ C & D \end{bmatrix}$, let us find eigenvalue of M, for non-trivial solution,

$$\begin{vmatrix} A-\lambda & B \\ C & D-\lambda \end{vmatrix} = 0 \quad \Rightarrow \lambda^2 - m\lambda + 1 = 0 \text{ where, } m = \frac{A+D}{2}$$

So matrix eigenvalues are, $\lambda_a, \lambda_b = m \pm \sqrt{m^2 - 1}$ which obey the relation ship $\lambda_a \times \lambda_b = 1$

If r_a and r_b are two eigenray vectors then $\mathrm{M}\, r_a = \lambda_a r_a$ and $\mathrm{M}\, r_b = \lambda_b r_b$, Now we can write any arbitrary ray, r_0 into the form, $r_0 = c_a r_a + c_b r_b$ where c_a and c_b are expansion coefficient. If ray travels through number of optical element then the ray vector can be written as,

$$r_n = M^n r_0 = M^n (c_a r_a + c_b r_b) = c_a \lambda_a^n r_a + c_b \lambda_b^n r_b$$

Let us suppose the ray matrix for one period has A and D coefficients such that,

$-1 \le m \le 1$ or $m^2 = \frac{A+D}{2} \le 1$, In this situation we can write m=cosθ. Therefore,

$$\lambda_a, \lambda_b = m \pm i\sqrt{1-m^2} = \cos\theta \pm i \sin\theta = e^{\pm i\theta}$$

r_n takes the form, $r_n = c_a r_a e^{in\theta} + c_b r_b e^{-in\theta} = r_0 \cos\theta_n + s_0 \sin\theta_n$

where, $r_0 = c_a r_a + c_b r_b$ is the input ray vector and

$s_0 = i(c_a r_a - c_b r)$ is the input slope vector

So, if m≤1, $\Rightarrow m^2 = \frac{A+D}{2} \le 1$, (2.31)

represent conditions for a stable periodic system in which rays in the system oscillate back and forth about the axis where r_o and s_o are the initial conditions. Similarly, we can show that for m>1, we will get an unstable periodic system in which the final ray vectors turns out to be $r_n = r_0 \cosh\theta_n + s_0 \sinh\theta_n$ where $\theta = \ln(m + \sqrt{m^2 - 1})$; here r_n diverge exponentially and therefore represents an unstable periodic system.

2.4.2. Stability analysis of a Cr:forsterite cavity

The Cr:forsterite laser cavity, as shown in Fig. 2.14 below, consists of 1.5 cm long crystal that lies in between the two curved mirror of radius of curvature 10 cm, with distances d_1 and d_2, which are the variable parameters of the stability analysis. There is a flat mirror, output coupler, which has a distance of L_1=50 cm to the curved mirror M_1 as shown in figure. The distance of another curved mirror M_2 to the end mirror M_4 is L_2 = ~60 cm. In the arm L1 of the cavity, we have a prism pair for dispersion compensation which is not considered here even though prism is also a source of astigmatism.

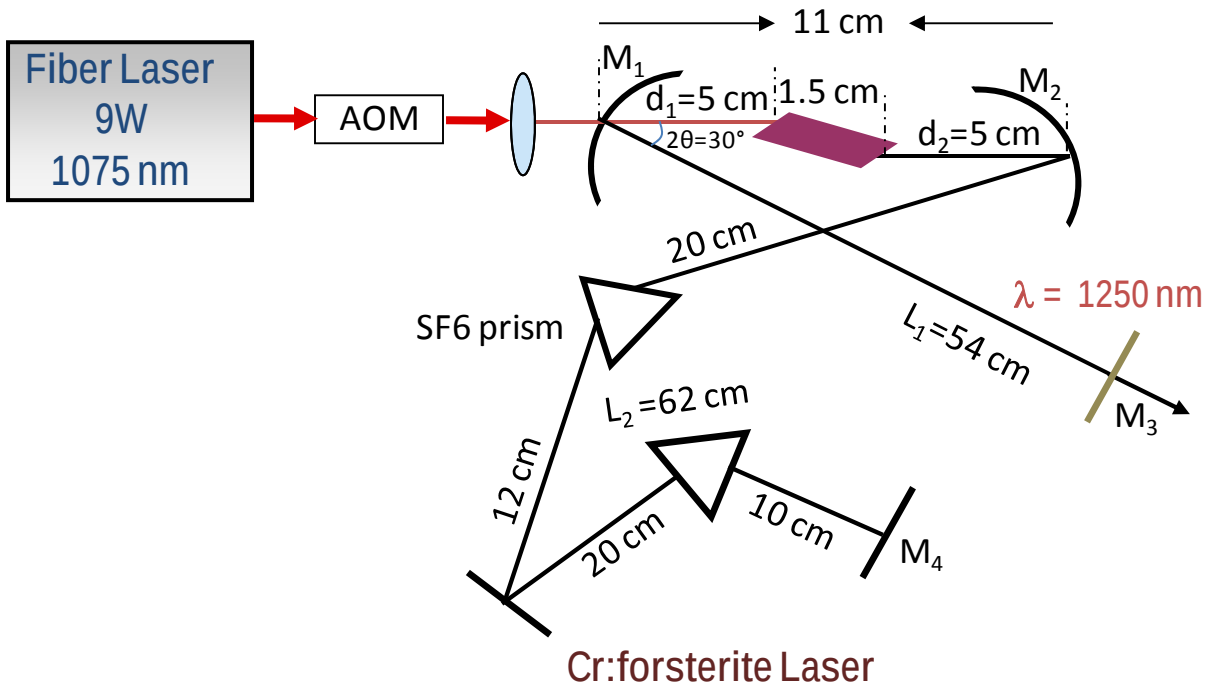

Figure 2.14. Approximate dimension of the Cr:forsterite laser cavity.

The ABCD matrix of this linear cavity is calculated by including astigmatism introduced from the end mirror as well as from the Brewster-cut gain medium with refractive index ~1.63. These two astigmatisms are used in a way to nullify effect of both to get astigmatic free beam profile inside the crystal. The round trip ABCD matrix of the four mirror cavity is calculated by choosing a reference plane at the middle of the crystal. Note that this process is performed twice,

once for the tangential plane and once for the sagittal plane since the curved mirrors M_1 and M_2 and Brewster-cut crystal behave differently in the two planes. The ABCD matrix for a complete round trip through the cavity is then given by multiplying all the matrix elements for each and every optic starting from the centre of the crystal and all the way back to the same place. In short an ABCD matrix allows the output of an optical element to be written in terms of its input. The hard part about ABCD matrix analysis is coming up with the appropriate ABCD matrices for the elements in the system to be analyzed. The detailed derivations of the transfer matrices of other simple optical elements will not be discussed here, but a table is included which gives the general form of the transfer matrices for several optical elements [65].

Table 2.2. Transfer matrices of some of the simple optical elements [65].

Elements	Matrix	Remarks
Propagation in free space or in a medium of constant refractive index	$\begin{bmatrix} 1 & \frac{L}{\mathrm{n0}} \\ 0 & 1 \end{bmatrix}$	L = distance
Reflection from a flat mirror	$\begin{bmatrix} 1 & 0 \\ 0 & 1 \end{bmatrix}$	Identity matrix
Reflection from a curved mirror, for tangential plane.	$\begin{bmatrix} 1 & 0 \\ -\frac{2}{R\mathrm{Cos}[\theta]} & 1 \end{bmatrix}$	R = $R\mathrm{Cos}[\theta]$ radius of curvature for tangential plane
for sagittal plane	$\begin{bmatrix} 1 & 0 \\ -\frac{2\mathrm{Cos}[\theta]}{R} & 1 \end{bmatrix}$	R=$\frac{R}{\mathrm{Cos}[\theta]}$ radius of curvature for sagittal plane
Incidence of light under Brewster angle from air to crystal.	$\begin{bmatrix} 1 & \frac{\sqrt{1+n^2}t}{n^4} \\ 0 & 1 \end{bmatrix}$	t=thickness of crystal. For tangential plane
	$\begin{bmatrix} 1 & \frac{\sqrt{1+n^2}t}{n^2} \\ 0 & 1 \end{bmatrix}$	For sagittal plane

The matrices depend on the mirror's radii of curvature, the thickness of crystal, the refractive index, the distances from the curved mirrors to crystal, denoted by d_1 and d_2, the

distance from curved mirrors to the end mirrors, L_1 and L_2, and angle between incoming and outgoing beams on the curved mirrors.

The ABCD matrix for a complete round trip through the cavity in tangential plane is given by,

$$\begin{pmatrix} 1 & \frac{\sqrt{1+n^2}t/2}{n^4} \\ 0 & 1 \end{pmatrix} * \begin{pmatrix} 1 & 0 \\ -\frac{2\mathrm{Sec}\left[\frac{\theta_2}{2}\right]}{\mathrm{R2}} & 1 \end{pmatrix} * \begin{pmatrix} 1 & 2\mathrm{L2} \\ 0 & 1 \end{pmatrix} * \begin{pmatrix} 1 & 0 \\ -\frac{2\mathrm{Sec}\left[\frac{\theta_2}{2}\right]}{\mathrm{R2}} & 1 \end{pmatrix} * \begin{pmatrix} 1 & \mathrm{d2} \\ 0 & 1 \end{pmatrix} *$$
$$\begin{pmatrix} 1 & \frac{\sqrt{1+n^2}t}{n^4} \\ 0 & 1 \end{pmatrix} * \begin{pmatrix} 1 & \mathrm{d1} \\ 0 & 1 \end{pmatrix} * \begin{pmatrix} 1 & 0 \\ -\frac{2\mathrm{Sec}\left[\frac{\theta_1}{2}\right]}{\mathrm{R1}} & 1 \end{pmatrix} * \begin{pmatrix} 1 & 2\mathrm{L1} \\ 0 & 1 \end{pmatrix} * \begin{pmatrix} 1 & 0 \\ -\frac{2\mathrm{Sec}\left[\frac{\theta_2}{2}\right]}{\mathrm{R1}} & 1 \end{pmatrix} * \begin{pmatrix} 1 & \mathrm{d1} \\ 0 & 1 \end{pmatrix} *$$
$$\begin{pmatrix} 1 & \frac{\sqrt{1+n^2}t/2}{n^4} \\ 0 & 1 \end{pmatrix} \tag{2.32}$$

The ABCD matrix for a complete round trip through the cavity in sagittal plane is given by,

$$\begin{pmatrix} 1 & \frac{\frac{\sqrt{1+n^2}t/2}{2}}{n^2} \\ 0 & 1 \end{pmatrix} * \begin{pmatrix} 1 & 0 \\ -\frac{2\mathrm{Cos}\left[\frac{\theta_2}{2}\right]}{\mathrm{R2}} & 1 \end{pmatrix} * \begin{pmatrix} 1 & 2\mathrm{L2} \\ 0 & 1 \end{pmatrix} * \begin{pmatrix} 1 & 0 \\ -\frac{2\mathrm{Cos}\left[\frac{\theta_2}{2}\right]}{\mathrm{R2}} & 1 \end{pmatrix} * \begin{pmatrix} 1 & \mathrm{d2} \\ 0 & 1 \end{pmatrix} *$$
$$\begin{pmatrix} 1 & \frac{\sqrt{1+n^2}t}{n^2} \\ 0 & 1 \end{pmatrix} * \begin{pmatrix} 1 & \mathrm{d1} \\ 0 & 1 \end{pmatrix} * \begin{pmatrix} 1 & 0 \\ -\frac{2\mathrm{Cos}\left[\frac{\theta_2}{2}\right]}{\mathrm{R1}} & 1 \end{pmatrix} * \begin{pmatrix} 1 & 2\mathrm{L1} \\ 0 & 1 \end{pmatrix} * \begin{pmatrix} 1 & 0 \\ -\frac{2\mathrm{Cos}\left[\frac{\theta_2}{2}\right]}{\mathrm{R1}} & 1 \end{pmatrix} * \begin{pmatrix} 1 & \mathrm{d1} \\ 0 & 1 \end{pmatrix} *$$
$$\begin{pmatrix} 1 & \frac{\sqrt{1+n^2}t/2}{n^2} \\ 0 & 1 \end{pmatrix} * \begin{pmatrix} 1 & \frac{\frac{\sqrt{1+n^2}t/2}{2}}{n^2} \\ 0 & 1 \end{pmatrix} \tag{2.33}$$

There are two ways to figure out the stability criterion, the first is to use the expression for stability criteria using Eq. 2.31, which is,

$$0 \le \frac{\frac{A+D}{2}+1}{2} \le 1 \tag{2.34}$$

where A+D is the trace of the matrix 2.32 and 2.33. Now we plot the quantity $\frac{\frac{A+D}{2}+1}{2}$ for both the tangential plane and sagittal plane by adjusting the angle of incidence on the two curved so that both regions get well overlapped. The angle of best overlap is found to be at ~θ=15º, angle

of incidence on the mirrors. The combined plot of the both planes where d_1 and d_2 are varied from 4 cm to 6 cm is shown in the Fig. 2.15. The contour plot shows that there is the region where the beam profile on both the tangential and sagittal plane overlaps.

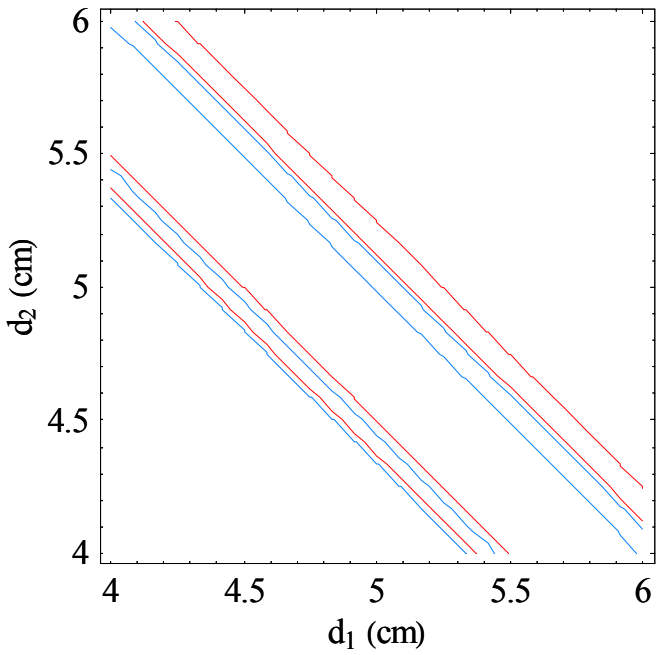

Figure 2.15. The contour plot shows that there is only one stability region inside our Cr:forsterite laser cavity where beam profile on both the tangential (blue stripe) and sagittal plane (red stripe) overlaps.

Another way to find the stability region is to look at the formula for the beam waist, ω, which is given by relation,

$$\omega^2 = \pm\frac{\lambda}{\pi n}\frac{B}{q_0\sqrt{1-\left(\frac{A+D}{2}\right)^2}} \tag{2.35}$$

This expression also enables us to calculate the laser beam size inside the crystal. When the imaginary part of this beam waist expression given in Eq. 2.35 is zero, one can obtain physically meaningful beam size.

Figure 2.16 shows the stability regions and beam waists ω_0 as a function of d_1 and d_2, which are the distances between the crystal and curved mirrors. From the result we find the

optimum combination of d_1 and d_2 where the beam radius at the laser crystal strongly shrinks due to the Kerr lens effect. In the graph above dotted line (green) above the X-axis indicated imaginary part of the beam size inside the crystal in tangential plane whereas solid line (red) is the real part of the beam size in the tangential plane. Similarly, below the X-axis we have real and imaginary beam size in the sagittal plane. There is a region somewhere in between 4.5 cm and 5 cm where the imaginary part vanishes, which gives the real beam size. We have adjusted the angle of incidence on the two curved mirrors so that the beam profiles in both the tangential and sagittal plane overlap in order to avoid astigmatism. From the simulation, we have found that the angle of incidence of the curve mirror should be $\theta = \sim 15^0$, to compensate astigmatism inside the cavity and beam size inside the crystal is 26 μm.

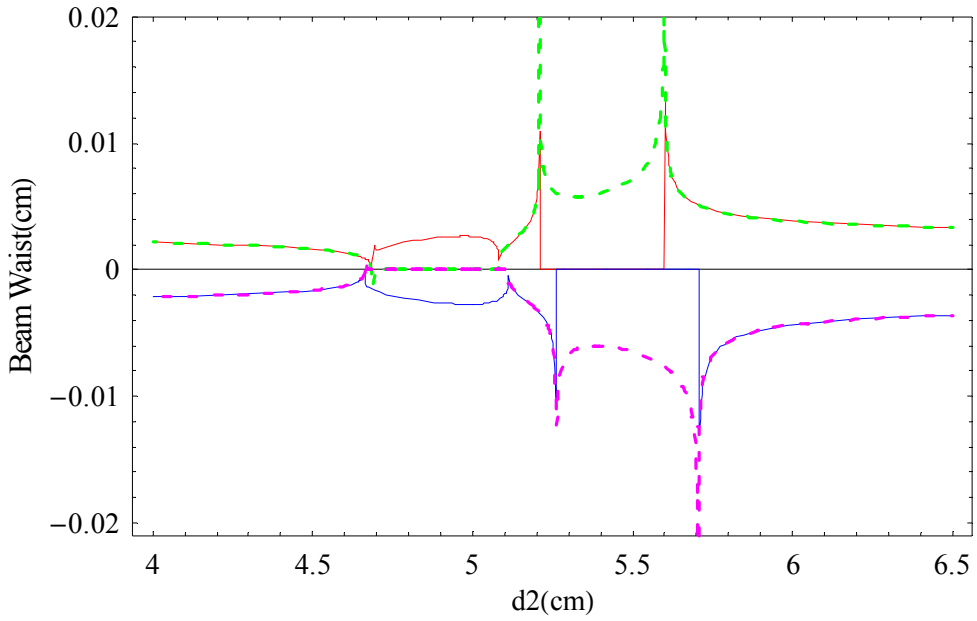

Figure 2.16. Stability regions and beam waists as a function of d_1 and d_2, distance between the crystal and curved mirrors. Real part of the beam size is indicated by the solid line and imaginary part by dotted line in both the sagittal (above x-axis in graph) and tangential plane (below x-axis is graph).

CHAPTER 3 - The femtosecond Cr:forsterite frequency comb stabilization

The optical frequency comb produced from phase stabilized mode-locked laser [66] has permitted the determination of optical frequencies with unprecedented precision [67, 68]. Recently Ti:sapphire laser systems that directly produce octave-spanning frequency combs have also been demonstrated [69-72]. The high frequency resolution available using stabilized lasers has allowed for experimental investigation into various aspects of fundamental physics [73] such as gravitational wave detection [74], time variation of fundamental constants [75] , and quantum electrodynamics [76]. Besides this, the techniques pioneered in precision measurement have also led to advances in optical communication[77], measurements of absolute optical frequencies and precision laser spectroscopy [78], development of optical atomic clocks [79, 80], optical frequency synthesis [81] and broadband, phase-coherent spectral generation [71, 82], along with coherent synthesis of optical pulses [83], phase-sensitive extreme nonlinear optics [84] and pulse timing stabilization. The main problem with using a pulsed laser for spectroscopy is the broad frequency bandwidth associated with a short pulse. The broad spectrum prevents high precision measurements. This problem can be avoided by using a train of phase-coherent pulses, which permits frequency resolution orders of magnitude better than that associated with a single pulse. Many new technologies have been enabled by the phase-stabilization of femtosecond lasers.

The series of pulses from mode-locked laser in time domain acts like a comb in frequency domain; it is therefore called frequency comb. Correspondence of time and frequency domain of the modelocked laser is shown in Fig. 3.1. Frequency comb can be described using two independent quantities: the laser repetition frequency (f_r) and the carrier envelope offset frequency (f_0). Any tooth of the comb (f_n) can be described exactly using Eq. (3.1) and the stabilization of f_r and f_0 simultaneously ensures that all the teeth of a comb occupy well defined and fixed frequency locations.

$$f_n = f_0 + nf_r \tag{3.1}$$

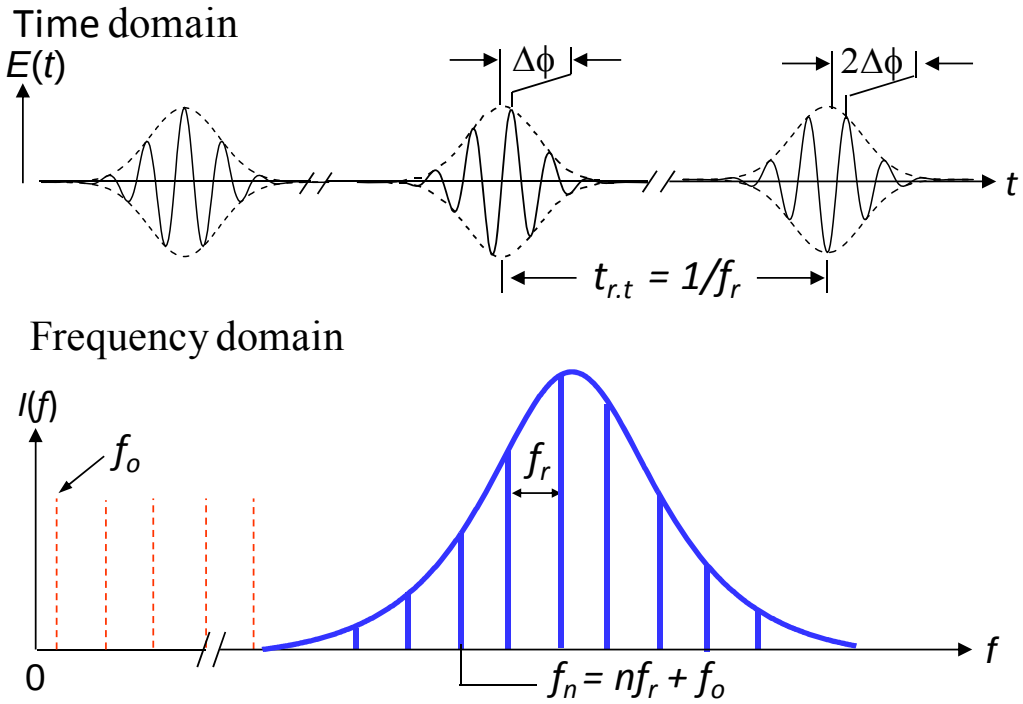

Figure 3.1. Time and frequency domain representation of mode-locked laser. In time domain the carrier-envelope phase changes at a defined rate between pulse to pulse and give rise to the carrier-envelope offset frequency, f_0 in frequency domain. In frequency domain, comb lines are spaced by the laser repetition rate, f_r determined by the round trip time, $t_{r,t}$ of the laser pulse inside the cavity.

The repetition frequency is often trivial to stabilize, generally only requiring high speed cavity length control offered by PZT mounting of the end mirror controlled by fast servo electronics. Control of f_0 however is generally nontrivial and the choice of intracavity dispersion compensation scheme in a laser cavity often determines the control mechanisms for its stabilization. Regardless of the mechanism used in stabilizing f_0, the intensity-related dynamics of f_0 is of considerable importance as it governs the stability of the entire comb. The intensity-related dynamics of f_0 in Ti:sapphire frequency combs in both prism based systems and chirped mirror based systems have previously been investigated [85] and it was noted that the f_0 dynamics were different for the two cases and depended on certain operational characteristics. The chirped mirror configuration demonstrated a roughly linear change in f_0 response and contained a zero crossing point with a reversal in the sign of the response. It was however found to be relatively easy to stabilize f_0 using pump power modulation for comparatively broad f_0

linewidth. Conversely the prism based configuration did not show any reversal of the response sign and exhibited narrower linewidth throughout but was considerably more difficult to servo using pump power modulation [85, 86]. To date there has been no such reported study for a Cr: forsterite laser and consequently the intensity related dynamics of f_0 are as yet undetermined.

The linewidth of the detected f_0 signal is often attributed to the level of intensity noise present on the pump laser [87] but it can also depend on the cavity configuration. For example Ref. [87] reported broad f_0 signals with widths of 6.7 MHz FWHM when using a chirped mirror based Cr:forsterite. In this paper, we report on a prism-based Cr: forsterite laser system with f_0 linewidth of the order of ~1.5 MHz in spite of employing a similar pump laser. This is in agreement with that seen in Ti:sapphire systems [86] with the addition that the stabilization of our prism-based Cr:forsterite comb required the inclusion of an intracavity prism modulation scheme in conjunction with power modulation. We have also seen a dramatic reduction in linewidth from ~2 MHz to ~20 kHz in the carrier envelope offset frequency of a femtosecond Cr:forsterite comb due to insertion of knife edge in front of the end mirror inside the cavity. Insertion of the knife edge also shifts the central frequency of the laser as well as the amplitude of the beat note. We believe this change in f_0 linewidth may be due to change in intracavity dispersion and change in wavelength dependent intracavity loss. But, the exact cause of the narrowing remains unexplained. In this Chapter we presented the results of the stabilization of our self-referenced prism-based mode-locked Cr:forsterite system and a study of the intensity related dynamics of the frequency comb in terms of both f_0 and f_r. We have also measured the approach used for phase stabilization and a discussion of the f_0 linewidth and stability that was achieved. Furthermore, the fractional stability of the stabilized Cr:forsterite comb was determined using in-loop and out of loop measurements.

3.1. A self-referenced prism based Cr:forsterite comb

Cr:forsterite lasers have previously been phase stabilized and used for infrared frequency measurements using two different cavity configurations: one employing a prism-pair for dispersion compensation [88] and another employing chirped mirrors [89, 90]. Chirped mirror based lasers are generally more compact and can generate higher repetition rate combs but are limited with regards to their ability to change output characteristics. Prism based systems on the

other hand allow for more control over intracavity dispersion and enable a greater flexibility in the output characteristics. Unfortunately this flexibility comes at the cost of greater complexity with regards to the phase stabilization of the frequency comb. For instance, a common technique used in the stabilization of chirped mirror combs is to use pump power changes to differentially affect the group velocity and phase velocity of the propagating pulses. A change in the pump power effects the overall intracavity dispersion by changing both the linear and nonlinear refractive index of the gain medium but for prism based systems there is also a change in the intracavity beam path through the dispersion prisms [91] which alters their contributions to the total linear refractive index.

3.1.1. Cavity configuration

The cavity configuration of the prism-based Cr:forsterite laser is shown in Fig.3.2 which includes a 10W Ytterbium fiber pump laser (IPG Photonics) that operates at 1075 nm with a spectral bandwidth of ~3 nm. The pump is then directed through an acousto-optic modulator (AOM) to enable pump power modulation for f_0 control before being focused into a 15 mm long Brewster cut Cr:forsterite crystal using a 10 cm focal length lens. Two 100 mm radius of curvature (ROC) cavity mirrors, M_1 and M_2, then maintain an intracavity beam focus calculated to have a spot size of radius ~18 μm within the crystal, which has the same bulk properties as that used in Ref. [62] (doping of 0.2% by weight, absorption coefficient α = 1.1 cm^{-1} at 1075 nm). As described in Chapter 2, dispersion compensation is achieved using a pair of intracavity SF6 prisms, Brewster cut for 1250 nm, mounted on translational stages and separated by ~ 30 cm. The high reflecting end mirror was then initially mounted onto a high-response PZT (f_{3dB} ~ 30 kHz) to enable fast servo control of f_r. Astigmatic aberration compensation requires the two cavity mirrors (M1 and M2) be angled at a relatively large angle of ~30°. A 6% output coupler is then used to extract ~300 mW of mode-locked power for 8W of pump power at a crystal temperature of 263 K and autocorrelations reveal pulses with ~40 fs duration for a ~45 nm spectral bandwidth (transform limited case yields 37.6 fs for this bandwidth). The repetition rate of the laser was 117 MHz.

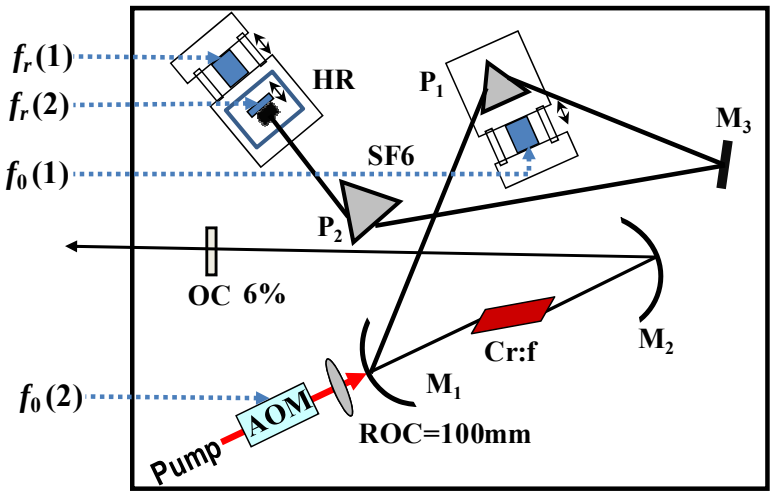

Figure 3.2. Schematic of the prism-based Cr:forsterite laser cavity (OC=output coupler, ROC=radius of curvature, HR=High reflector, cavity mirrors= M_1 & M_2, SF6 dispersion prisms=P_1 & P_2) including the four components used for servo control of both f_r and f_0. $f_r(1)$ and $f_0(1)$ offer slow speed control while $f_r(2)$ and $f_0(2)$ allow higher speed control

Mode locked operation is achieved by dithering the second prism (P_2) using a computer controlled stepper motor and once optimized, mode-locking can be regularly observed uninterrupted over a period of a week. The laser is enclosed in a Plexiglas box and is purged with dry nitrogen to prevent water condensation on the crystal surface and it also helps to maintain a constant environment that aids in ensuring a consistent performance of the laser.

As will be discussed later in section 3, AOM modulation alone was insufficient to stabilize f_0 due to large excursions and so an additional servo control system was needed to allow more significant control. A small Piezoelectric Transducer (PZT) (with ~ 4 μm of movement) was inserted into the translational mount of an intracavity prism (P_1) at the tip of the micrometer to enable the prism insertion to be modulated at slow speeds (<1 kHz) and produce large shifts in f_0. These two control mechanisms allow for both coarse (slow) and fine (fast) control of f_0 simultaneously and allow f_0 to be appropriately stabilized but the prism modulation has an additional effect on f_r stabilization. To compensate for the prism insertion f_r required additional servo control which was achieved by way of inserting a large PZT (with ~10 μm of movement) at the tip of the micrometer used for moving the high reflecting cavity end mirror. This allowed f_r to be shifted at slow speeds (<1 kHz) in response to the slow prism modulation and added extra dynamic range to f_r control to help compensate for environmental conditions that cause it to drift over long time periods (hours).

For self-referenced f_0 detection the laser output is directed into a dispersion-shifted highly nonlinear fiber (HNLF) [92] with dispersion D = 1.19 ps/(nm km) at 1550 nm, where 130 mW of average power emerges and has a supercontinuum spectrum that spans more than an optical octave. The supercontinuum output is shown in Fig. 3.3 and contains two measurements of the spectral coverage due to wavelength response limitations of the equipment used for the detection. The main plot in that figure shows the data recorded using an optical spectrum analyzer (HP8361A) which has a wavelength cut off at 1700 nm. While the inset of Fig. 3.3 shows a portion of the supercontinuum signal above the cut-off of the optical spectrum analyzer recorded using a monochromatic spectrometer and shows that a portion of the supercontinuum covers ~ 2050 - 2220 nm.

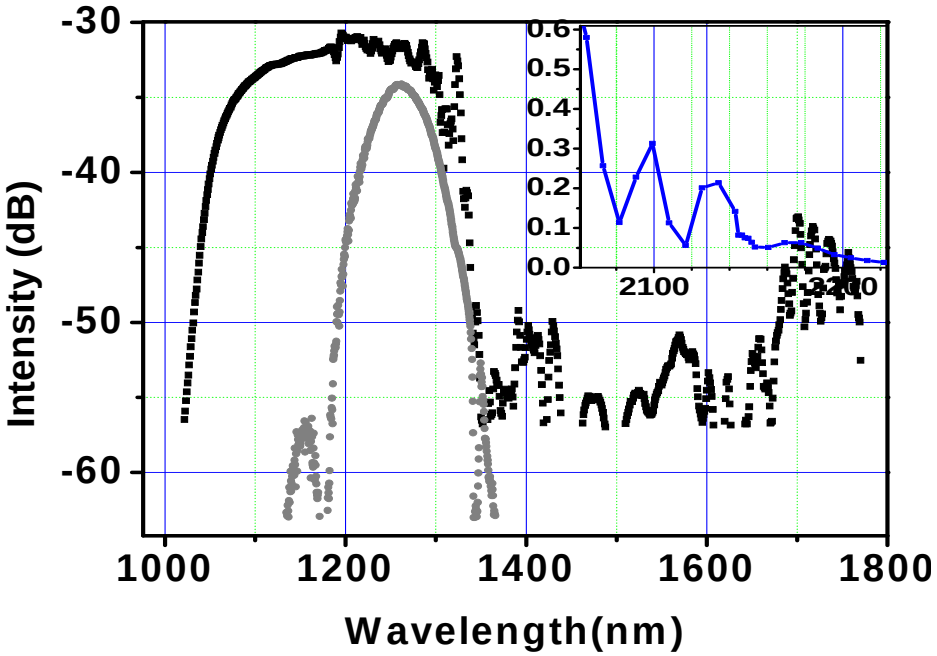

Figure 3.3. Laser spectrum (grey) and supercontinuum spectrum (black). The main plot shows the OSA measured signal with a cut-off at 1700 nm due to the internal detector and the inset shows the signal measured beyond 1700 nm using a monochromator revealing a large peak at ~ 2060 nm.

Once generated, the supercontinuum is then directed into an *f*-2*f* interferometer where a section of the signal at 1030 nm is mixed with the second harmonic of the signal at 2060 nm to directly retrieve f_0. A 10 mm long crystal of periodically poled lithium niobate (PPLN) with a 30 μm grating period is used to generate the second harmonic signal and is held at a temperature of 150°C to optimize conversion efficiency. After detection the f_0 signal was recorded showing a

signal-to-noise ratio of ~40 dB and a linewidth of ~1.5 MHz. A schematic of the *f*-2*f* interferometer is shown in Fig. 3.4 and both f_r and f_0 were detected simultaneously using a pair of 125 MHz InGaAs photodetectors. The detected signals were then input into a pair of frequency counters for recording via GPIB connection to a computer.

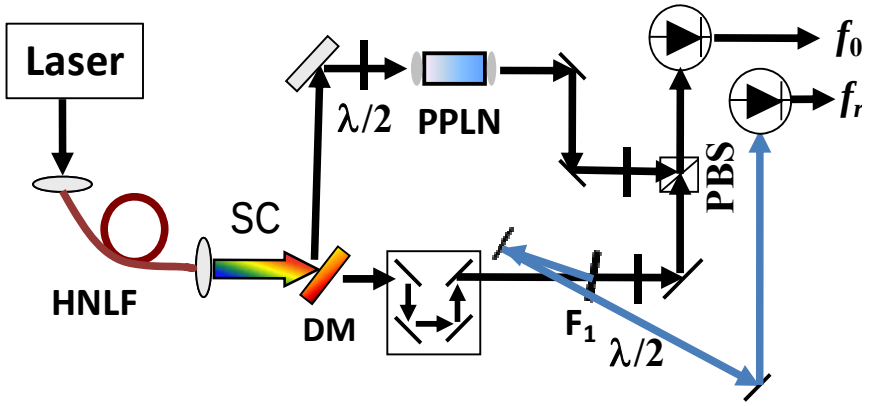

Figure 3.4. Schematics of the *f-2f* interferometer used for the self-referenced detection of f_0. (HNLF =highly nonlinear fiber, SC=supercontinuum, DM=dichroic mirror, F_1=1030 nm bandpass filter, PBS=polarization beam splitter cube) A surface reflection from the band pass filter, F_1 is used for f_r detection.

3.1.2. Phase-stabilization of Cr:forsterite laser

In order to stabilize the entire frequency comb both f_r and f_0 need to be stabilized. In the case of f_r, the detected signal is mixed with a synthesizer at ~ 117 MHz; phase detection generates an error signal which is converted to an output signal that drives the PZT mounted end mirror in order to change the cavity length and hence f_r and minimize the error signal. Control of the cavity length is straightforward and high accuracy control of f_r is possible using relatively simple but high speed electronics. The carrier envelope offset signal however is a different matter. Before any phase detection can be implemented, the f_0 signal is first sent through a 50 MHz low-pass filter (LPF) and then mixed with a 1 GHz synthesizer signal where the resulting signal is filtered, amplified and frequency divided (by a factor of 120). At this point the resultant signal is phase compared to a second synthesizer (set at ~16.8 MHz for f_0 locked at 35 MHz) and used to generate an error signal for use to vary the pump power input into the Cr:forsterite crystal. Figure 3.5 is a schematic of the servo control loops used to control both the fast and slow circuits for f_r and f_0 control and Fig. 3.2 shows what component of the laser cavity setup was modulated for the appropriate signal control.

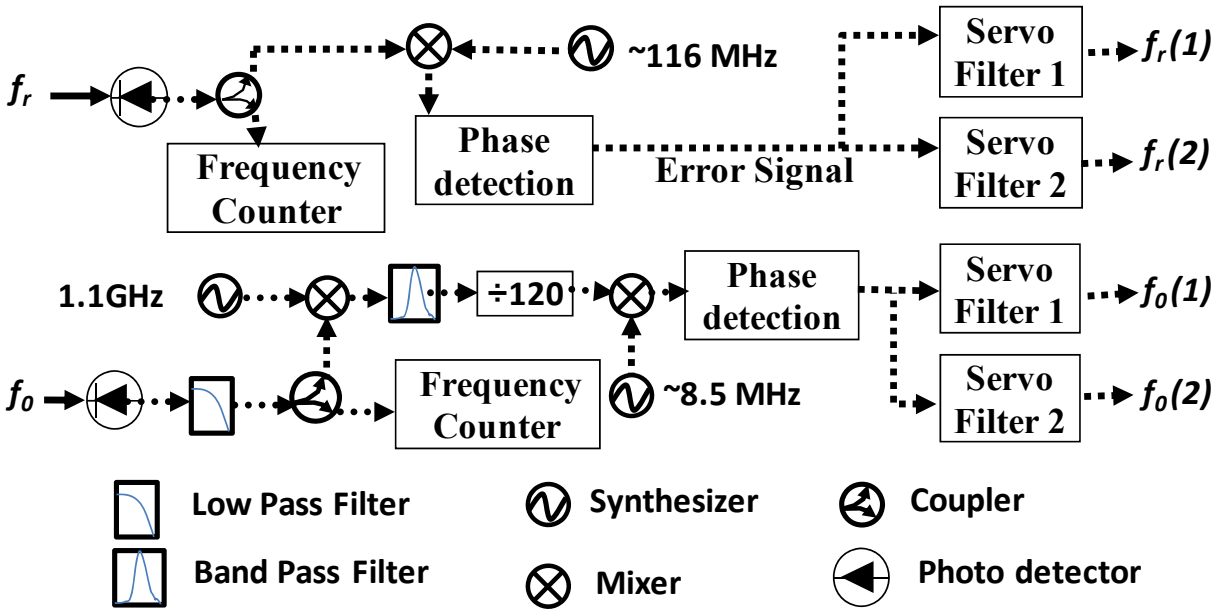

Figure 3.5. RF electronics used for servo control of f_0 and f_r. In both the f_0 and f_r case a slow (indicated by a 1) and fast (indicated by a 2) servo signal.

Unlike the case for many Ti:sapphire lasers, Cr:forsterite has a narrow power operating range over which mode-locked operation can be maintained. In our case we cannot change the 10 W pump power by more than 5% when modulating at slow speeds (less than a few kHz). This means that for our system power modulation alone is insufficient to control f_0 while maintaining a mode-locked output due to frequent large and slow fluctuations in beat note frequency. Therefore a second method is required that does not affect the input pump power but allows f_0 to be changed by large amounts at relatively slow speeds. This was achieved by modulating the insertion of an intracavity prism (P_1 in Fig.3.2) which affects both the group and phase velocity of the intracavity pulse and changes both f_0 and f_r without detrimental effects on the mode-locked operation of the laser. In combination, prism modulation and power modulation significantly changed f_0 at both fast and slow speeds, but they do not compete.

Initially the f_0 phase detection error signal was used to drive prism P_1 at slow speeds (<1 kHz) and resulted in a 'loose' lock on f_0 by removing slow but large fluctuations, $f_0(1)$. After this the remaining error signal was ac-coupled into a second servo circuit which modulated the AOM and the input power of the pump laser and 'tightened' the f_0 lock, $f_0(2)$. This combined approach

enabled f_0 to be stabilized to within ~1 Hz of the reference signal and held at 35 MHz for 2-3 hours. Clearly there are drawbacks to this approach, the main one being that changes in the prism insertion also affect the cavity length and degrade f_r stability and slow variations in the prism insertion were problematic for the f_r servo circuit due to its gain at low frequencies. Therefore additional slow servo capability was also required for f_r to counteract the prism modulation and could also be used to counteract slow temperature fluctuations in the lab beyond the capability of the short range PZT mounted to the HR end mirror. An additional, larger PZT was integrated into the translational stage of the end mirror mount and was controlled by a slow loop filter to remove the slow fluctuations introduced by the prism modulation for f_0 locking. Again to ensure no competition between the two f_r servos the error signal generated by the phase difference between the detected RF signal and the reference synthesizer was first used in the slow servo circuit, $f_r(1)$, to drive the large PZT and the residual error signal was ac-coupled into a second faster servo circuit, $f_r(2)$, to drive the small PZT. Combining the fast and slow servos it was possible to measure a counter limited f_r signal that was within 1 mHz of the synthesizer signal. Lastly, all three synthesizers used for f_r and f_0 stabilization were referenced to a commercial GPS-disciplined rubidium oscillator offering a long-term stability of ~ 10^{-13} at a gate time of 1s for a week. After stabilizing the comb the f_0 linewidth was recorded using an RF spectrum analyzer and a linewidth of ~1.5 MHz was measured (Fig. 3.6).

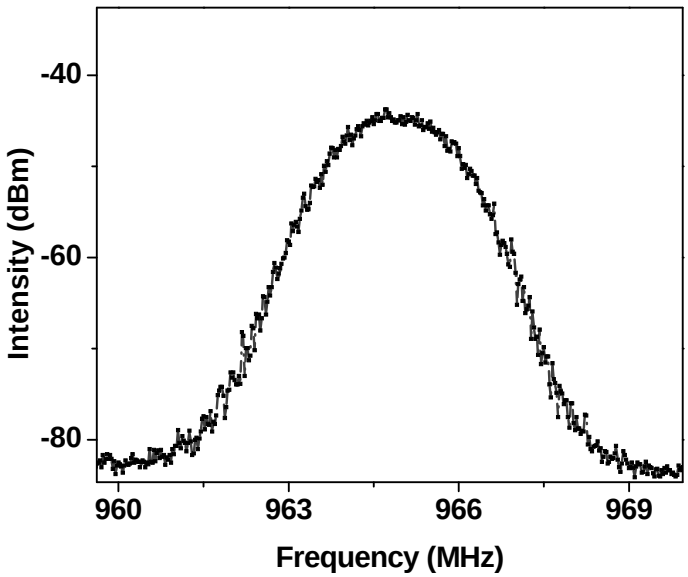

Figure 3.6: Detected f_0 signal, with S/N ~ 40 dB and a FWHM linewidth ~ 1.5 MHz (RBW = 100 kHz)

Previous work involving the stabilization of a 420 MHz chirped-mirror based Cr:forsterite laser [87] had demonstrated an unusually broad linewidth of 6.7 MHz which was attributed to noise during supercontinuum generation seeded by the intensity noise on pump laser. Here a similar pump laser has been used with an alternative dispersion compensation scheme and a narrower linewidth has been measured. In both cases the pump laser is a commercial 10 W CW Yb:fiber laser operating at 1075 nm with a spectral bandwidth of ~3 nm (IPG Photonics). The pump laser contains multiple longitudinal modes generating a suppressed noise spike at ~3.5 MHz which potentially results in a ~10% fluctuation in output power. But these higher frequency spikes do not have much effect on the performance of the laser since the laser frequency response is almost negligible at these frequencies.

3.1.3. Intensity-related dynamics of the carrier-envelope offset frequency

The relationship between f_0 width and pump power laser intensity fluctuation has been studied by many groups. This is basically a study of response of f_r and f_0 to pump power changes. A detailed study of the intensity related dynamics of a Ti:sapphire frequency comb [85] has shown

that prism-based systems are less responsive to pump power fluctuations and intrinsically exhibit a narrower f_0 linewidth than chirped mirror based systems. In such a system utilizing prism pairs, we optimize the cavity to achieve near-zero net cavity dispersion. The consequence of this is that prism based systems are more difficult to stabilize using a servo controlled AOM. The study presented in Ref. [85] demonstrated explicitly that f_0 linewidth increased linearly with an increased dependence of f_0 on pump intensity changes (df_0/dI) and can be accompanied by a sign reversal in both the f_r and f_0 response. These dynamics can be explained by considering a corresponding shift in the spectrum of the laser pulse. In prism-based systems, mode-locking conditions can be found under which the intensity-related spectral shift or the magnitude of GDD is minimized, thereby minimizing the noise on both f_r and f_0 and giving narrower f_0 linewidths.

Washburn *et al* [93] have also studied the intensity related response dynamics using Erbium as a gain medium; they have found that the response of the gain medium was also an important determining factor for the linewidth of f_0. For systems where the response rolled off at lower frequencies, the linewidth of f_0 was narrower. The roll-off frequency in Er:fiber lasers differed depending on the cavity configuration that was used but occurred at around 10 kHz whereas for Ti:sapphire laser it was measured at a much higher frequency of ~800 kHz [94]. Another important factor in determining the linewidth of f_0 is the relative intensity noise (RIN) of the laser systems being used, meaning both the pump laser and the femtosecond laser [95]. McFerran *et al* [96] reported that the linewidth of f_0 in fiber lasers can mainly be attributed to white amplitude noise on the pump diode laser leading to a breathing-like motion of the comb about a fixed frequency [96]. This effect can be observed in the wings of the comb where optical linewidth of fiber-laser frequency teeth are particularly large. Using these factors to develop an understanding of laser dynamics means there are strong implications to the optimal use of pump power variation to control f_0 and f_r. In an attempt to better understand the intensity related dynamics of f_0 in a prism-based Cr:forsterite system and to make use of power modulation as a stabilization approach, a study of the key influential factors determining our f_0 linewidth was required.

Prism-based lasers are known to exhibit significant variations in the strength of their f_0 response to power fluctuations (df_0/dP) depending on often small and subtle changes to the total intracavity dispersion [86]. By understanding the resulting variation in the Cr:forsterite medium it may be possible to chose an appropriate configuration where a strong response is detected and

use it to stabilize the comb. Based on the work of previous groups [86, 93-97], three key influential factors can be identified which include: laser RIN (pump and the femtosecond laser), the response roll off frequency (f_{-3dB}) and the gain medium power response (df_0/dP). RIN is a relatively simple measurement to make in that once the output from the laser cavity is incident onto a fast photo detector it is simple to record the RIN over a given range using a frequency spectrum analyzer. For our measurements 100 kHz segments were recorded (RBW=1 kHz) covering 0 – 3 MHz for the two cases of the pump laser alone (Yb:fiber) and the combination of the Cr:forsterite laser and pump laser. The data recorded is presented in Fig. 3.7 where the red trace shows the pump noise only, the black trace shows the combined Cr:forsterite and pump noise and the blue trace shows the Cr:forsterite noise only (calculated by subtracting the pump noise from the combined noise). The RIN of Cr:forsterite only shows a 3dB roll-off in the signal at around 700 kHz which is similar to that measured in Ti:sapphire [94].

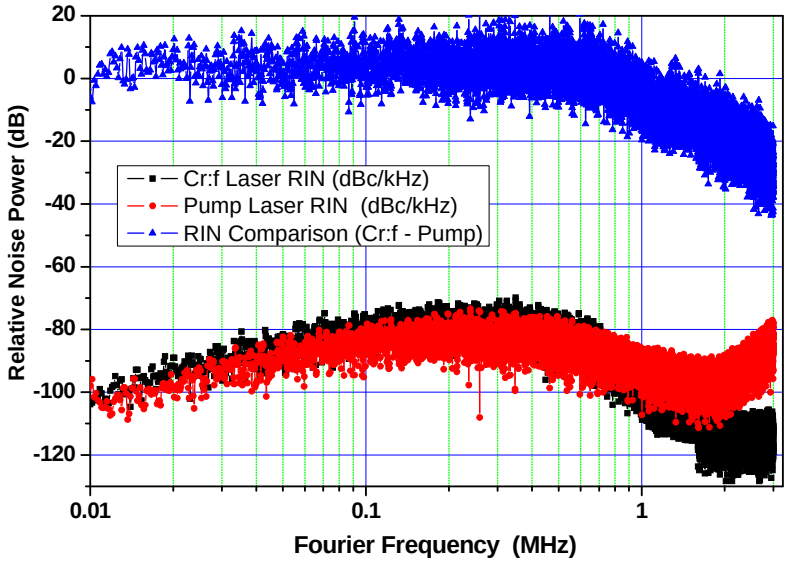

Figure 3.7. Pump RIN (Red circles), Cr:forsterite RIN (black squares) and comparison of Cr:forsterite and pump RIN (Blue triangles) plotted as a function of detection frequency.

The alternative technique involved first locking f_0 and then modulating the pump power at a range of frequencies and measuring how the modulation broadened the linewidth of the locked signal. At frequencies below 700 kHz the locked linewidth saw significant broadening effects that were reduced as the modulation frequency rose above 700 kHz and were virtually undetectable above 1 MHz.

Figure 3.7 shows that the response of Cr:forsterite to pump power fluctuations greatly diminishes above 700 kHz and indicated that what was previously considered one of the key noise sources, the pump laser, was not in fact a significant contributor to the linewidth of the f_0 signal. Namely that the noise spike at 3.5 MHz due to longitudinal modebeating within the Yb:fiber cavity was not significantly influencing the comb stability.

Another necessary measurement was to find the response of the Cr:forsterite f_0 signal to pump power fluctuations, df_0/dP, which would also give an indication of the change in f_0 linewidth introduced by modulating the pump power for f_0 control. This measurement was initially made by recording changes in the position of f_0 using a known pump power change (i.e. $\Delta f_0/\Delta P$) for a range of different intracavity prism positions. Additionally the prism itself was modulated about each of the different center positions and a change in f_0 was also recorded. Figure 3.8 shows a schematic of the setup used for the AOM modulation experiment where a square wave signal at 3 Hz was applied to the AOM to change the input power by a known amount of ~150 mW.

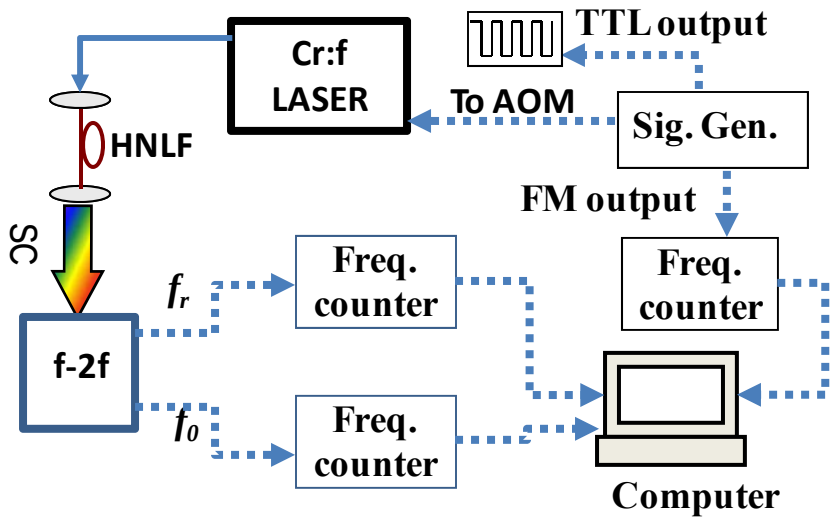

Figure 3.8: Experimental configuration used to make $\Delta f_0/\Delta P$ measurements as a function of relative prism insertion. Pump power changes were made using AOM modulation (ΔP) at different fixed prism positions and a change in f_0 position was recorded (Δf_0).

Two such measurements are shown in Fig. 3.9 where amplitude and frequency of modulation to AOM are similar at two different prism positions; we can clearly see the reduction in beat note response.

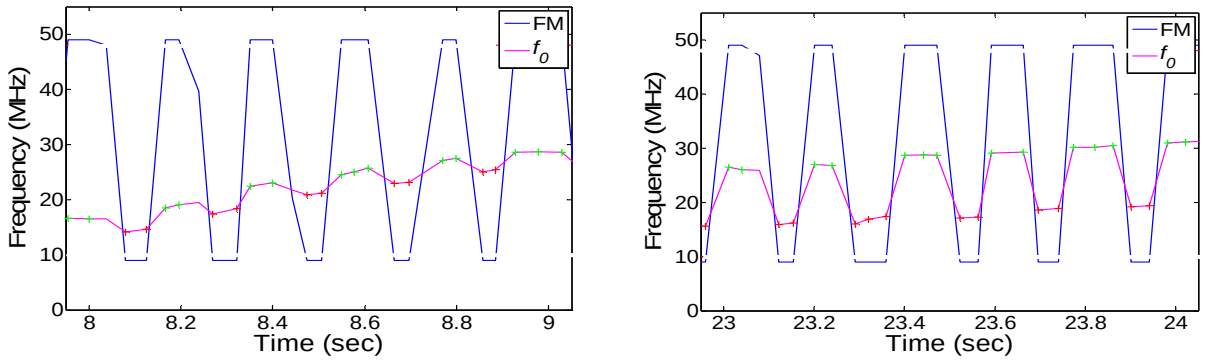

Figure 3.9. Effect of power modulation at different prism insertion inside the cavity. Blue line is the frequency of modulation applied to the AOM and Red is the response of the f_0 measured at two different prism positions.

Fourteen different prism positions were used, each separated by 50 μm which for SF6 glass corresponds to a group delay dispersion (GDD) difference of ~6.36 fs^2 per position changing the spectral bandwidth of the output pulses from 30-45 nm. Figure 3.10 shows the results of this experiment with Fig. 3.10a showing the results of the AOM modulation and Fig. 3.10b show the results of the prism modulation. In Fig. 3.10a significant variation in $\Delta f_0/\Delta P$ as a function of the prism position is clearly evident whereas the response of f_0 to prism modulation is virtually uniform throughout.

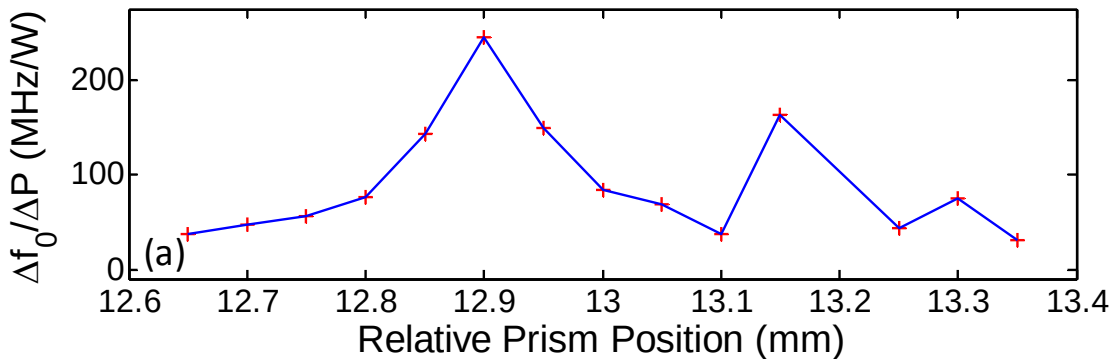

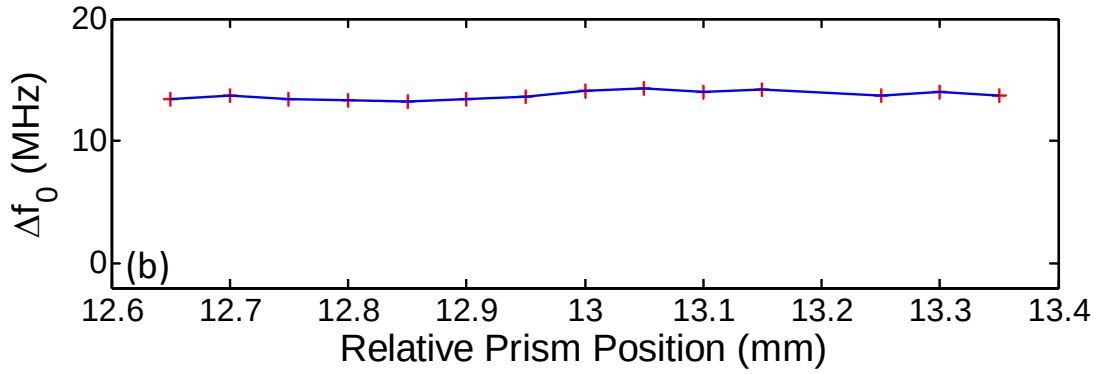

Figure 3.10. a) Response of f_0 to power modulations for different fixed prism settings where a maximum of 250 MHz/W was recorded (a prism position change of 0.1 mm results in a change in cavity GDD of ~ 12.72 fs^2 for SF6) b) Response of the f_0 to changes in prism insertion for different prism positions (~ 13.5 MHz throughout).

Prior to making this measurement it was difficult to stabilize f_0 due to a small df_0/dP response and large but slow fluctuations (10's of MHz) in its frequency. Consequently the servo circuit used large pump power changes at slow speeds to attempt to compensate for the changes which were sufficient to force the Cr:forsterite laser out of mode-locked operation after a few seconds. This experiment indicated that it was possible to choose a prism position where df_0/dP was maximized and enable effective servo control of f_0. Due to issues of repeatability in the actual response values measured using the previous approach an alternative technique was required to accurately quantify df_0/dP for the Cr:forsterite laser. So the idea was to measure an f_0 response using both a fast and slow modulation in pump power at a fixed prism position (or intracavity dispersion) and then calculate df_0/dP for both cases. For the fast pump power modulation measurement a previous approach was used where f_0 was locked using only the prism servo and then an AOM (f_{-3dB} response was measured to be ~ 1.2 MHz) was used to modulate the pump power at frequencies between 50 kHz and 2 MHz. The resultant f_0 linewidth was then measured on an RF spectrum analyzer and compared to an unmodulated f_0 linewidth to reveal a broadening that was attributed to the applied pump power modulation. The AOM modulation signal used throughout the fast modulation was sinusoidal with amplitude of ~5 % of the 8 W input pump power or ~350 mW peak-to-peak. For the slow pump power modulation measurement a lock-in detection approach was used to ensure only the contributions to an f_0 change arising from the AOM modulation of the pump power were detected. The basic principle

was to first lock the f_0 signal using the prism servo only and then to modulate the pump power by a known amount and then measure the increased prism servo signal needed to remove that pump power change. This required calibration of the prism servo signal to correspond to a known prism insertion indicating a known frequency and by knowing the pump power change corresponding to the applied AOM modulation signal. The lock-in amplifier and pump modulation signal were both synchronized using the same 3 Hz (100mV) signal from an external signal generator and the modulated f_0 signal was detected on a InGaAs photodiode. Figure 3.11 shows the relatively simple setup used for both the fast and slow pump power modulation experiments. The fast and slow pump modulation data agreed to within 20% of each other and resulted in a calculated value of df_0/dP of 90 MHz/W and 110 MHz/W respectively.

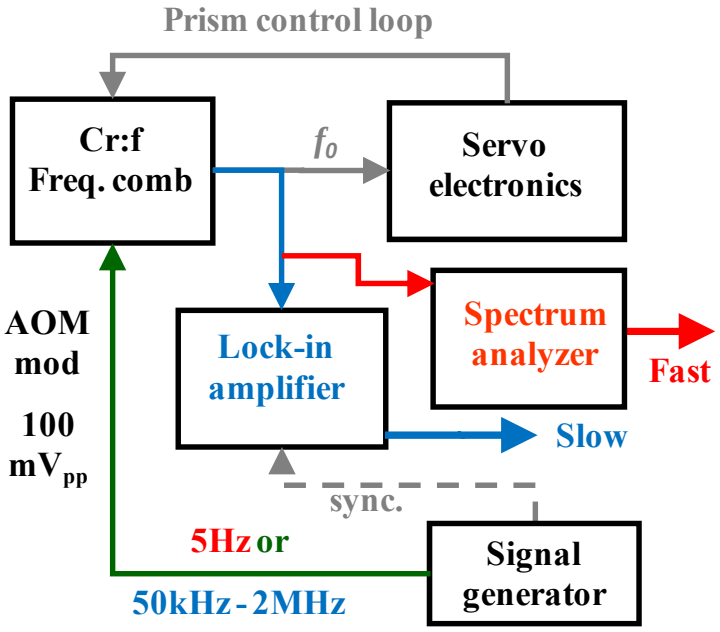

Figure 3.11. Response of the beat note f_0 to both the fast, > 50 kHz, and slow, < 50 Hz, power modulations. To measure Δf_0 for fast pump modulation, it was first stabilized to some extent using a slow-speed (<1 kHz) feedback loop to the prism insertion. An RF spectrum analyzer was used to make Δf_0 measurements. We employ a lock in detection technique with slower pump power modulation to avoid ambiguity in the measurement to observe small change f_0 width.

Both the RIN measurements and the df_0/dP measurements allowed the effect of the pump noise on f_0 width to be estimated using a similar expression to that mentioned in references [96] and [98]. This expression takes into account the three key factors mentioned previously namely RIN, the laser's response cut-off frequency (f_{-3dB}) and f_0's response to pump power fluctuations, df_0/dP. The estimated value of f_0 linewidth can be found using Eq. (3.2):

$$\Delta f_0 \cong \left(P\frac{\partial f_0}{\partial P}\right)\int_0^{f-3dB} RIN(\nu)d\nu \tag{3.2}$$

Using the previous data of df_0/dP (Fig. 3.10) and integrating area under the RIN as shown in Fig. 3.7 up to the 3dB response of laser, the estimated f_0 linewidth should be ~50 kHz which underestimate the actual f_0 linewidth of 1.5 MHz by a factor of 30 and suggests the dominating linewidth broadening mechanism for f_0 in Cr:forsterite is not the pump noise.

3.1.4. Effect of knife edge inside the cavity

We also discovered that a narrow f_0 beat is observable when a knife edge is inserted after the 2nd prism, to tune the laser to shorter wavelengths. Insertion of the knife edge also shifts the central frequency of the laser and changes the signal to noise of the beat note. There is some optimum value of the knife edge where the beat note seems to be narrower. Figure 3.12a below shows the absolute peak power of f_0 with respect to knife edge insertion. We have observed that the f_0 linewidth begins to shrink down in its width and a narrow peak begins to appear on top of a wide pedestal. For example, as shown in Fig. 3.12a, when the knife edge reaches ~225 μm of insertion towards the beam, we then begin to see the narrowing effect. At this point, the central frequency of the laser shifts to 1265 nm and the output power drops by 20 mW as shown in Fig. 3.12b. Reference position '0' is the position of the knife edge before it just begins to cut off a small section of the beam so that we can see the change in output power as well as the shift in central frequency of the laser.

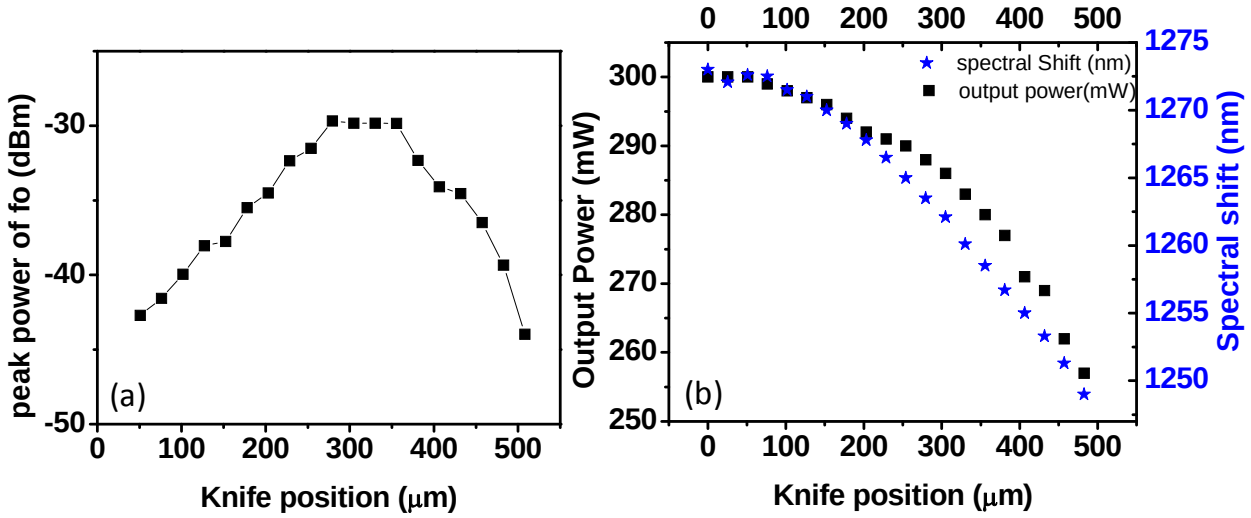

Figure 3.12 a) Absolute peak power of beat note measured in RF spectrum analyzer with the position of the knife edge towards the beam right before the pzt mounted mirror. The base value of RF signal was -76.90 dBm. RBW was 100 kHz. Pump power was 7.9 W and Average output power was ~300 mW. 0 in X-axis is some referenced value of the knife edge when the beam is unblocked. b) Output power measured using power meter. There is also a shift in the central frequency of laser output with respect to knife edge measured in spectrum analyzer.

The knife edge insertion dramatically narrows the beat note by about two orders of magnitude. Figure 3.13b shows a comparison between the narrow and wide profiles measured with and without the knife edge inserted. The data in Fig 3.13a shows a narrow linewidth of 30 kHz, which is limited by the resolution band width (RBW) of the RF spectrum analyzer. Changing the RBW to 3 kHz yielded a narrow linewidth of ~ 10 kHz (Fig 3.13b). We stabilized the laser at every position of the knife edge and measured the f_0 linewidth (Fig 3.13c). It was difficult to lock the laser at narrower linewidth; this is due to a significant decrease in response of the f_0 with change in pump power. At wider beat note, it is much easier to lock but the f_0 linewidth shows breathing like behavior and its width changes by ~0.5 MHz as shown in Fig. 3.13c.

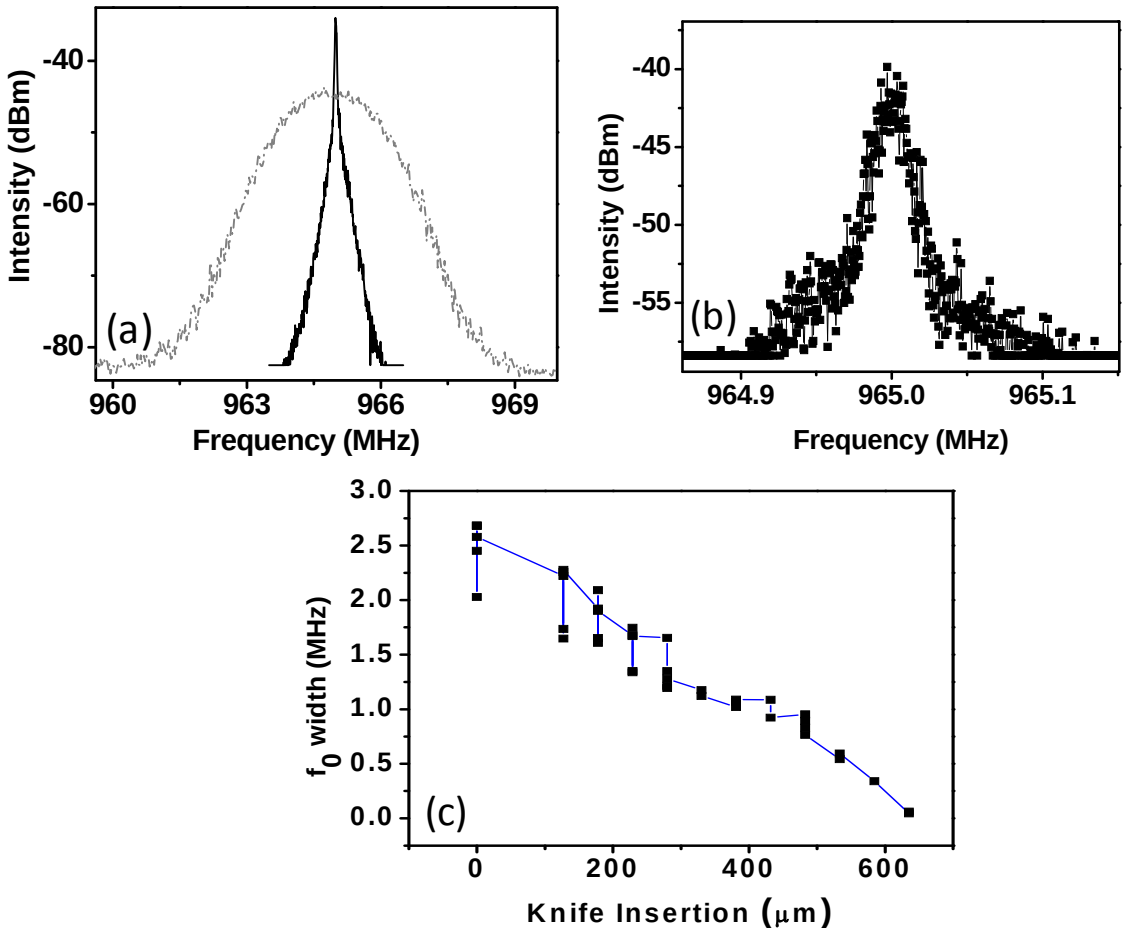

Figure 3.13 a) (black) shows narrow f_0 beat measured on RF spectrum analyzer with RBW of 30 kHz with knife edge insertion. (gray) shows wider f_0 signal without knife edge insertion measured at different time, approx ~ 1.5 MHz wide, with RBW = 100 kHz. Pump powers are similar in either case, ~ 8 W and output laser power was ~300 mW. Our pump is 1075 nm Yb doped fiber laser (IPG Photonics). b) It shows narrower signal (zoom in) with knife edge insertion, approx ~ 10 kHz wide, with RBW = 3 kHz. c) measured f_0 linewidth of the laser at various positions of the knife edge insertion inside the cavity.

We have measured the response of f_0 to the pump power for different knife edge positions; we performed both the slow and fast modulation exactly the same way it is described in section 3.1.2. The only difference is that we did not change the prism position as shown in Fig. 3.10. The data shown in Fig. 3.14 are taken at different time as compared to the data shown in Fig. 3.12 and 3.13; it is expected that the laser response will change on a day by day basis since we have to tweak the laser several times to get its stable operation. The difference is obviously

clear if we compare Fig. 3.13c and 3.14b. In the former case we changed the knife edge until we got the narrowest f_0 linewidth and we did not insert the knife edge further. In later case, we inserted the knife edge beyond the point where we get narrowest f_0 linewidth and clearly saw the broadening afterwards. We then compared the measured f_0 linewidth at every knife edge position to the estimated value of the f_0 linewidth calculated form Eq. 3.3. The calculation based on df_0/dip, f_{-3dB} and pump RIN significantly underestimates f_0 linewidth.

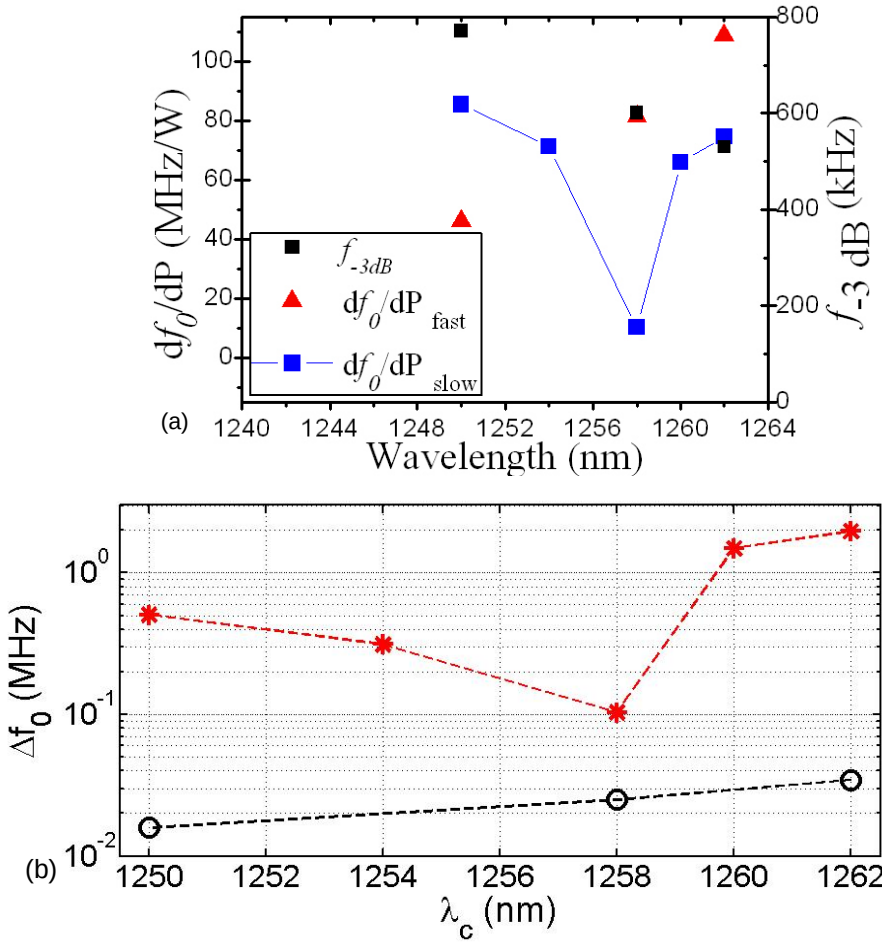

Figure 3.14 (a) slow and fast response of the f_0 to the pump power modulation. The modulation frequency of the slow modulation is 5 Hz whereas that of the fast frequency varies from 50 kHz to 2 MHz. In both the slow and fast modulations, the amplitude of the modulation is 100 mV_{P-P} which corresponds to approximately 10% change in pump power. The input pump power is ~9 W. (b) Red star in the picture is the measured f_0 linewidth and the black circle is f_0 linewidth calculated with the help of Eq. 3.2. The basic estimation of calculated f_0 linewidth underestimates the measured value.

3.1.5. Fractional stability of the Cr:forsterite comb

To measure the fractional frequency stability of the stabilized Cr:forsterite comb, both in-loop and out-of-loop stability measurements were required. To make in-loop measurements, both f_r and f_0 were counted using different gate times and a corresponding Allan deviation was calculated for each signal at each of the gate times used. The overall comb lock was relatively robust and could be maintained for several hours. However, the fractional stability of f_0 degraded if the f_r lock was optimized, as observed on the size of the servo error signal while locked. The frequency counters did not reveal any difference because they were limited to measuring 10's of μHz at 117 MHz. Consequently it was not possible to count f_r exactly but only to place an upper limit on its stability. Sometimes, during each data run, the phase lock loop of the Cr:forsterite laser comes out of lock and we need to manually relock it. This may be due to several factors such as thermal drift, pump power fluctuation, temperature of the lab etc. Most of these data were recorded and removed from the raw data. Each of this data set has been recorded for different gate time of the counter to characterize the stability of the comb by calculating Allan deviation.

Allan deviation is the non-classical statistics used to estimate stability of the clocks, oscillators and frequency standards. Allan deviation measures point to point fluctuations of the data unlike standard deviation which measures fluctuation from mean value. Allan deviation is also used to identify types of oscillator and measurement system noise. The slope of the Allan deviation vs. sampling time or gate time plot will tell you about the kind of noise in the oscillator. Allan deviation can be expressed mathematically as,

$$\text{Allan Deviation} = \sqrt{\frac{1}{2(N-1)}\sum_{i=1}^{N-1}(y_{i+1}-y_i)^2}$$

where y_i is a set of frequency measurements that consists of individual measurements, y_1, y_2, y_3, and so on; N is the number of values in the y_i series. A low Allan variance is a characteristic of a clock with good stability over the measured period of time. We use the same statistics to calculate the frequency stability of our frequency comb. The time series measurement of the data of f_0 and f_r is shown in the fig. 3.15 below.

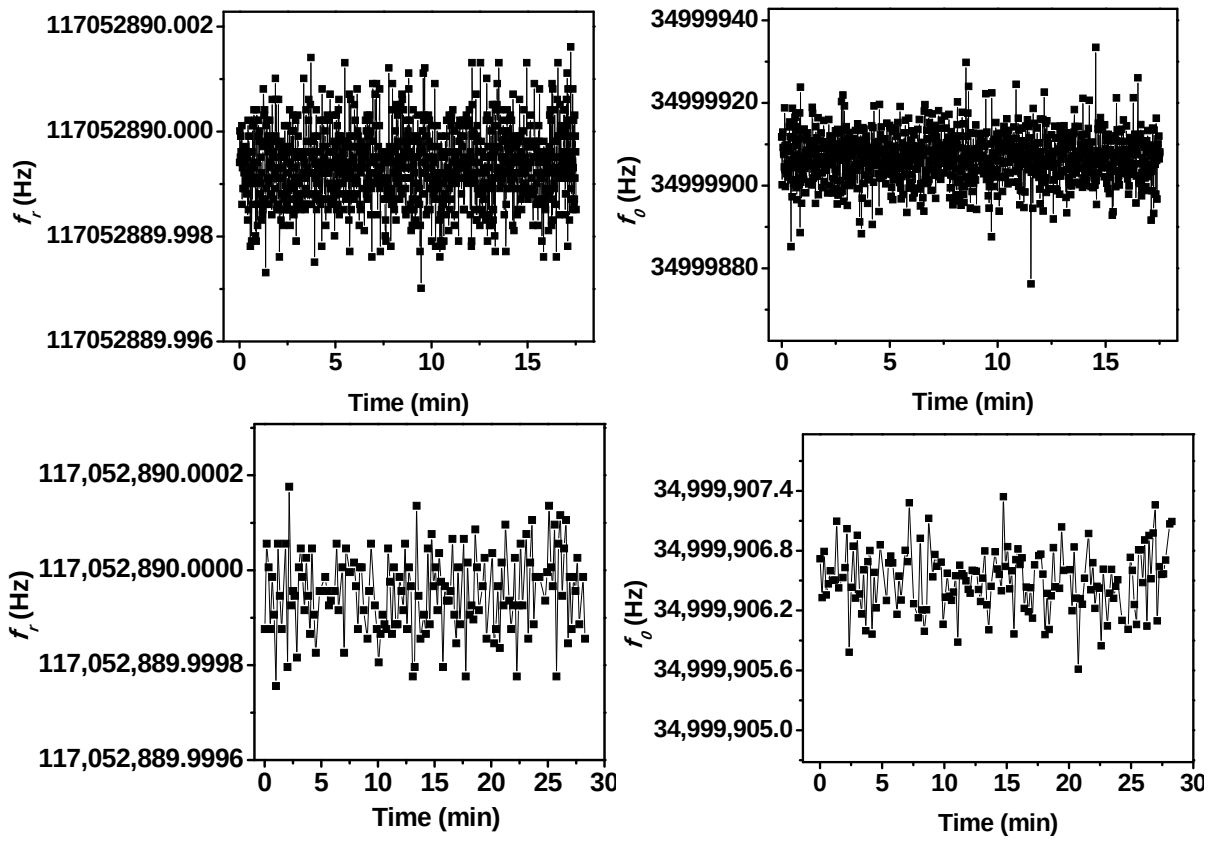

Figure 3.15. Counter frequency measurement of f_r and f_0 with 1-s gate time (upper two graphs) and 10-s gate time (lower two graphs). We have removed some of the occasional large spikes from the graph.

Each of the measurements of f_r and f_0 consists of count data of three different counters that were monitored and recorded in a computer using a program called "peasoup" originally written at NIST, Boulder. We repetitively gate the counter using different gate times of 1 ms, 10 ms, 100 ms, 1000 ms and 10000 ms in each run. The repetition rate data were limited by noise in the counters to approximately $\Delta f/f \approx 5\times10^{-11}$ or 50 mHz at 1-s gate time. We then calculate the Allan deviation to describe the stability of f_r and f_0. Based on these measurements we assign an upper limit of fractional frequency uncertainty for the stabilized Cr:forsterite frequency comb of $\sim 5\times10^{-12}$ at a 1 second gate time. This is the in-loop measurement of the stability of the comb and this measurement does not take into account noise in the GPS system. Reliable measurement of the stability of the comb can be carried by making out-of-loop measurement. However, our out of loop measurement is also limited by the stability of the GPS reference at 2×10^{-11} at 1s-gate time. The out-of-loop measurement of comb stability is discussed in Chapter 7. Figure 3.16 below shows the Allan deviation of the time series measurements of f_r and f_0.

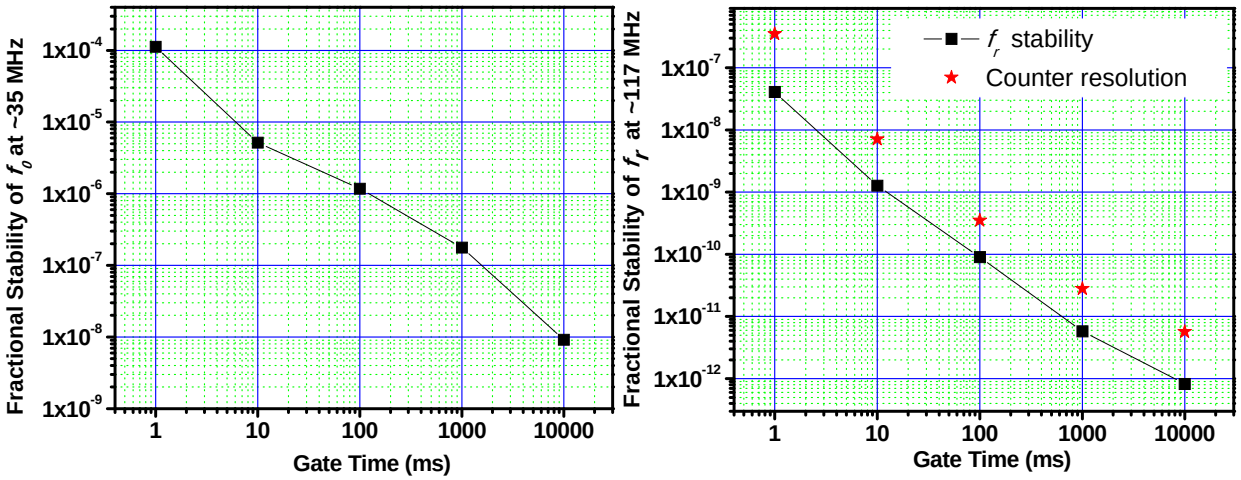

Figure 3.16 Fractional stability of f_0 (upper graph) and f_r (lower graph) for different gate times measured in RF domain.

To the best of my knowledge, this the first stabilized frequency comb using a prism-based Cr:forsterite laser. As discussed already, Cr:forsterite laser is a difficult laser to work with because of several drawbacks of the crystal itself. Moreover, our pump is not strictly single mode and it has lots of high frequency noise as well as significant power fluctuations. We have developed four different servo systems including a prism servo inside the cavity to stabilize the Cr:forsterite laser. These kinds of servo systems, we believe, can be used in many other less stable laser systems as ours. Kim *et al.* at NIST also stabilized the chirped mirror based Cr:forsterite laser and was able to phase stabilize it with the frequency stability of 2.9×10^{-13} at 1-s of averaging time [87]. But their comb is referenced with a maser which has the frequency stability of 2.5×10^{-13} at 1-s; at least 2 order of magnitude better than our GPS reference system which puts the upper limit on the frequency measurement. One subtle difference between two of these laser systems besides the cavity configuration is the width of the f_0 which is much wider in the chirped mirror based Cr:forsterite laser system, ~ 6.7 MHz, despite employing a similar pump system. They attributed the width of the f_0 to the level of intensity noise present on the pump laser but it can also depend on the cavity configuration. We have demonstrated that the dominating linewidth broadening mechanism for f_0 in Cr:forsterite is not the pump noise since the estimated f_0 linewidth should be ~50 kHz as per the noise in the pump system which underestimate the actual f_0 linewidth of 1.5 MHz by a factor of 30. Our result of knife edge insertion inside the cavity also shows the potential to use prism based Cr:forsterite laser with much narrower f_0 width of around 10 kHz. It was however found to be relatively easy to stabilize

f_0 using pump power modulation for comparatively broad f_0 linewidth. We use our stabilized Cr:forsterite laser system to measure the absolute frequency of acetylene lines inside the hollow core optical fiber which will be discussed in later chapters. The next Chapter basically focuses on the spectroscopy inside these hollow core fibers which is the first step toward developing these portable frequency references.

CHAPTER 4 - Saturation spectroscopy of acetylene inside hollow core fibers

This Chapter describes the nonlinear spectroscopy of acetylene in the near infrared spectral region inside a photonic band gap fiber. The near infrared region of the optical spectrum is an area of intensive research due to its relevance to telecommunication and optical metrology. Acetylene provides a large number of reference transitions coincident with the international telecommunication band. Acetylene contains about 50 strong lines between 1510 nm and 1540 nm in the $\nu_1+\nu_3$ ro-vibrational combination band. We have observed the Doppler-free saturated spectrum of several of these lines, inside a variety of fibers. Saturated absorption spectroscopy is performed on acetylene inside photonic bandgap fibers of small (~10 μm) and large (~20 μm) core diameters. The large core fiber offers significant advantages, including a significant reduction in background oscillations which have been attributed by others to surface modes. Furthermore, the linewidth is reduced significantly due to increased interaction time between the molecules and the laser beam. The $\nu_1+\nu_3$ band near 1532 nm is explored, and line widths of 20-40 MHz are observed. Recently, we have used much larger core, kagome structured (~68 μm core) fiber, to perform saturation spectroscopy and observed ~10 MHz linewidth. This is described in the last part of this chapter. The line width and signal strength depend upon various parameters, including fiber diameter, pressure, optical power, and fiber length but is mostly dominated by the mode field diameter of the fiber.

4.1. Introduction

The development of optical frequency standards in the near-infrared spectral region has been motivated in part by the optical telecommunications industry. Acetylene gas offers a series of well-spaced spectral features in the 1.5 μm region, spanning the C band. By pressure-broadening these features to about 1 GHz in width, the National Institute of Standards and Technology (NIST) has created portable standards of moderate uncertainties, between 13 MHz and 130 MHz, that can be built into commercial devices [6, 99]. Meanwhile, sub-Doppler spectroscopy of molecular gases provides high-accuracy infrared optical frequency references. Typically the weak molecular overtone transitions employed at these wavelengths require high powers for

saturation, and therefore to date all high-accuracy references have been based on power build-up cavities [100, 101] , which provide power amplification and long effective interaction lengths but are not readily portable. A series of measurements of lines in the $\nu_1 + \nu_3$ band [101-103] led the Comitté International des Poids et Mesures (CIPM) to adopt a value of the P(16) line in $^{13}C_2H_2$ with an uncertainty of 100 kHz [104]. With the advent of frequency comb technology, groups at the National Institute of Advanced Industrial Science and Technology (AIST) in Japan [105, 106], National Physics Laboratory (NPL) in Great Britain [107], and the National Research Council (NRC) in Canada [108, 109] have measured these lines with greatly increased precision. The CIPM recently reduced the uncertainty of the P(16) transition to 10 kHz, and most recently, 61 lines in the band have been realized with a width of 600 kHz and measured to an uncertainty of 1.4 kHz [110]. There are many advantages to performing saturation spectroscopy independent of a power build-up cavity, as described in Ref. [111], where signals with widths ~1 MHz have been observed inside a 1 m long glass cell.

While the science of frequency metrology has been transformed, optical fiber technology has simultaneously been revolutionized. The advent of hollow, low-loss photonic bandgap (PBG) fiber allows light to be confined at high intensities in a hollow air or gas-filled region with very low loss [19]. These fibers are vastly superior to capillary fibers for small core diameters [20], and have therefore been used in many recent demonstrations of nonlinear light-gas interactions. For example, acetylene has been detected in small quantities inside a PBG fiber employed as a gas sensor [112], and Raman scattering in hydrogen-filled fiber has created very tunable laser light [22]. Furthermore, electromagnetically induced transparency (EIT) in acetylene-filled PBG fibers [113, 114], revealing sub-Doppler transitions when the pump and probe lasers were arranged in a co-propagating laser beams [115]. Lasers have been locked to the side of Doppler-broadened transitions in acetylene-filled fibers, toward the development of portable frequency references [24]. These fibers were sealed by splicing the PBG fibers to solid-core fiber on both ends. Finally, saturated absorption has been observed inside photonic bandgap fibers, but with larger linewidth and reduced signal-to noise [115, 116].

All the previous work in PBG fibers has been based on single laser beam interrogation, or co-propagating pump-probe geometry. To establish frequency references based on gas-filled PBG fiber, a counter-propagating geometry is required, which gives rise to unwanted optical interference. We characterized saturated absorption inside PBG fibers, as a function of gas and

fiber dimensions. We have measured saturated absorption features inside PBG fibers for a variety of pressure and pump power values. The central dip in transmitted power is due to the presence of the pump beam, which burns a Bennett hole in the ground-state population of the acetylene molecules. When the probe and the pump are resonant with the same velocity class of molecules, the probe light is less strongly absorbed. A laser may be locked to this feature and used as a frequency reference which we will discuss in chapters 5 and 6.

4.2. Theoretical background: Doppler free saturated absorption spectroscopy

The technique of Doppler-free saturated absorption spectroscopy was developed by the research group of Arthur L. Schawlow, who was one of the recipients of the 1981 Nobel Prize in physics for this work. Before the development of this technique, Doppler widths of about 500 MHz, caused by the random thermal motion of the atoms being studied, ultimately limited the resolution of optical spectroscopy. Doppler-free saturated absorption spectroscopy is insensitive to this effect. In this technique, there are two counter-propagating laser beams- a saturating beam and a probe beam. The saturating beam identifies a group of molecules in a narrow interval of axial velocities and pumps a sizable portion of the molecules from the lower level to the upper one. It thereby creates hole in the velocity distribution of the lower level. A second laser beam, called a probe beam, is needed to probe this modified velocity distribution of molecules. When both saturating and probe beams are tuned to interact with the same group of molecules, the probe beam will experience a lower amount of absorption or a modified refractive index and therefore a saturated absorption signal will emerge from the Doppler-broadened absorption background. The saturating field and probe beam generally influence each other but we have minimized that effect by working at lower probe power.

The effect of optical pumping on the saturation of population densities can be explained by simple two-level systems in which the two levels are coupled to each other by absorption or emission and by relaxation processes. Such a two-level system is realized by many atomic resonance transitions without hyperfine structure.

Let $E_1$and E_2 be the lower and upper energy levels respectively, with population in each level denoted by N_1 and N_2 respectively. γ_1 and γ_2 are the decay rates for levels 1 and 2.

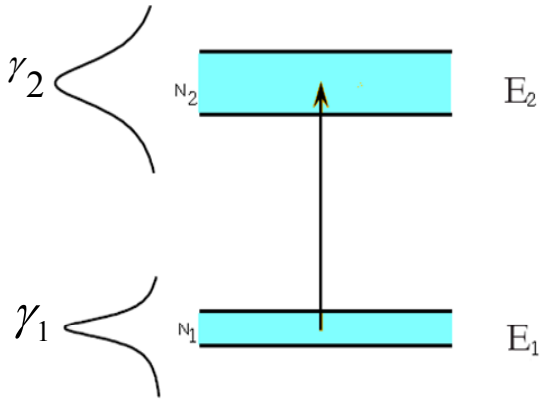

Figure 4.1. Uncertainty in the energy level.

When a monochromatic laser beam $E = E_0 cos(\omega t - kz)$ passes through the sample of molecules, the intensity, I, of the laser beam changes according to Beer's law as,

$$\frac{dI}{dz} = -\alpha I \tag{4.1}$$

where $\alpha = \alpha(\nu)$ is the frequency-dependent absorption coefficient. The absorption coefficient $\alpha(\nu)$ for a transition $|1\rangle \rightarrow |2\rangle$ depends upon the population densities of the lower and upper levels, and on the optical absorption cross-section σ_{12} of each absorbing atom.

To a good approximation, for a single weak beam, $\alpha(\nu)$ does not depend upon position. Therefore, the overall transmission through the fiber cell of length ℓ is given by

$$I = I_0 \exp[-\alpha(\nu) l] \tag{4.2}$$

where $\alpha(\nu) l$ is also called optical depth.

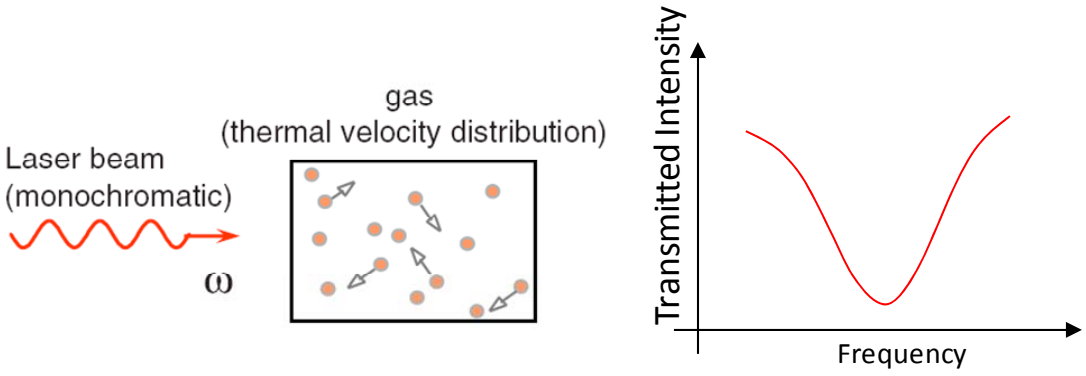

Figure 4.2. Intensity profile due to absorption of radiation.

The exact form of $\alpha(\nu)$ depends upon physical situation. Ideally, it would be Lorentzian with a characteristic linewidth equal to that of the natural linewidth of the transition (Fig.4.2). However, many mechanisms such as Doppler broadening, transit time broadening, power broadening etc. serve to broaden that linewidth. Typically the absorbance $\alpha(\nu)$ for saturation absorption is calculated either in the limit of equal pump and probe power or in the case when the saturation parameter, which we will discuss later, is much smaller than unity; here we seek to make a more general calculation of α that will apply to our system.

The absorption of the incident wave causes changes in the population of the levels involved in the absorbing transition. The rate Eq. for the population densities N_1 and N_2 of the non-degenerate levels $|1\rangle$ and $|2\rangle$ with statistical weight factors $g_1 = g_2 = 1$ can be written as,

$$\frac{dN_1}{dt} = B_{12}\rho_\nu(N_2 - N_1) - R_1N_1 + R_{21}N_2 + D_1 \tag{4.3}$$

$$\frac{dN_2}{dt} = B_{12}\rho_\nu(N_1 - N_2) - \mathrm{R_2N_2} + R_{12}N_1 + D_2 \tag{4.4}$$

where ρ_ν is the spectral energy density of the radiation field, B_{12} and B_{21} are Einstein's coefficients, R_1N_1 is relaxation of N_1 due to collision of $|1\rangle$ with anything that depopulates state 1 due to collision with velocity v at z, $\mathrm{R_2N_2}$ are the relaxation of N_2 due to collision of $|2\rangle$ with anything that depopulates state 2. R_{21} arises due to inelastic collisions that knock a molecule in $|2\rangle$ to $|1\rangle$. $R_{12}N_1$ and $R_{21}N_2$ are spontaneous emission that depopulates level $|1\rangle$ and $|2\rangle$, and D_1 and D_2 take care of diffusion rate of molecules in both the levels.

When a laser beam $E = E_0 cos(\omega t - kz)$ with the mean intensity, $I = \frac{1}{2}C\varepsilon_0 E_0^2$ passes through the sample of molecules, which absorb on the transition $E_2 - E_1 = \hbar\omega_L$, the power dP absorbed in the volume $dV = Adz$ is given by $dP = AI\sigma_{12}\Delta N dz$. Therefore we can write,

Energy at ω_L absorbed in volume $Adz = \int \Delta N(v) Adz\sigma(\omega_L, z)\frac{I(\omega_L, z)}{\hbar\omega_L}\hbar\omega_L d^3v$

where v is the velocity of the molecule under consideration in the direction of propagation of the laser beam, $\int \Delta N(v) A dz d^3v$ represents the number of targets, $\sigma(\omega_L, z)\frac{I(\omega_L, z)}{\hbar\omega_L}$ is the rate of transition per target and $\hbar\omega_L$ represents energy per transition.

$$\therefore \Delta I(\omega_L, z) = -\frac{\text{Energy absorbed in volume } Adz}{Area(A)}$$

$$\Rightarrow \frac{\Delta I(\omega_L, z)}{\Delta z} = -\Delta N(v, z)\sigma(\omega_L, v) I(\omega_L, z) d^3v$$

$$\Rightarrow \frac{1}{\Delta z}\frac{\Delta I(\omega_L, z)}{I(\omega_L, z)} = -\Delta N(v, z)\sigma(\omega_L, v) d^3v$$

$$\therefore \frac{d \log I(\omega_L, z)}{dz} = -\Delta N(v, z)\sigma(\omega_L, v) d^3v$$

If ΔN were independent of $I(\omega_L, z)$, then the integral gives $\alpha(\omega_L, z)$. Typically $\Delta N(v,z)$ is also independent of z, so,

$$\alpha(\omega_L, z) = \alpha(\omega_L) = -\int \Delta N(v, z)\sigma(\omega_L, v) d^3V \tag{4.5}$$

$$\therefore \frac{d \log I(\omega_L, z)}{dx} = -\int \Delta N(v, z)\sigma(\omega_L, v) d^3V \tag{4.6}$$

Now let us take the case when both pump and probe are present at the same time,

$$\frac{dN_1(v, z)}{dt} = \gamma_{sp} N_2(v, z) - N_1(v, z)\left[\sigma(\omega_L, v)\frac{I(\omega_L)}{\hbar\omega_L} + \sigma(\omega_L', -v)\frac{I(\omega_L')}{\hbar\omega_L'}\right]$$
$$+ N_2(v, z)\left[\sigma(\omega_L, v)\frac{I(\omega_L)}{\hbar\omega_L} + \sigma(\omega_L', -v)\frac{I(\omega_L')}{\hbar\omega_L'}\right] - R_1 N_1(v, z) + R_{21} N_2(v, z) + D_1$$

First bracketed expression in above equation represents depopulation of N_1 level with pump and probe where they have different frequencies ω_L and ω_L' respectively. Similarly, the second bracketed term is due to an increase in the population of level $|2\rangle$ due to the presence of both pump and probe.

$$\therefore \frac{dN_1(v, z)}{dt} = -(N_1 - N_2)\left[\sigma(\omega_L, v)\frac{I(\omega_L)}{\hbar\omega_L} + \sigma(\omega_L', -v)\frac{I(\omega_L')}{\hbar\omega_L'}\right] \tag{4.7}$$
$$+ \gamma_{sp} N_2(v, z) - R_1 N_1(v, z) + R_{21} N_2(v, z) + D_1$$

Similarly, $$\frac{dN_2(v,z)}{dt} = (N_1 - N_2)\left[\sigma(\omega_L, v)\frac{I(\omega_L)}{\hbar\omega_L} + \sigma(\omega_L^{'}, -v)\frac{I(\omega_L^{'})}{\hbar\omega_L^{'}}\right] - \gamma_{sp}N_2(v,z) - R_2N_2(v,z) + R_{12}N_1(v,z) + D_2 \quad (4.8)$$

Now, at steady state, $\frac{dN_1(v,z)}{dt} = 0$, so,

$$(N_1 - N_2)\left[\sigma(\omega_L, v)\frac{I(\omega_L)}{\hbar\omega_L} + \sigma(\omega_L^{'}, -v)\frac{I(\omega_L^{'})}{\hbar\omega_L^{'}}\right] - \gamma_{sp}N_2(v,z) + R_1N_1(v,z) - R_{21}N_2(v,z) - D_1 = 0$$

But $N_1 = N - N_2$, and $D_2 \approx R_1N_1 - D_1$, we can get,

$$\Delta N = N_1 - N_2 = \frac{N(\gamma_{sp} + R_{21}) - 2D_2}{2\left[\sigma(\omega_L, v)\frac{I(\omega_L)}{\hbar\omega_L} + \sigma(\omega_L^{'}, -v)\frac{I(\omega_L^{'})}{\hbar\omega_L^{'}}\right] + \gamma_{sp} + R_{21}} \quad (4.9)$$

Where we have assumed that R_1N_1 includes the collisions which do not change velocity.

When laser is turned off, all the population is in $|1\rangle$. The unsaturated population difference ΔN^0 can be written as

$$\Delta N^0 = N - \frac{2D_2}{\gamma_{sp} + R_{21}} \quad (4.10)$$

But, when beam is on, we can rewrite expression 4.9 as,

$$\Delta N = \frac{N - \frac{2D_2}{\gamma_{sp} + R_{21}}}{1 + \frac{2\left[\sigma(\omega_L, v)\frac{I(\omega_L)}{\hbar\omega_L} + \sigma(\omega_L^{'}, -v)\frac{I(\omega_L^{'})}{\hbar\omega_L^{'}}\right]}{\gamma_{sp} + R_{21}}} = \frac{\Delta N^0}{1 + S} \quad (4.11)$$

where the saturation parameter,

$$S = S(v,z) = \frac{2\left[\sigma(\omega_L, v)\frac{I(\omega_L)}{\hbar\omega_L} + \sigma(\omega_L^{'}, -v)\frac{I(\omega_L^{'})}{\hbar\omega_L^{'}}\right]}{\gamma_{sp} + R_{21}} \quad (4.12)$$

is the saturation parameter which includes a contribution due to both pump and probe. If we consider only pump beam propagation, then the saturation parameter can be written as

$$S = \frac{2\sigma(\omega_L^{'}, -v) I(\omega_L^{'})}{\hbar\omega_L^{'}(\gamma_{sp} + R_{21})} \tag{4.13}$$

It gives the ratio of the induced transition probability to the mean relaxation probability. The intensity $I=I_S$ at which the saturation parameter S becomes S=1 is called the saturation intensity, where,

$$I_S = \frac{\hbar\omega_L^{'}(\gamma_{sp} + R_{21})}{2\sigma} \tag{4.14}$$

It is obvious from Eq. 4.11 that, for S=1, the population difference ΔN decreases to one half of its unsaturated value ΔN^0. Saturation also decreases the absorption coefficient $\alpha(\omega)$ by the factor (1+*S*) as shown in Fig. 4.3.

$$\alpha_s(\omega) = \frac{\alpha(\omega)}{1+S}$$

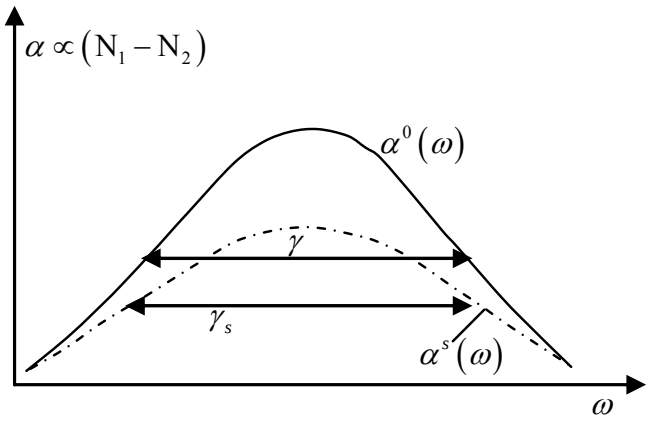

Figure 4.3. Saturation absorption profile.

As mentioned before, collisions usually do change the velocity so this expressions and original expression for dN_1/dt is approximate. Now, Eq. 4.6 reduces to,

$$\therefore \frac{d \log I_A(\omega_L, z)}{dz} = -\int \frac{\Delta N^0(v)}{1+S(v,z)} \sigma_A(\omega_L, v) d^3v \text{ and} \tag{4.15}$$

$$\therefore \frac{d \log I_B(\omega_L, z)}{dz} = -\int \frac{\Delta N^0(v)}{1+S(v,z)} \sigma_B(\omega_L^{'}, -v) d^3v \tag{4.16}$$

Where, $\sigma_A(\omega_L, v)$ and $\sigma_B(\omega_L', -v)$ are absorption cross-section of pump and probe having intensity of I_A and I_B respectively,

Let us suppose that probe I_B is weak as compare to pump intensity I_A; then we can ignore the term with I_B in expression 4.12 for ΔN. Also, ignore $\frac{D_2}{\gamma_{sp} + R_{21}} \ll N$, so eq. 4.12 can be written as,

$$S = S(v, z) = \frac{2\sigma_A(\omega_L, v)\frac{I_A(\omega_L)}{\hbar\omega_L}}{\gamma_{sp} + R_{21}} \tag{4.17}$$

Equation 4.15 can be written as,

$$\therefore \frac{d \log I_A(\omega_L, z)}{dz} = -\int \frac{\Delta N^0(v)}{1 + \frac{2\sigma_A(\omega_L, v)\frac{I_A(\omega_L)}{\hbar\omega_L}}{\gamma_{sp} + R_{21}}} \sigma_A(\omega_L, v) d^3V \tag{4.18}$$

In two-level system, the absorption cross-section of a molecule in level E_1 that moves with velocity v_z has a Lorentzian profile with natural line width γ given by,

$$\sigma_A(\omega_L, v) = \sigma_0 \frac{(\gamma/2)^2}{(\omega_L - \omega_0 - \frac{\omega_L}{c} v_z)^2 + \left(\frac{\gamma}{2}\right)^2} \tag{4.19}$$

where $\sigma_0 = \sigma(\omega = \omega_0 + \frac{\omega_L}{c} v_z)$ is the maximum absorption cross-section at the line center of the molecular transition.

$$\therefore \frac{d \log I_A(\omega_L, z)}{dz} = -\int \frac{\sigma_0 (\gamma/2)^2}{(\omega_L - \omega_0 - \frac{\omega_L}{c} v_z)^2 + \left(\frac{\gamma}{2}\right)^2} \frac{N(v)\sigma_A(\omega_L, v)}{1 + \frac{2\sigma_A\left(\frac{\gamma}{2}\right)^2 I_A(\omega_L, z)}{(\omega_L - \omega_0 - \frac{\omega_L}{c} v_z)^2 \hbar\omega_L(\gamma_{sp} + R_{21})}} d^3v$$

$$= -\int \frac{\sigma_0 (\gamma/2)^2 N(v)}{(\omega_L - \omega_0 - \frac{\omega_L}{c} v_z)^2 + \left(\frac{\gamma}{2}\right)^2 + \frac{2\sigma_0\left(\frac{\gamma}{2}\right)^2 I_A(\omega_L, z)}{\hbar\omega_L(\gamma_{sp} + R_{21})}} d^3v \tag{4.20}$$

At thermal equilibrium, all the molecules of a gas follow a Maxwell velocity distribution. Therefore the number of molecules with velocity v_z in the direction of the observed light is given by,

$$n(\mathrm{v}_z)d\mathrm{v}_z = \frac{N}{v_{th}\sqrt{\pi}}\exp\frac{-\mathrm{v}_z^2}{v_{th}^2} \tag{4.21}$$

where N is total number of molecules.

$$\therefore \frac{d\log I_A(\omega_L,z)}{dz} = -\int_{-\infty}^{\infty} \frac{dv_z N\exp\frac{-\mathrm{v}_z^2}{v_{th}^2}\sigma_0(\gamma/2)^2}{\sqrt{\pi}\,v_{th}\left\{(\omega_L-\omega_0-\frac{\omega_L}{c}v_z)^2+\left(\frac{\gamma}{2}\right)^2+\frac{2\sigma_0\left(\frac{\gamma}{2}\right)^2 I_A(\omega_L,z)}{\hbar\omega_L(\gamma_{sp}+R_{21})}\right\}} \tag{4.22}$$

If Lorentzian is sharper than Gaussian, then, $\sqrt{\left(\frac{\gamma}{2}\right)^2+\frac{2\sigma_0\left(\frac{\gamma}{2}\right)^2 I_A(\omega_L,z)}{\hbar\omega_L(\gamma_{sp}+R_{21})}}\Big/\left(\frac{\omega_L}{c}\right) \ll \frac{1}{v_{th}}$

$$\therefore \frac{d\log I_A(\omega_L,z)}{dz} = -N\exp\left\{-\left(\frac{\omega_L-\omega_0}{\omega_L/c}\right)^2\right\}\sigma_0(\gamma/2)^2 \int_{-\infty}^{\infty} \frac{\omega_L/c\,dv_z}{\sqrt{\pi}\,v_{th}\left\{(\omega_L-\omega_0-\frac{\omega_L}{c}v_z)^2+\left(\frac{\gamma}{2}\right)^2+\frac{2\sigma_0\left(\frac{\gamma}{2}\right)^2 I_A(\omega_L,z)}{\hbar\omega_L(\gamma_{sp}+R_{21})}\right\}\frac{\omega_L}{c}} \tag{4.23}$$

The integral is in the form,

$$\int_{-\infty}^{\infty}\frac{dx}{x^2+(a+bI_A)\omega_L/c} = \frac{\pi}{(a+bI_A)\omega_L/c} \tag{4.24}$$

So above equation reduces to,

$$\therefore \frac{d\log I_A(\omega_L,z)}{dz} = \frac{-N\exp\left\{-\left(\frac{\omega_L-\omega_0}{\omega_L/c}\right)^2\right\}\sigma_0(\gamma/2)^2\sqrt{\pi}}{v_{th}\sqrt{\left(\frac{\gamma}{2}\right)^2+\frac{2\sigma_0\left(\frac{\gamma}{2}\right)^2 I_A(\omega_L,z)}{\hbar\omega_L(\gamma_{sp}+R_{21})}}/\frac{\omega_L}{c}} \tag{4.25}$$

$$= \frac{-N\exp\left\{-\left(\frac{\omega_L-\omega_0}{\omega_L/c}\right)^2\right\}\sigma_0(\gamma/2)^2\sqrt{\pi}}{\sqrt{1+\frac{I_A}{I_S}}} \tag{4.26}$$

Where $I_S = \frac{\hbar\omega_L(\gamma_{sp}+R_{21})}{2\sigma_0\left(\frac{\gamma}{2}\right)^2}$ is saturation intensity as mentioned in eq 4.14.

Equation 4.26 is in the form, $\frac{d\log I_A(\omega_L,z)}{dz} = -\frac{C_1}{\sqrt{1+C_2 I_A}}$ which can be solved analytically,

$\int \frac{\sqrt{1+C_2 I_A}}{I_A} dI_A = -C_1 z$ where, $C_1 = -N\exp\left\{-\left(\frac{\omega_L-\omega_0}{\omega_L/c}\right)^2\right\}\sigma_0(\gamma/2)^2\sqrt{\pi}$ which gives,

$$2\sqrt{1+C_2 I_A} - 2\tan^{-1} h\sqrt{1+C_2 I_A} = -C_1 z \tag{4.27}$$

$\Rightarrow I_A(\omega_L,z) = f(z)$ This expression gives pump power at every point along the propagation direction.

Now, let us consider probe beam in presence of pump,

$$\alpha_B(\omega_L^{'}, I_A(z) = \int \frac{N(v)}{1+S(v,I_A)}\sigma_B(\omega_L^{'},-v)d^3V$$

Similar to expression (4.22), we can write,

$$\alpha_B(\omega_L^{'}, I_A(z) = -\int_{-\infty}^{\infty} \frac{dv_z N \exp\frac{-v_z^2}{v_{th}^2}\sigma_0(\gamma/2)^2 / \left\{(\omega_L^{'} - \omega_0 - \frac{\omega_L^{'}}{c}v)^2 + \left(\frac{\gamma}{2}\right)\right\}^2}{\sqrt{\pi}\, v_{th}\left\{1 + \frac{2\sigma_0\left(\frac{\gamma}{2}\right)^2 I_A(\omega_L, z)}{\hbar\omega_L(\gamma_{sp} + R_{21})\left\{(\omega_L - \omega_0 - \frac{\omega_L}{c}v_z)^2 + \left(\frac{\gamma}{2}\right)^2\right\}}\right\}} \tag{4.28}$$

$$\alpha_B(\omega_L^{'}, I_A(z) = -\frac{N\sigma_0(\gamma/2)^2}{\sqrt{\pi}\, v_{th}}\exp\frac{-v^2}{v_{th}^2}$$

$$\int_{-\infty}^{\infty} \frac{\left\{(\omega_L - \omega_0 - \frac{\omega_L}{c}v)^2 + \left(\frac{\gamma}{2}\right)^2\right\}dv}{\sqrt{\pi}\, v_{th}\left\{(\omega_L^{'} - \omega_0 - \frac{\omega_L^{'}}{c}v)^2 + \left(\frac{\gamma}{2}\right)^2\right\}\left\{(\omega_L - \omega_0 - \frac{\omega_L}{c}v)^2 + \left(\frac{\gamma}{2}\right)^2 + \frac{I_A}{I_S}\right\}} \tag{4.29}$$

$$\text{Let } \left(\frac{\gamma_s}{2}\right)^2 = \left(\frac{\gamma}{2}\right)^2 + \frac{I_A}{I_S} \tag{4.30}$$

$$\alpha_B(\omega_L^{'}, I_A(z)) = -\frac{N\sigma_0(\gamma/2)^2}{\sqrt{\pi}\, v_{th}}\exp\frac{-v^2}{v_{th}^2}$$

$$\int_{-\infty}^{\infty} \frac{\left\{(\omega_L - \omega_0 - \frac{\omega_L}{c}v)^2 + \left(\frac{\gamma}{2}\right)^2\right\}dv}{\sqrt{\pi}\, v_{th}\left\{(\omega_L^{'} - \omega_0 - \frac{\omega_L^{'}}{c}v)^2 + \left(\frac{\gamma}{2}\right)^2\right\}\left\{(\omega_L - \omega_0 - \frac{\omega_L}{c}v)^2 + \left(\frac{\gamma_s}{2}\right)^2\right\}} \tag{4.31}$$

The integration gives the general expression of absorption coefficient of the probe in the case when both the pump and probe are simultaneously tuned over the velocity distribution.

If the frequency of the pump and probe are same i.e. $\omega_L = \omega_L^{'} = \omega$, we can easily solve this using contour integral since there are four poles as seen from the denominator of the above integral. We can write 4.31 as

$$\alpha_B(\omega, I_A(z)) = -\frac{N\sigma_0(\gamma/2)^2}{\sqrt{\pi}\, v_{th}} \exp\left\{-\left(\frac{\omega-\omega_0}{\omega} - \frac{c}{v_{th}}\right)^2\right\}$$

$$\frac{c}{\omega^2}\int_{-\infty}^{\infty} \frac{\left\{\left(\frac{\omega-\omega_0}{\omega} - \frac{v}{c}\right)^2 + \left(\frac{\gamma}{2\omega}\right)^2\right\} d\left(\frac{v}{c}\right)}{\sqrt{\pi}\, v_{th}\left\{\left(\frac{\omega-\omega_0}{\omega} - \frac{v}{c}\right)^2 + \left(\frac{\gamma}{2\omega}\right)^2\right\}\left\{\left(\frac{\omega-\omega_0}{\omega} - \frac{v}{c}\right)^2 + \left(\frac{\gamma_s}{2}\right)^2\right\}} \tag{4.32}$$

$$\text{Integral, I} = \frac{2\pi i[-i\omega\left\{16(\omega-\omega_0)^2\gamma_s + \gamma(\gamma+\gamma_s)^2\right\}]}{\gamma\gamma_s\left\{16(\omega-\omega_0)^2 + (\gamma+\gamma_s)^2\right\}}$$

$$\Rightarrow \alpha_s(\omega) = \alpha_0(\omega)\left[\frac{\gamma}{\gamma_s} - \frac{(\omega-\omega_0)^2\left(\frac{\gamma-\gamma_s}{\gamma_s}\right)}{(\omega-\omega_0)^2 + \left(\frac{\Gamma_S^*}{2}\right)^2}\right] \tag{4.33}$$

$$\text{Where, } \alpha_0(\omega) = -\frac{\sqrt{\pi}N\sigma_0\gamma c}{2\omega v_{th}} \exp\left\{-\left(\frac{\omega-\omega_0}{\omega} - \frac{c}{v_{th}}\right)^2\right\}$$

Equation 4.33 is the absorption coefficient in the case when both the pump and probe are simultaneously tuned over the velocity distribution with the same frequency.

We can write $\left(\frac{\gamma_s}{2}\right)^2 = \left(\frac{\gamma}{2}\right)^2 + \frac{I_A}{I_S}$ as, $\left(\frac{\gamma_s}{2}\right)^2 = \left(\frac{\gamma}{2}\right)^2 + \frac{I_A 2\sigma_0\left(\frac{\gamma}{2}\right)^2}{\hbar\omega_L(\gamma_{sp}+R_{21})}$

$$\therefore \gamma_s{}^2 = \gamma^2 + \frac{2\sigma_0 I_A}{\hbar\omega_L(\gamma_{sp}+R_{21})}\gamma^2 \quad \Rightarrow \gamma_s = \gamma\sqrt{1+S} \tag{4.34}$$

$$\text{Similarly, we can simplify, } \Gamma_S^* = \frac{\gamma+\gamma_s}{2} = \frac{\gamma}{2}\left[1+\sqrt{1+S}\right] \tag{4.35}$$

The FWHM of Γ_S^* represents the sum of the width of the saturated dip due to the strong pump beam and the unsaturated homogeneous absorption width γ of the weak probe beam when both the pump and probe are simultaneously tuned; the detected dip is called a Lamb dip.

We can rewrite Eq. 4.33 in the form

$$\alpha_S(\omega) = \alpha^0(\omega)\left[1 - \frac{S_0}{2(1+S_0)}\frac{(\gamma+\gamma_S)}{2\gamma_S}\frac{(\gamma_S/2)^2}{(\omega-\omega_0)^2+(\Gamma_S^*/2)^2}\right] \tag{4.36}$$

If the intensity of the probe beam is very small as compared to the pump beam, i.e. for S<<1, $\gamma \approx \gamma_S$, we will get

$$\alpha_S(\omega) = \alpha^0(\omega)\left[1 - \frac{S_0}{2}\frac{(\gamma_S/2)^2}{(\omega-\omega_0)^2+(\Gamma_S^*/2)^2}\right] \tag{4.37}$$

This equation indicates that our experimental line profile with a narrow feature on top of a Doppler profile has the form of a Gaussian Profile times (1-Lorentzian Profile) as $\alpha^0(\omega)$ has Gaussian profile. If we subtract $\alpha^0(\omega)$ from $\alpha_S(\omega)$, we will get the line shape for a narrow feature which would be a narrow Lorentzian times a broad Gaussian.

Considering the form of the equation above, we have fitted our line shape with the similar kind of function in Origin software. Our exact fitting expression in the Origin software is,

$$Y = Y_0 + A_g \exp\left[\frac{-2(X-X_{cg})}{\omega_g}\right]^2\left[1 - A_l\frac{\omega_l^2}{4(X-X_{cl})^2+\omega_l^2}\right] \tag{4.38}$$

where A_g is the amplitude of the Gaussian Profile, Ag times Al gives the amplitude of the narrow feature on top of the Gaussian profile, X_{cg} and X_{cl} are the peak values of the two peaks, and ω_g and ω_l are the widths of the profiles.

4.3. Experimental setup

The experimental setup used to realize these saturated absorption spectra is shown in Fig. 4.4. Two PBG fibers from Crystal Fibre A/S with central wavelengths of 1.55 μm were used. The "20 μm fiber" has 19 missing cells, a core diameter of ~20 μm, and 0.78 m length. The "10 μm fiber" has 7 missing cells, a core diameter of ~10 μm, and 0.90 m length. As shown, both ends of the PBG fiber are fed into the vacuum chambers (VC) via either Torr-seal® feed-throughs or compression fittings. A diode laser (ECDL) emits ~5 mW, 10% of which is amplified by a fiber amplifier (EDFA) to up to 500 mW. 70% of this power becomes the pump beam, and is coupled into the evacuated PBG fiber after passing an isolator (Iso.), a polarization

controller (PC), and a polarizing beam splitter (PBS). The probe beam originates at the EDFA, passes through a double-passed acousto-optic modulator (AOM), an isolator and a PC, and then counter-propagates the pump beam through the PBG fiber. The polarization of the pump and probe beams are intended to remain orthogonal inside the PBG fiber, but polarization rotation inside the fiber must be corrected using half-wave and quarter-wave retarders. Thus the probe beam exiting the fiber can be separated from the pump beam path at the PBS, and the transmitted probe beam power is detected by a photodetector (PD). The AOM and waveplates are essential for minimizing the noise due to interference between the pump laser light reflected from the end of the fiber and the probe beam.

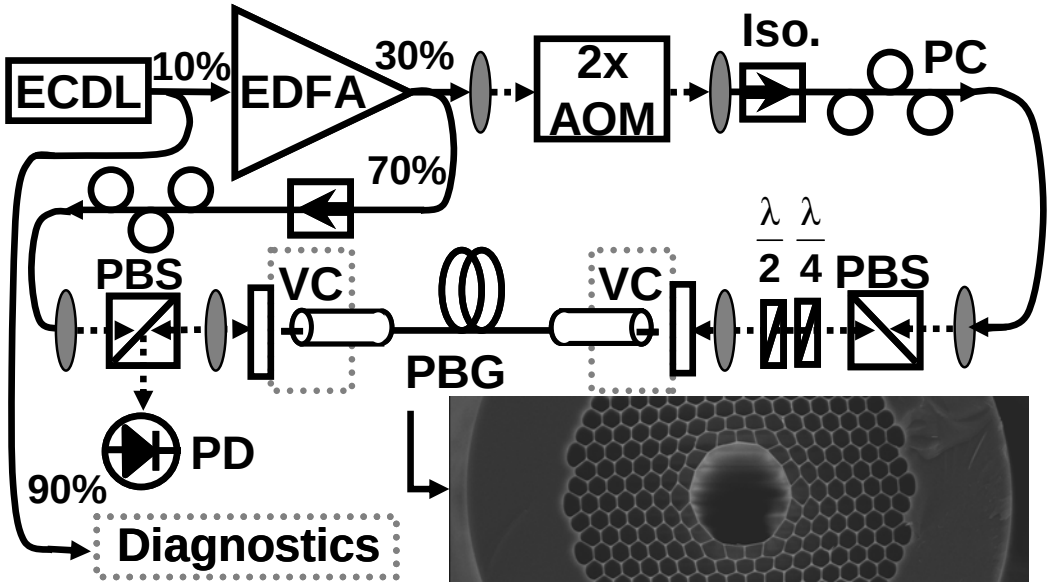

Figure 4.4. Schematic of experimental setup. Solid lines indicate optical fiber, and dashed lines indicate free-space optical beams. Aspheric lenses are shown as shaded ovals, the vacuum chambers (VC), indicated schematically, have wedge windows. The PBG image, courtesy of Crystal Fibre A/S, depicts the 20 μm fiber.

A Michelson interferometer is used to calibrate the horizontal axis of the oscilloscope in optical frequency units. The laser beam is divided by a beam splitter and two beams are recombined at the beam splitter and detected by a photodetector after the beams have traveled distances of $2L_1$ and $2L_2$ (as shown in Fig. 4.5). After returning to the beam splitter, the two

beams will have a phase difference due to their path differences. As the laser frequency is scanned, this phase difference will change, causing a series of maxima and minima.

The frequency spacing of the resolution maxima is given by,

$$\Delta\upsilon = \frac{c}{2(L_1 - L_2)}$$

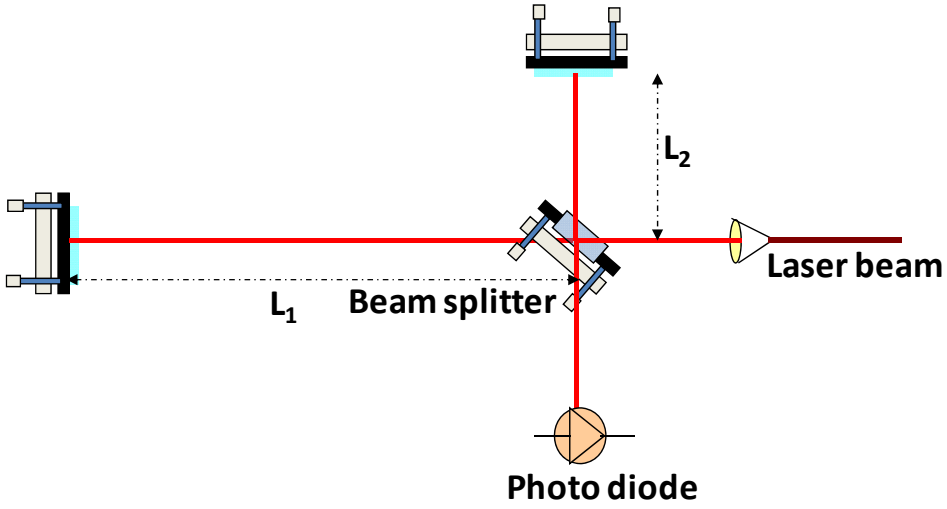

Figure 4.5. Michelson Interferometer.

We can also use the fiber based device such as beam splitter to create a cavity which gives similar kinds of fringes but slightly lower contrast as compare to a Michelson interferometer. The spacing of the fringes or free spectral range, FSR, is governed by the length of the closed loop (Fig 4.6).

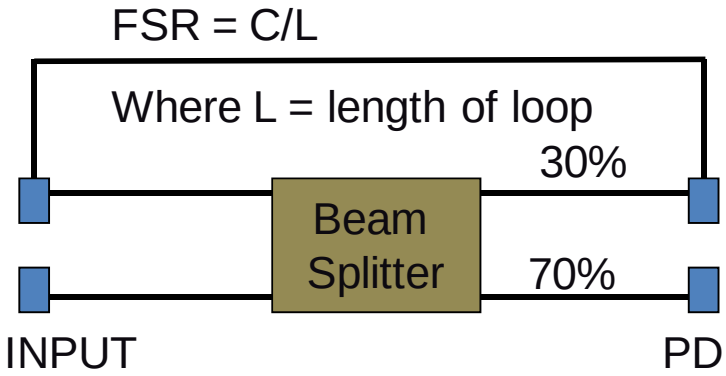

Figure 4.6. Fiber based interferometer

Now, we focus the pump and probe beams into the photonic band gap fiber placed inside the vacuum chamber. The vacuum chamber consists of two separate parts, connected to each other only through the photonic band gap hollow core fiber (PBG Fiber). A long PBG fiber is kept inside two hollow metal tubes. Two extreme ends of the stripped and nicely cleaved small portion of fiber are just outside the metal tube as shown in Fig. 4.7.

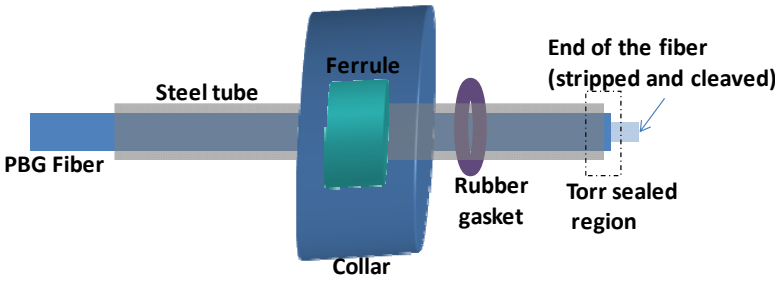

Figure 4.7. Compression fitting for fiber adapter. Torr seal is used to create a vacuum seal between the fiber and hollow metal tube.

An epoxy such as "Torr Seal" is used to create a vacuum seal between the fiber and the hollow metal tube. The metal tube is in turn sealed to two separated vacuum chambers by compression fittings. Gas is then introduced into both chambers, one on each end of the already evacuated chambers so that an equilibrium state of pressure inside the fiber is reached quickly.

There is some drawback of using epoxy as a sealant. Since the fiber is glued to the steel tube, we need to cut the steel tube along with the fiber to re-cleave or change the fiber in the case when fiber degrades in transmission over time or we want to use different fiber. Therefore we now use a slightly different compression fitting technique that creates a seal using an O-ring directly around the fiber as shown in Fig. 4.8.

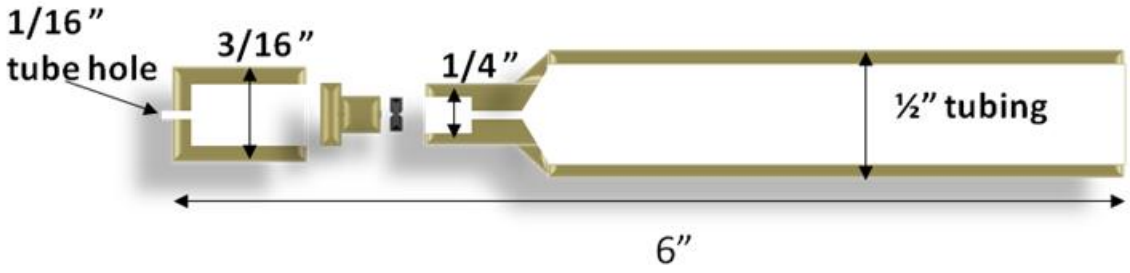

Figure 4.8. Compression fitting for fiber adapter without the use of "Torr seal".

4.4. Data analysis

The theory of saturated absorption spectroscopy is well-known in vapor cells [117]. It has been also discussed in the theory section of this Chapter. In our pump-probe setup, we shift the frequency of the probe by a fixed amount different from the pump frequency using an AOM. The propagation of a laser beam with power P_i along the fiber in direction z can be described by $dP_i = - P_i(z)\,\alpha_i(\nu,z)\,dz$, with $i=(u,r)$ for the case of pump and probe beams, respectively. The pump power is absorbed according to $\alpha_u(\nu,z) = \alpha_D(\nu)/\sqrt{1+S(z)}$, where $\alpha_D(\nu) = \alpha_0 \exp[-(\nu-\nu_0)^2/(0.36\ \nu_D^2)]$ is the Doppler-broadened absorption profile, α_0 is the maximum absorption coefficient on resonance, ν is the laser frequency, ν_0 is the unshifted resonance frequency of the molecules, and ν_D is the Doppler width [117]. The resonant saturation parameter $S_0(z) = P_u(z)/P_s$, where the saturation power, P_s, is the power required at frequency ν_0 to pump ¼ of the ground-state molecules into the excited state.

When the probe beam counter-propagates the pump, with input power $P_r(z=l) = P_{r0}$, the absorption coefficient of the probe beam in terms of S_0 and transition width γ becomes

$$\alpha_r(\nu,z) = \alpha_D(\nu)\left[1 - \frac{S_0(z)}{4}\frac{1+\sqrt{1+S_0(z)}}{\sqrt{1+S_0(z)}}\frac{(\gamma/2)^2}{(\nu-\nu_0)^2+\left(\Gamma_S^*(z)/2\right)^2}\right] \tag{4.39}$$

where $\Gamma_S^*(z) = \gamma\left(1+\sqrt{1+S_0(z)}\right)/2$, as derived in section 4.2. To analyze the data such as that shown in Fig. 4.9, an effective alpha is calculated, $\alpha_e(\nu) = \ln\left[P_r(\nu, z=0)/P_{r0}(\nu, z=l)\right]$ and fit to

$$\alpha_e = A_g \exp\left\{-\left(\frac{2(\nu-\nu_0)}{\nu_D}\right)^2\right\}\left\{1 - \frac{A_l(w/2)^2}{\Delta\nu^2+(w/2)^2}\right\}, \tag{4.40}$$

where $\Delta\nu = \nu - \nu_{AOM} - \nu_0$ includes the shift in the signal due to the AOM. The 10 μm fiber data were fit with additional terms to account for slope and sinusoidal modulation of the background. The width of the saturation feature varies significantly between the 10 μm and 20 μm fibers. At comparable pressures, w is consistently greater in the 10 μm fiber over a range of powers, as shown in Fig. 4.9.

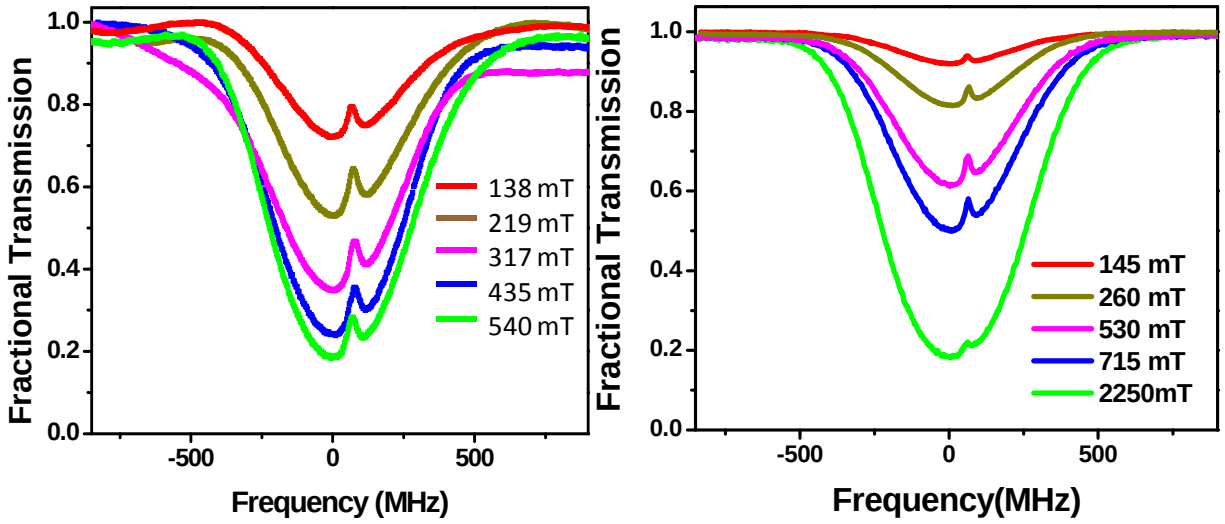

Figure 4.9. Saturated absorption spectra of the P (11) feature as a function of 5 different pressures for the 10 µm and 20 µm fiber. Each curve is normalized to unit intensity at resonance. The zero point in the frequency scale is adjusted so that the origin of the frequency is at the line of symmetry of the Doppler-broadened curve.

We can see from Fig 4.9 that large-core PBG fiber not only gives narrower transitions but it also has much cleaner signals than those observed in smaller PBG fibers. This larger core fiber happens to have fewer surface modes than smaller core fibers which give rise to noises at the back ground of the absorption signal due to surface mode beating. This is consistent with the predictions and observations of West *et al.*[118]. Fig. 4.10 below is the frequency scan of the $\alpha_S(\nu)$, calculated from measurements shown in Fig. 4.9, of P (11) transition line shapes and an overlaid theoretical fit based on the broadening formalism explained in Eq. 4.39. The fit result also produces information such as the amplitude of the Gaussian profile, the amplitude of the small peak on top of the Gaussian, and the width of both.

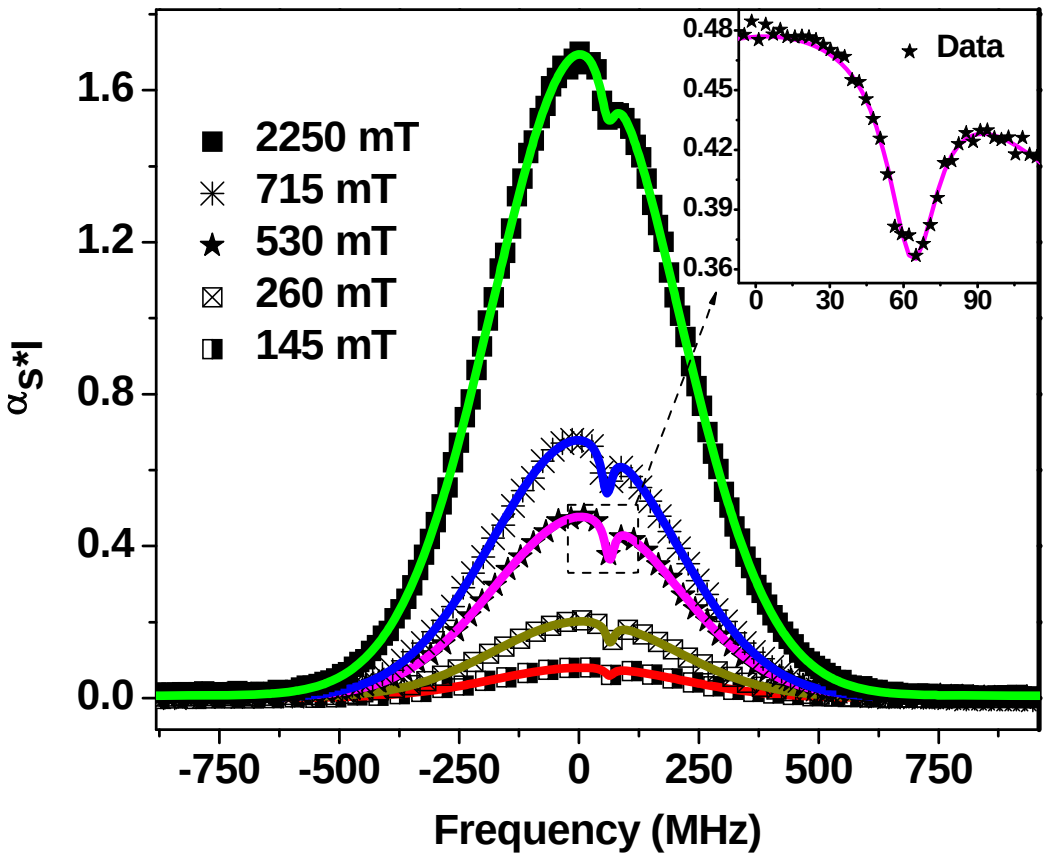

Figure 4.10. Fractional transmission vs. Δν, for the P(11) transition at 1531.6 nm with a pump power of 29 mW incident on the fiber and a counter-propagating probe power of ~1 mW. The $^{12}C_2H_2$ pressure, from top to bottom, was 0.15, 0.26, 0.53, 0.72, and 2.25 torr. (left inset) $\alpha_e(\nu)$ *l* vs. Δν over the range of +/- 750 MHz, calculated from the data taken at 0.53 torr (squares) and fit with Eq. (2) (line). (right inset) Same as the main figure, but with expanded axes.

The width of the saturation feature (*w*) varies significantly between the 10 μm and 20 μm fibers. Figure 4.11 below compares width, *w* from transitions measured in the 10 μm and 20 μm fibers as a function of pressure. At comparable pressures, *w* is consistently greater in the 10 μm fiber over a range of powers. Again, features in the 10 μm fiber are broader than in the 20 μm fiber. Linear fits to the resulting data give intercepts of 34 MHz, 21 MHz, 18 MHz, and 19 MHz, with slopes of 10 MHz/torr, 10 MHz/torr, 7 MHz/torr, and 7 MHz/torr respectively (1 torr= 133 Pa). These are smaller than the pressure broadening measured in higher-pressure

systems, but the discrepancy may be due to the reduction in power broadening at higher pressure, due to stronger attenuation of the pump beam.

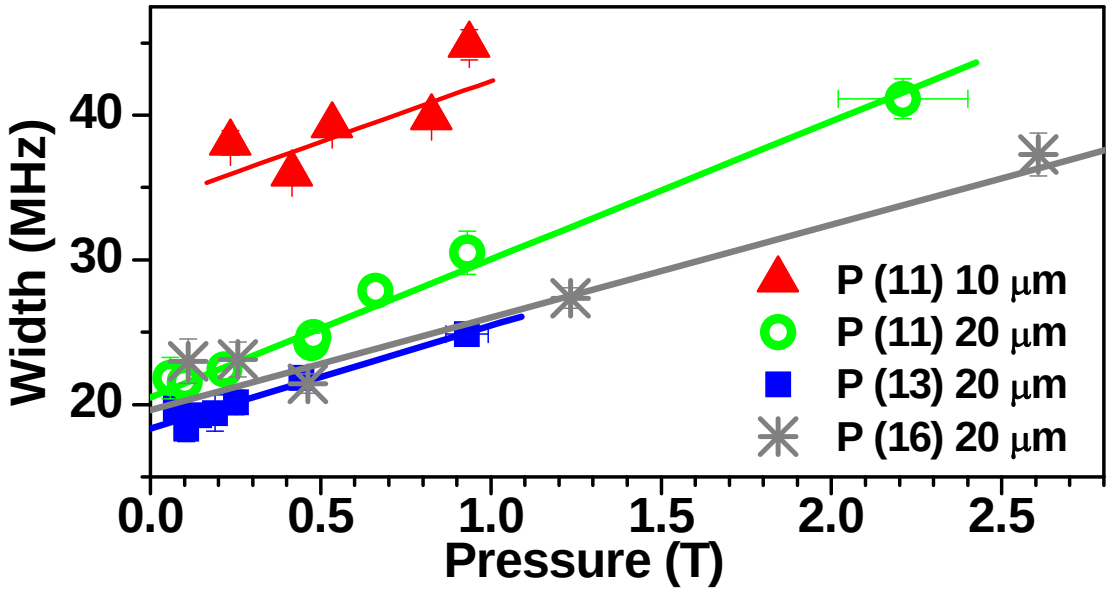

Figure 4.11. Full width at half maximum (*w*) vs. pressure for P (11), P (13), and P (16) transitions in the 10 μm and 20 μm diameter PBG fibers. Linear fits to the resulting data give intercepts of 34 MHz, 21 MHz, 18 MHz, and 19 MHz, with slopes of 10 MHz/torr, 10 MHz/torr, 7 MHz/torr, and 7 MHz/torr respectively (1 torr= 133 Pa).

The measured width *w* is expected to reflect broadening of the natural line width (~kHz) due to power, pressure, and interaction time between the molecules and the laser beam. The y-intercept of Fig. 4.11 data give the γ of Eq. 4.39 without power broadening, and should reflect pressure broadening and interaction time broadening. Once the pressure broadening of ~11.5 MHz/torr [99] is subtracted, the resulting widths of 16 MHz and 24 MHz in the 20 μm and 10 μm fiber diameters, respectively, reflect the interaction time broadening, the cause of which may be modeled by wall collisions (γ_{col}^{wall}) as discussed in Benabid *et al.*[24] or transit time (γ_{tt}). The transit time limited width can be approximated as $\gamma_{tt} = 0.375\ v/r_{1/e}$ [117], where v is the thermal velocity, which gives 25 MHz and 43 MHz for the same fibers with 1/*e* mode field diameters of 13 μm and 7.5 μm, respectively. Estimates for wall collision rates give similar values. Both γ_{col}^{wall} and γ_{tt} give the same scaling with fiber diameter.

Figure 4.12 below shows the power broadening effect on the width of the sub-Doppler profile. Fits of the three data sets shown in Fig. 4.9 to $\Gamma_S^*(z=0)=\gamma\left(1+\sqrt{1+S_0(z=0)}\right)/2$ yield γ values of (34 MHz, 26 MHz, and 27 MHz) and P_S values of (17 mW, 49 mW, and 43 mW) respectively. These fits neglect the significant effect of pump attenuation, but offer insight into the physical broadening mechanisms. For example, the y-intercept, γ, is clearly larger in the case of the 10 μm fiber.

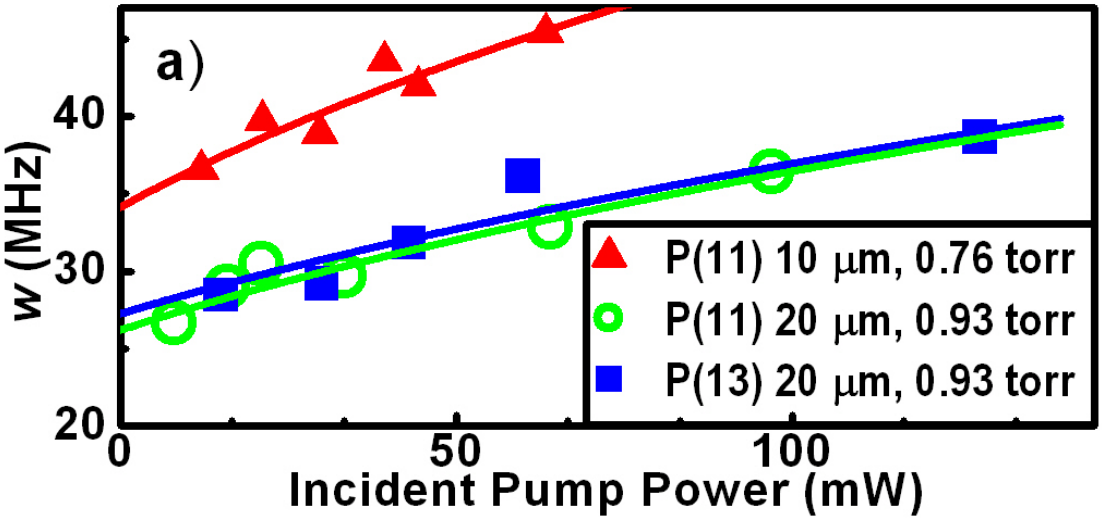

Figure 4.12. Full width at half maximum (w) vs. injected pump power for P(11) and P(13) transitions in the 10 μm and 20 μm diameter PBG fibers. The theoretical fit is based on the formalism explained in eq. 3.45. The fibers were filled to (▲) 0.76 T and (○,■) 0.93 T.

In particular, we are interested in the determination of the optimum pressure for the maximum signal slope. The maximum signal slope will have the larger signal with smaller width which in turn gives the better resolution of the peak frequency. A figure of merit for a frequency reference, "discrimination" (D), can be calculated based on the fractional change in optical power transmission divided by the transition width.

$$D=\frac{e^{-A_g\cdot(1-A_l)}-e^{-A_g}}{\omega_l}$$

where A_g is the amplitude of the Gaussian profile and A_g times A_l is the amplitude of the narrow feature. The value of D is thus proportional to the derivative signal obtained from modulation

spectroscopy, which would be required in order to peak-lock a laser to the saturated absorption feature.

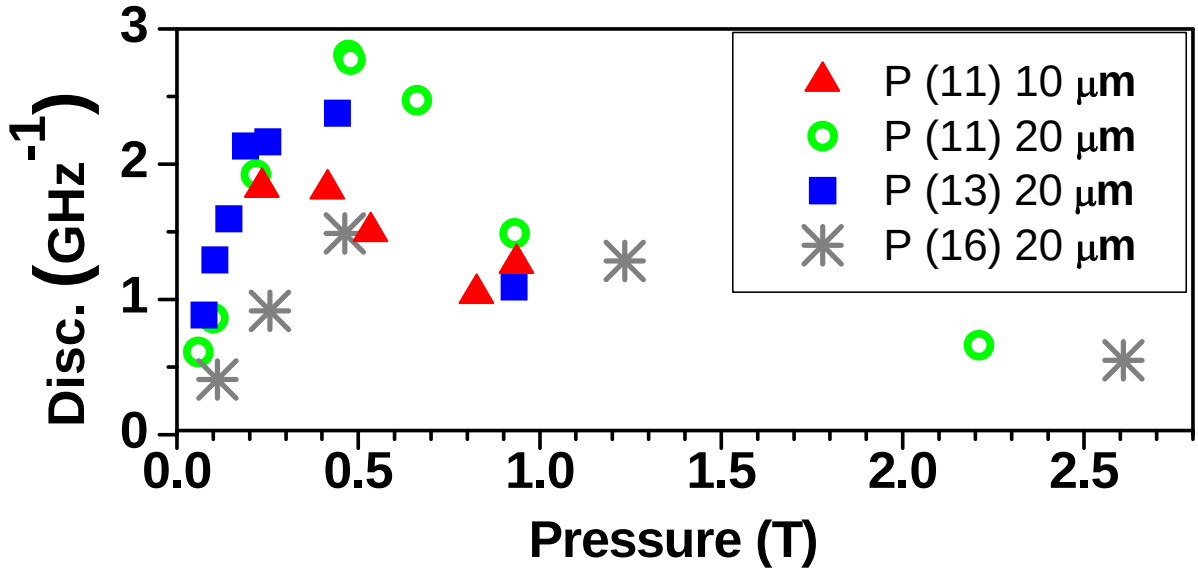

Figure 4.13. Graph shows *D*, the figure of merit for the frequency discrimination of the signals. For comparison, the Doppler-broadened resonances of Benabid *et al.*[24] have a *D* of about 1 kHz^{-1}, while the cavity-based standards have *D* = 40 kHz^{-1} . Thus the discrimination of PBG fiber-based references does not yet rival cavity-based standards, but is clearly superior to Doppler-broadened lines. The optimum conditions for operating a frequency reference at a given input pump power inside PBG fiber can be deduced from this plot. P(11) data were taken at a higher pump power than the P(13), and therefore exhibit a higher value of *D*. The optimum pressure is expected to depend nearly inversely on fiber length for long fibers.

To figure out the saturation parameter, we have initially used the calculation based on the expression $\Gamma_S^*(z=0)=\gamma\left(1+\sqrt{1+S_0(z=0)}\right)/2$ for γ values of 34 MHz, 26 MHz, and 27 MHz, which gives saturation power of P_S values of (17 mW, 49 mW, and 43 mW) respectively. As I mentioned above, this does not take into account pump attenuation. We then simulated the experiment by dividing fiber into large number of very small section so that we can use Beer's law in each fine section of the fiber. Then we repeat the procedure through the fiber so that we

get the saturated absorption signal of the probe in presence of the pump. To simulate the experiment, experimental values of $P_u(z=0)$, $P_r(z=l)$, α_0, P_s and γ are chosen, and then P_u and P_r are propagated along the fiber numerically. P_s and γ are varied independently until the amplitude and width of the simulated signal match that of the experiment. The measurement based on measured attenuation of the pump beam gives 22 ± 4 mW of saturation power, in agreement with Henningsen *et al.* .[119] using the same approach. Error in both cases is primarily systematic, and found by taking the standard deviation of ~ 20 measurements. The discrepancy between the two approaches remains unresolved.

We have investigated saturation spectroscopy inside large-core PBG fiber, and observed narrower transitions and much cleaner signals than those observed in smaller PBG fibers. Thus the larger core fibers appear to be much less sensitive to surface mode contamination. This is consistent with the predictions and observations of West *et al.*[118]. We have optimized the conditions to maximize the signal inside the 20 μm fiber. Larger core fibers should result in increasingly narrow lines.

4.5. Saturation absorption spectroscopy in Kagome fiber

We have recently formed an informal collaboration with Fetah Benabid and his group at the University of Bath, United Kingdom, to study saturation absorption of acetylene inside new large-pitch kagome fibers [120]. These fibers were recently designed and demonstrated by the Bath group. Benabid's group sent us some of this fiber, and we have done pressure and power studies on saturated absorption in these fibers, and some of the results are reported below. Benbid's group has also studied EIT in Rb inside these fibers [121] to demonstrate their usefulness.

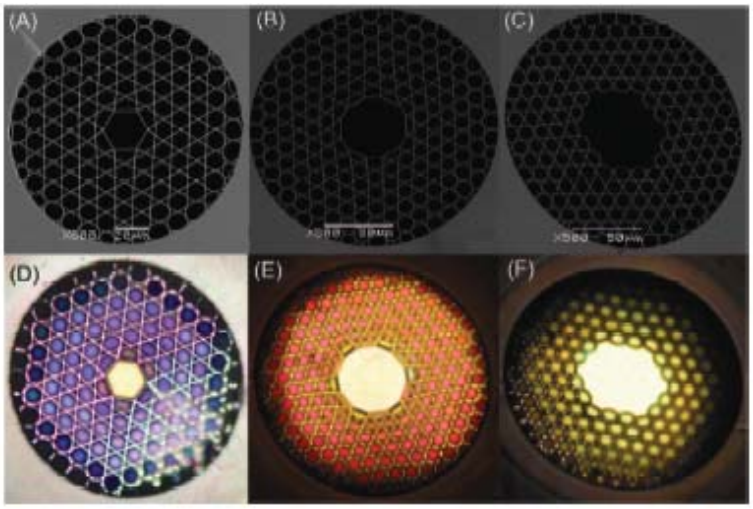

Figure 4.14. (A) – (C) SEM images and (D)–(F) Optical micrographs of the single-cell, 7-cell, and 19-cell defect fibers. The single, 7-cell, and 19-cell fibers have diameters (min/max) of 22.3/26.1, 43.7/45.4, and 47.8/68.3 μm respectively. Figure taken from Fig. 1 of Ref. [121]

These fibers not only offer larger cores (up to 70 μm), but they also have improved optical properties such as much smaller surface mode coupling and larger infrared and optical transmission regions as compared to PBG fibers. Fetah Benabid's group sent us the fiber and we carried out saturation absorption spectroscopy in 19-cell kagome fibers, and found that they can give smaller linewidths and larger linewidth slopes as compared to PBG fibers. The setup for saturation absorption spectroscopy with kagome fiber is similar to PBG fibers except we replace PBG fiber with kagome and we now have two additional CW fiber laser sources instead of only the diode laser which we described in the previous PBG fiber setup. These fiber lasers purchased from Orbits Lightwave, Inc. have narrow linewidth (~500 Hz at 100 ms) and higher power (25 mW). They are extremely robust and stable CW laser sources, but their tuning range is only 10 GHz, so only a single ro-vibrational transition is accessible. Therefore we specified that the lasers should be centered near the P(13) line of acetylene, unlike the diode laser which can scan the entire P-branch of the acetylene lines.

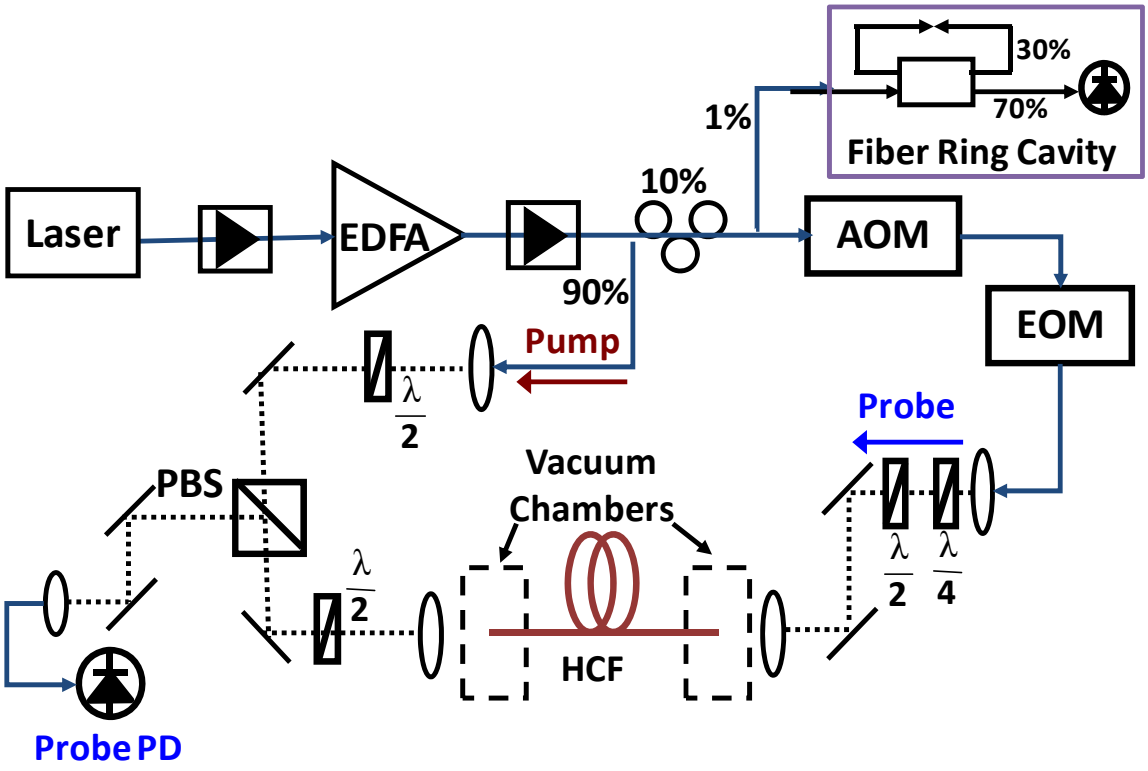

Figure 4.15. Saturated absorption spectroscopy setup inside 19-cell, ~70 µm core diameter kagome hollow core fiber (HCF. erbium doped fiber amplifier (EDFA), photo-detector (PD), polarizing beam splitter (PBS), acousto-optic modulator (AOM), and electro-optic modulator (EOM).

The light from either the diode laser (~ 5 mW) or the fiber laser (~4.5 mW) is amplified using an EDFA to achieve output powers up to 300 mW. The amplified power is split into two parts as a pump and probe as shown in Fig. 4.2. Most of the amplified (~ 90%) light goes to the pump and the rest is passed through an AOM which shifts the frequency by ~50 MHz. The AOM helps to minimize noise by forcing the interference between the pump and probe beams to occur at a frequency too fast to detect. The light is then passed through the EOM which has no use here except that we use it afterward for frequency modulation spectroscopy setup only (discussed in Chapter 6). Finally, the pump and probe are coupled inside the fiber in opposite directions. Polarizing beam splitter, half-wave plate and quarter-wave plate are used to make pump and probe polarization orthogonal so that probe can be detected separately from the pump. They also help to reduce the back reflection of the pump that is detected by the probe photo detector.

Saturation spectra were recorded for different pressure and power values. The kagome data show a further reduction in linewidth to less than 10 MHz at 100 mW of pump power, and to even lower widths at 30 mW pump power, comparable to the data taken for the HC-PCF's. We then calculated a measure of the slope of the sub-Doppler feature and called it the discrimination, *D*, for the saturation signal for kagome setup. The *D* values observed in kagome are more than 2 times larger than those observed inside 7- and 19-cell HC-PCFs at comparable powers; it is due to narrower linewidth at comparable signal strength. The discrimination and width vs. pressure graph for kagome fiber. (The particular data shown in Fig. 4.16 and Fig 4.17 for kagome fiber with green hexagon and green star is taken by my colleagues Kevin Knabe.)

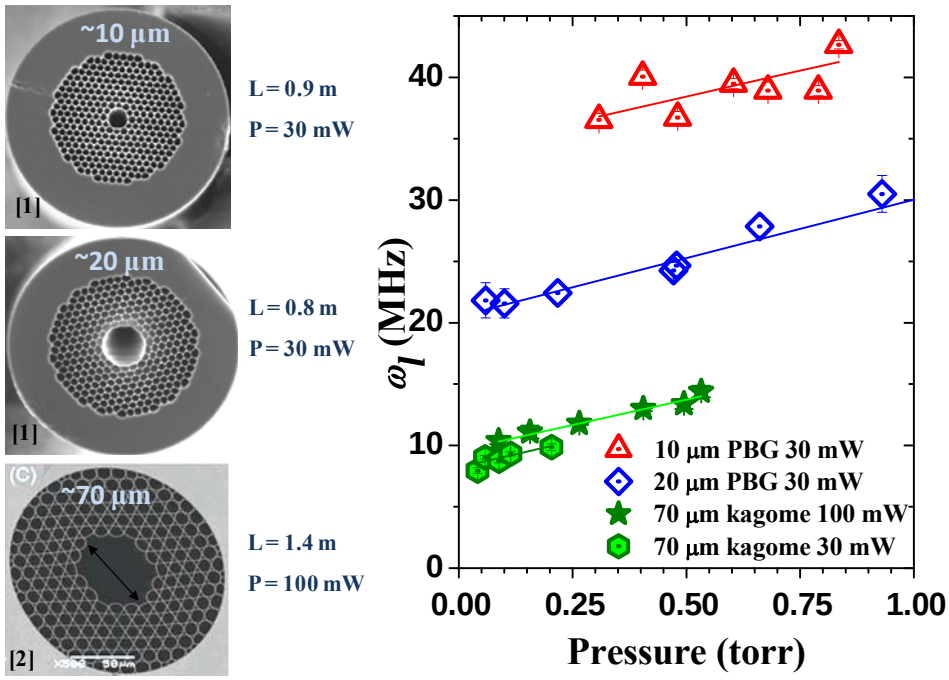

Figure 4.16. Sub-Doppler FWHM width ω_I vs pressure for different core size and types of fiber. The cross-section of the fiber has been shown from reference [1], Crystal Fiber A/S, www.crystal-fibre.com for 10 µm and 20 µm PBG fiber, and reference [2] F. Couny, ***et al.***,Optics Letter 31 (2006) for ~70 µm kagome fiber. The widths of the 10 µm (red triangle) and 20 µm (blue diamond) PBG fibers are shown here for comparison with the kagome spectra (green hexagon and green star). The 10 µm PBG fiber was 0.9 m long and had an optical power of 30 mW, the 20 µm PBG fiber was 0.8 m long and had an optical power of 29 mW, and the kagome fiber was 1.4 m long and had an optical power of 92 mW. The filled green hexagon indicates a point taken at 30 mW of pump power exiting the kagome fiber**.**

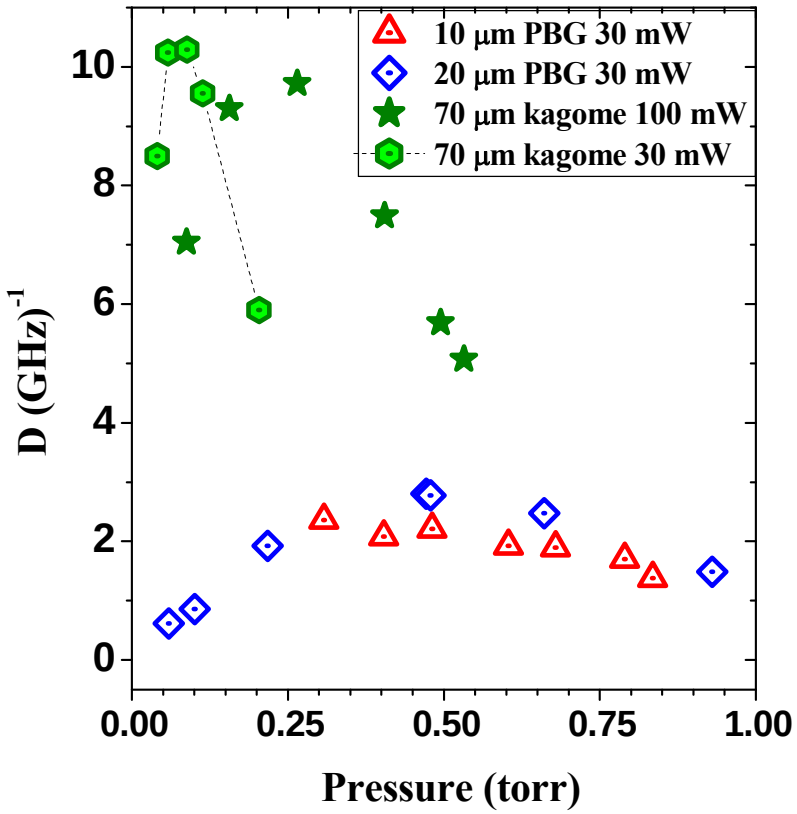

Figure 4.17. Discrimination,*D*, versus pressure inside the fiber for different optical pump power exiting the fiber 10 µm (red triangle) and 20 µm (blue diamond) PBG fibers and 70 µm kagome fiber (green hexagon and green star). The D values observed in kagome are more than 2 times larger than those observed inside 7- and 19-cell HC-PCFs at comparable powers.

The narrower line and smoother background transmission make the large-core kagome fiber a likely candidate for portable acetylene-based frequency references. But one subtle problem with kagome fiber is the mismatch between its outer diameter (300 micron) and SMF (125 microns) which makes splicing very difficult. Since we want to develop a portable fiber cell, splicing is an integral part of our research. We are in the process of investigating how to splice (or at least seal) large-core kagome fiber. But we have successfully spliced 10 µm and 20 µm PBG fiber. The next Chapter basically focuses on the splicing of 10 µm and 20 µm PBG fibers with single mode fiber (SMF 28).

CHAPTER 5 - Fiber splicing: towards portable fiber cell

Photonic bandgap fibers (PBGF) are optical waveguides that will serve as a key technology to enable future advances in frequency metrology, spectroscopy, and quantum optics. A PBGF is a low-loss waveguide whose hollow core can be filled with a fluid. This allows light to interact with the fluid while being guided by the PBGF geometry. Recently, much progress has been made using gas-filled PBGF. For instance, resonant interactions and electromagnetically-induced transparency have been observed in acetylene-filled fibers with applications toward all-optical fiber communications [23, 122]. Saturation spectroscopy, for higher-accuracy portable optical frequency references, has also been demonstrated [123, 124]. Even linear interactions are significantly enhanced, resulting in the development of gas sensors [125] and Doppler- and pressure-broadened frequency references [14, 126].

Splices between microstructured fibers and step index single-mode fiber (SMF) are difficult to create, because the air holes in the fiber tend to collapse at the high temperatures required to form a strong splice (see Ref. [127] and references therein). Splicing solid-core microstructured optical fibers to SMF is typically accomplished with filament splicers [14, 128, 129], but has also been demonstrated using an arc splicer [130]. Indeed, splicing SMF to hollow-core PBGF is even more difficult due to the presence of the large guiding hole, and this difficulty limits the use of these fibers in laboratory experiments or in commercial products. However, successful splices between hollow-core PBGF and SMF have been made using a filament-based fusion splicer, and are commercially available [131]. Furthermore, arc splicers have been used to systematically investigate the collapse of air holes in PBGF for selective injection [132], but until now, no low-loss, robust splices have been made with the relatively inexpensive and ubiquitous arc fusion splicer.

Many applications of PBGF require the fabrication of a PBGF cell, in which a length of PGBF is filled with a gas or liquid and spliced to solid-core single-mode fiber on each end. This cell is doubly difficult to produce since 1) two low-loss splices between the SMF and PBGF fiber must be made and 2) at least one splice must be made while keeping the gas in the PBGF microstructures. Such PBGF cells have been created [14, 126, 128] where the first splice between the PBGF and SMF is made in air, while the second splice to SMF must be made in a gas atmosphere. In fact, PBGF have been sealed after being filled by acetylene gas [14], but this

technique relies on the use of an expensive, filament-based fusion splicer. Another clever method of making gas-filled PBGF cells involves splicing the PBGF to SMF in a helium and acetylene gas purge using a filament splicer [128]. The helium diffuses from the PBGF, leaving only high purity acetylene in the cell. Nevertheless, a simple recipe for splicing PBGF to SMF using a conventional arc fusion splicer has until now been lacking. Here we demonstrate a repeatable, robust, low-loss splice between a hollow-core PBGF and SMF. The performance of this fiber compares favorably with a commercially made spliced fiber.

5.1. Fusion splicing hollow-core PBGF to SMF

Two types of hollow-core PBGF, both purchased from Crystal Fibre A/S, are discussed in this study. The PBGFs were spliced to Corning® SMF-28e® SMF using an Ericsson FSU-995 electric arc fusion splicer. The first PBGF, part number HC-1550-02, has a hole diameter of 10.9 μm and a mode overlap of >90 % with the SMF. The second PBGF, part number HC19-1550-01, has a hole diameter of 20 μm. The significant fiber parameters are listed in Table 1.

Table 5.1. Fiber Parameters for the PBGF and the Single-Mode Fiber

Fiber Name	Core diameter	Mode-field diameter†	Numerical Aperture†	Hole Separation Λ
HC-1550-02	10.9 μm	7.5 μm†	0.12†	3.8
HC19-1550-01	20 μm	13 μm‡	0.13‡	3.9
SMF-28e	8.2 μm	10.4 μm†	0.14	--

† Values given at 1550 nm [133]. ‡Values given at 1570 nm [134, 135].

5.1.1. Splicing procedure using an electric arc splicer

Filament splicers are generally preferred for fusion splicing PBGFs since they heat the fiber more slowly and uniformly. Our goal, which is motivated largely by the cost and popularity of arc fusion splicers, is to mimic this performance with a more common electric arc fusion splicer. One difficulty in splicing hollow-core PBGF is avoiding the collapse of the microstructures, because temperatures that are high enough to form a strong splice also allows the glass to flow. Splicing PBGF is particularly difficult using an electric arc splicer because the fibers are heated

very rapidly during the arc. Thus, we have developed a multi-step splice procedure involving a short, high current arc followed by a long, low current arc. In general, the amount of current used in this process is less than that of a conventional splicing procedure.

The geometry of the fusion splicer is illustrated in Fig. 5.1. There are two parameters that define the distance of the fibers from the electric arc and from each other. The first parameter called "gap" measures the distance between the two fibers. Zero gap, which occurs at a position called the "touch point" indicates that the fibers are butt-coupled. Negative gaps, here called "overlap", indicate that the fibers are pushed further together than they were when butt-coupled. The second parameter called "offset" indicates the displacement of the touch point from the electrode axis. In all splices, the fibers are prepared by mechanically stripping the coating away from the last ~2.5 cm of fiber, and cleaved using a Fujikura CT-04B cleaver.

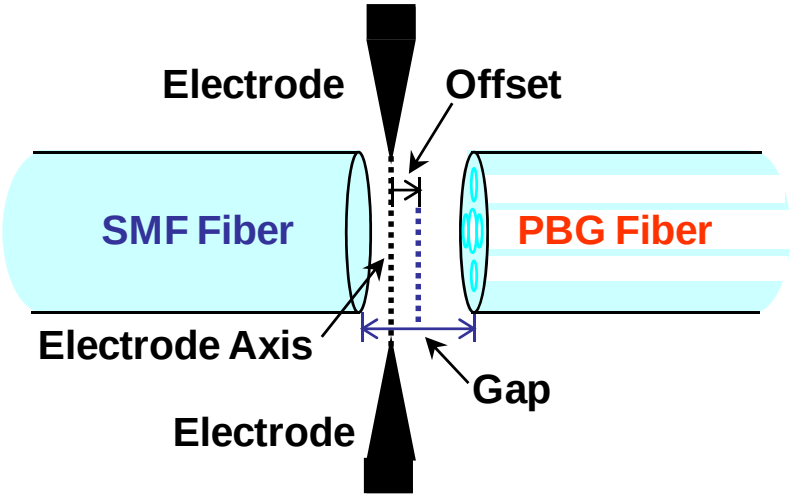

Figure 5.1. The fusion splicer geometry. Two variable parameters, gap/overlap and offset, determine the position of the fibers with respect to the electrode axis.

The optimum procedure for splicing PBGF to SMF was developed by attempting more than twenty splices with a wide range of splice parameters. The resulting optimized program for splicing SMF-28e® to the 10.9 μm PBGF HC-1550-02 is as follows. The splicing program first aligns the fibers and produces a short burst of current (pre-fuse) to remove any contamination present in the fiber end. This pre-fuse also removes any moisture in the microstructures that will cause the splice to be fragile. Next, the fibers are briefly butt-coupled at the touch point, and a gap of +10 μm is made. The offset is set to 260, placing the electrodes roughly 5 μm closer to the SMF than the PBGF (as determined using Ref. [132]). The butt-coupled loss from the SMF

to the 10.9 μm PBGF is typically 1.0 dB. The nonzero offset is a critical parameter in the splicing since it ensures that the SMF is heated more strongly than the PBGF, to prevent the collapse of the air holes [136]. Fusion current 1 is set to 10 mA and applied for 0.2 s, which softens both fiber ends and prepares the fibers to be overlapped and fused together upon physical contact in the next process. Care must be taken while choosing this current level because a low arc current leads to a mechanical deformation during the overlapping stage, while a high current causes a change in the glass geometry resulting in a poor quality splice. If fusion current 1 is reduced from the optimum splicing condition of 10 mA to 9 mA for the same duration (0.2 s), the resulting splice loss is approximately the same in both cases, but the mechanical strength of the splice is greatly reduced. If for a constant fusion current 1 (10 mA) the time is increased beyond 0.2 s, the PBGF end deforms or collapses completely under surface tension, forming a spherical end.

Fusion current 2 starts when the fiber ends actually touch and press together in order to overlap and to fuse. During this phase, the current is reduced to 7 mA for 12 s while the fibers are pushed together to a negative gap, or overlap, of 10 μm. A larger overlap at optimum arc current would give a better mechanical strength but leads to a higher splice loss while a smaller overlap leads to lower strength but lower loss. To complete the procedure the fusion current 3 is set to 6.5 mA for 3 s, while the splice anneals. Figure 5.2 illustrates the loss with respect to the butt-coupled transmission measured during the splicing procedure.

The splice routine was altered for splicing the SMF-28e® to the 20 μm PBGF HC19-1550-01. The only significant change in the program was the increase in the overlap from 10 μm to 15 μm in order to compensate for the larger hole diameter.

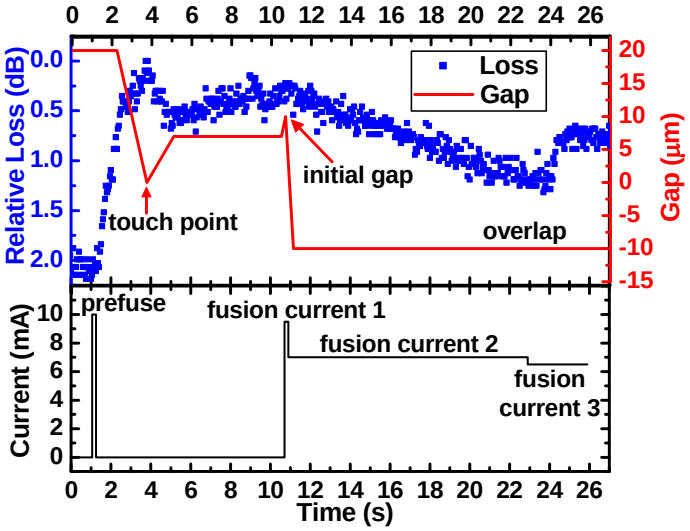

Splice Parameters		
Fiber Type	HC-1550-02	HC19-1550-01
Prefuse time	0.2 s	0.2 s
Prefuse current	10 mA	10 mA
Gap	10 μm	10 μm
Overlap	10 μm	15 μm
Fusion time 1	0.2 s	0.2 s
Fusion current 1	10 mA	10 mA
Fusion time 2	12 s	12 s
Fusion current 2	7 mA	7 mA
Fusion time 3	3 s	3 s
Fusion current 3	6.5 mA	6.5 mA
Offset	260	260

Figure 5.2. The relative loss with respect to the butt-coupled transmission from the SMF to the 10.9 μm PBGF during the fusion procedure. The gap curve is estimated from the splice parameters, the Ericsson FSU-995-FA fusion splicer manual, and the relative loss curve.

5.1.2. Splice loss between SMF and PBGF

The splice loss is determined directly by measuring the transmission of a 1534 nm laser source through the splice, in both directions, using the following procedure. To measure the loss from SMF to PBG, first the CW laser light is injected into the SMF fiber and the output power is measured. Then the SMF is spliced to the PBGF and the output power from the PBGF is measured. To measure the splice loss from the PBGF to SMF, the other end of the PBGF is subsequently spliced to another SMF and the output power is again measured.

The measured loss for splices of SMF to both the 20 μm and the 10.9 μm PBGFs are listed in Table 5.2. For both splices, the most unique feature is the non-reciprocity of the splice loss: the splice loss as measured from the SMF to PBGF is different from that measured in the opposite direction from the PBGF to SMF. In the 20 μm HC19-1550-01 fiber, splice loss from SMF to PBGF varies from 0.3 dB to 0.5 dB whereas splice loss from PBGF to SMF is more than 2 dB. The splice loss non-reciprocity is less prominent in 10.9 μm PBGF.

Table 5.2. Measured Non-Reciprocal Splice Loss between PBGF to SMF

Fiber Name	Core diameter	Mode-field diameter†	Numerical Aperture†	Hole Separation Λ
HC-1550-02	10.9 μm	7.5 μm†	0.12†	3.8
HC19-1550-01	20 μm	13 μm‡	0.13‡	3.9
SMF-28e	8.2 μm	10.4 μm†	0.14	--

†Value was determined indirectly from the transmission through 20 μm PBGF cells.

Unfortunately, the splice loss depends on the orientation of the PBGF. To see this effect, fiber cells of both 10.9 and 20 μm fiber were made and the splices were fixed to a table. For example when one 20 μm PBGF cell was moved randomly, the loss varied erratically from 2.2 to 6.0 dB through the entire cell. For a 10.9 μm fiber cell a smaller change from 4.2 to 5.3 dB was observed.

A physical explanation of the observed splice loss is difficult due in part to the complicated mode structure of the PBGF. This measured splice loss can be explained rigorously by computing the overlap integral between the PBGF and SMF modes. Unfortunately the determination of this integral is impossible since the amount of energy in each guided mode is typically unknown [127]. Also, it is difficult to compute the number of modes of the PBGF without resorting to a numerical method for computing the modes.

Qualitative arguments based on the theory of step-index fibers [137] can be used to explain the observed loss and the non-reciprocal loss. An estimate of the minimum loss can be computed from the mode overlap of two Gaussian profiles with mode field radii r_1 and r_2. This overlap integral (assuming no axial mismatch) can be evaluated to give the minimum splice loss in dB as [138]

$$10Log_{10}\left(4r_1^2r_2^2\left(r_1^2+r_2^2\right)^{-2}\right) \tag{5.1}$$

Using this equation the minimum loss for the 10 μm PBGF to SMF splice is 0.45 dB while the minimum splice loss for the 20 μm PBGF to SMF splice is 0.21 dB. Interestingly, this approximation predicts that the 20 μm PBGF will have a lower minimum splice loss than the 10.9 μm PBGF, which is indeed observed.

The crude splice loss approximation given in Eq. 5.1 based on mode-field radii does not predict the non-reciprocal loss. However, this non-reciprocal loss can be explained in terms of

mode mismatching between multimode waveguides [139]. The problem here is similar to the coupling between a SMF and a multimode fiber (MMF) at a given optical wavelength. For this scenario, there is a general rule that the loss from a small core fiber to a large core fiber be smaller than the loss in the other direction. In the case of coupling from SMF to MMF the loss is expected to be small [127]. The mode field radius of the SMF is smaller than that of the MMF so it can easily couple to the lowest order modes of the MMF. The opposite behavior occurs when coupling from the MMF to SMF. Here, higher order modes will be excited in the MMF that will not couple well to the SMF. From these arguments, it is expected that a larger asymmetry in splice loss will occur with a larger number of modes in the PBGF. Due to its larger diameter, the 20 μm PBGF supports more modes (~ 10 modes) than the 10.9 μm fiber (~ 1-3 modes). Thus the HC19-1550-01/SMF-28e splice should exhibit a more prominent non-reciprocal splice loss than the 10 μm PBGF. As described above, the 20 μm PBGF to SMF loss was much more susceptible to fiber positioning than the 10.9 μm PBGF to SMF loss. The observation is consistent with the 20 μm PBGF containing more modes than the 10.9 μm PBGF.

Figure 3 shows a micrograph of the HC-1550-02/SMF-28e splice. In general the splices are mechanically strong and can be bent to a ~1.5 cm circular radius before breaking.

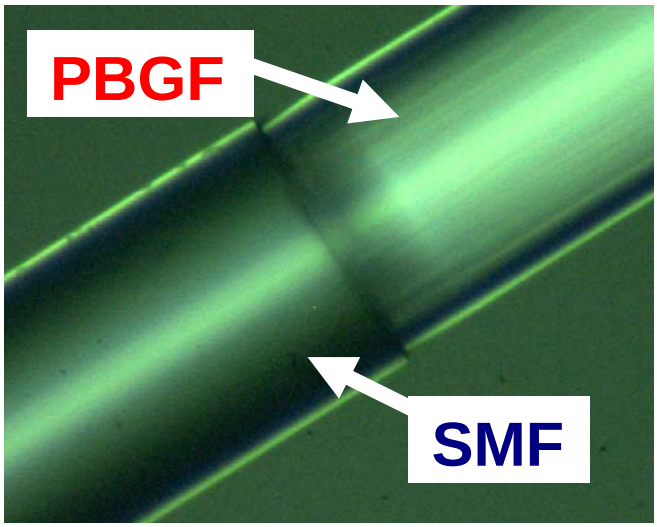

Figure 5.3. A micrograph showing the splice between the SMF and 10.9 μm PBGF. Picture courtesy of the GaN Group in the Kansas State University Physics Department.

5.2. PBGF-SMF splice for a gas-filled PBGF cell

One important application of PBGF-SMF splices is in the creation of gas-filled PBGF cells. Saturated absorption spectroscopy on such cells is a promising technology for portable optical frequency references, but sensitive to the splice quality. This sensitivity arises because light reflected from both splices can form a standing wave as in a Fabry-Perot cavity, and thus the fiber cell transmission depends periodically on optical frequency. This frequency-dependent "background" creates a shift in the apparent line center of the absorption feature of the reference gas, such as acetylene, and thus degrades the performance of the frequency reference.

5.2.1. Absorption spectroscopy

The splices will be useful in a PBGF cell, as demonstrated using saturation spectroscopy on acetylene inside PBGF that is spliced to SMF fiber. Several different fibers and splices are then compared. The experimental setup is shown in Fig. 5.4, and is similar to that of Ref. [124]. Here, a PBGF spliced to SMF is evacuated by pumping with a mechanical roughing pump on the PBGF's open end in a vacuum chamber. The fiber is evacuated to ~15 mtorr over 12 hours. Then the vacuum chamber and PBGF are filled with acetylene gas to a pressure of 0.9 torr. Absorption spectroscopy on the gas in the PBGF reveals a strong absorption feature. Light from a ~1531 nm tunable diode laser is amplified by an erbium-doped fiber amplifier and split to produce a probe (~1 mW) and pump (~30 mW). The probe beam passes through a double-passed acousto-optic modulator, an isolator, and a polarization controller, and then counter-propagates the pump beam through the PBGF. The transmitted probe beam power is detected by a photodetector as the diode laser frequency scans across the absorption feature. The laser is swept eight times across the signal, and the eight traces are averaged on an oscilloscope.

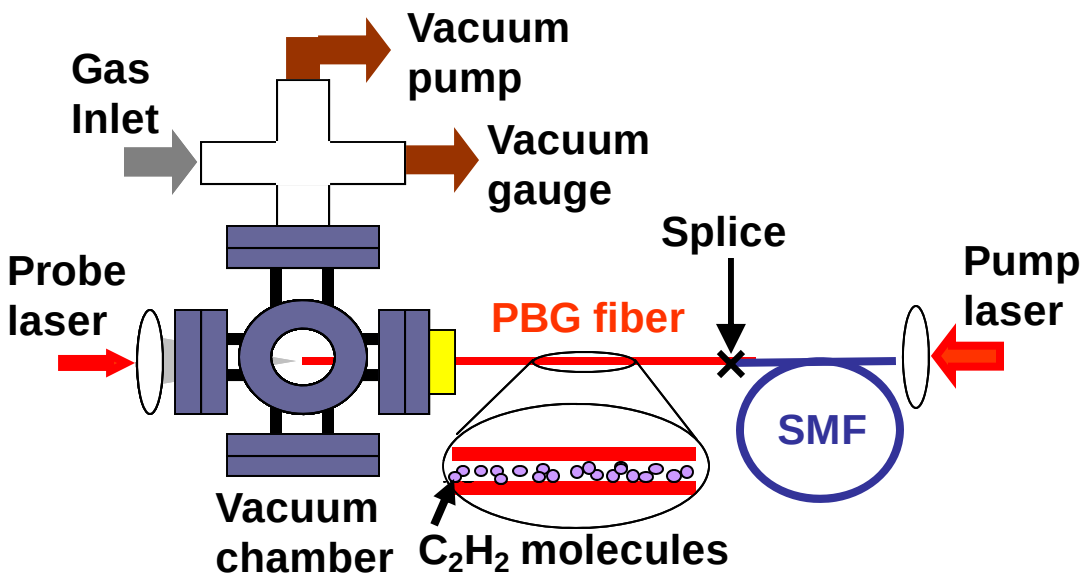

Figure 5.4. Chamber used to evacuate and fill the PBGF with acetylene gas for saturated absorption spectroscopy.

Saturated absorption spectra are shown in Fig. 5; here the spectra between different 10.9 μm and 20 μm fibers are compared. Figure 5.5(a) compares three 10.9 μm PBGFs: Fiber 1 is spliced to SMF with an arc splicer as described above; Fiber 2 (purchased from Crystal Fibre) is spliced to SMF with a commercial filament fusion splicer [131]; and Fiber 3 is unspliced. Figure 5.5(b) compares two 20 μm PBGFs: Fiber 4 is spliced to SMF with an arc splicer as described above, and Fiber 5 is unspliced. Two vacuum chambers where used to perform the saturation spectroscopy on the unspliced PBGFs [124]. The 10.9 μm fibers exhibit some dependence of transmission with frequency, with similar interference fringe contrast ratios of ~5%-10%. In contrast, the 20 μm fiber splices exhibit much smaller interference fringe contrast ratios of less than 0.5%. Thus these fringes are not thought to arise from the splice, but rather to be intrinsic to the fiber, due for example to mode beating associated with the excitation of surface modes. In both cases the splice does not significantly impact the quality of the saturated absorption feature. Of course, a fiber cell requires two splices, one of which can be made by the above method. Further investigations will be required to characterize and minimize the impact of reflections from a second splice on the signal quality of the cell.

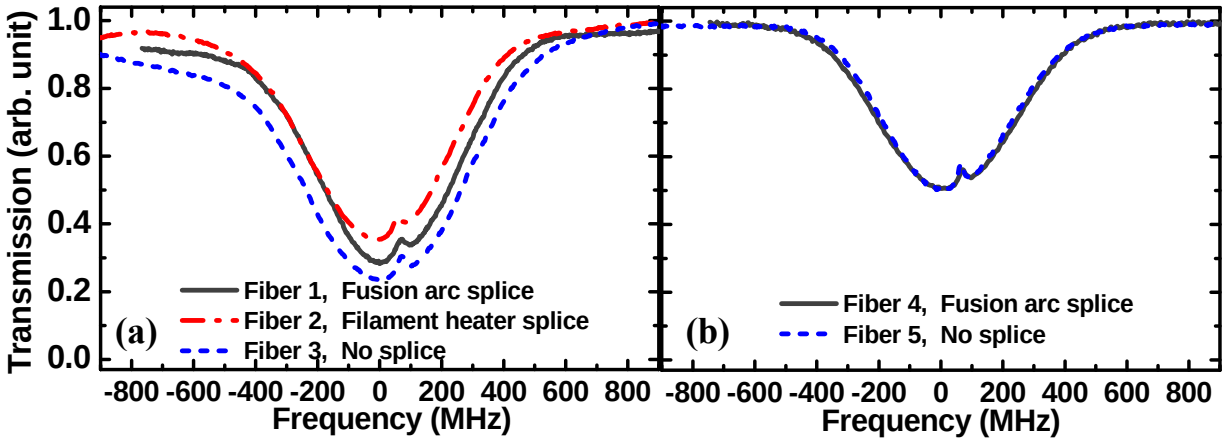

Figure 5.5. Saturated absorption spectra in (a) 10.9 μm and b) 20 μm diameter PBGFs. Fiber 1 is 0.78 m long, spliced to SMF using a conventional arc splicer using the technique described in this paper. The P(11) spectrum was taken at 29 mW and 0.9 torr. Fiber 2 is 2.0 m long, spliced to SMF by Crystal Fibre A/S using a filament heating splicer, and its spectrum is taken of the weaker P(12) transition at 17 mW and 0.8 torr. Fiber 3 is the unspliced 10.9 μm fiber of 0.9 m long, the P(11) spectrum was taken at 30 mW of pump power at 0.6 torr. Fiber 4 is 40 cm long, spliced with an arc splicer to SMF, the P(11) spectrum was taken at 34 mW and 0.9 torr. Fiber 5 is unspliced fiber 78 cm long, and the P(11) spectrum was taken at 29 mW of pump power at 0.7 torr.

5.2.2. Reflected pump spectroscopy

It was long been realized that saturation spectroscopy can be performed where the probe beam is created by retro-reflecting the pump beam back through the cavity using a mirror external to the cavity [116, 140]. We have implemented a similar setup to exploit reflection of the pump beam from the spliced interface as a probe light to perform saturation spectroscopy inside a hollow core photonic band gap fiber. To the best of our knowledge this is first of its kind to realize reflected pump inside a hollow core fiber. We called this reflected pump spectroscopy. This method simplifies setup for pump-probe spectroscopy significantly since we do not require any optics on the probe side. This also eliminates some extra sources of noise due to the presence of more optics which can create some interference noise and spurious signal. After investigating signal quality from reflected pump spectroscopy, we figured out this method is suitable for

saturation spectroscopy, frequency modulation spectroscopy [116] and maybe many others. We splice hollow core photonic band gap fiber (PBGF) with single mode fiber (SMF) and fill the spliced fiber with acetylene gas to probe P-branch of the $\nu_1 + \nu_3$ overtone transition of $^{12}C_2H_2$. Additionally, we used frequency modulation spectroscopy to lock the diode laser to these narrow saturation features to realize an all fiber frequency reference in the near-infrared spectral region.

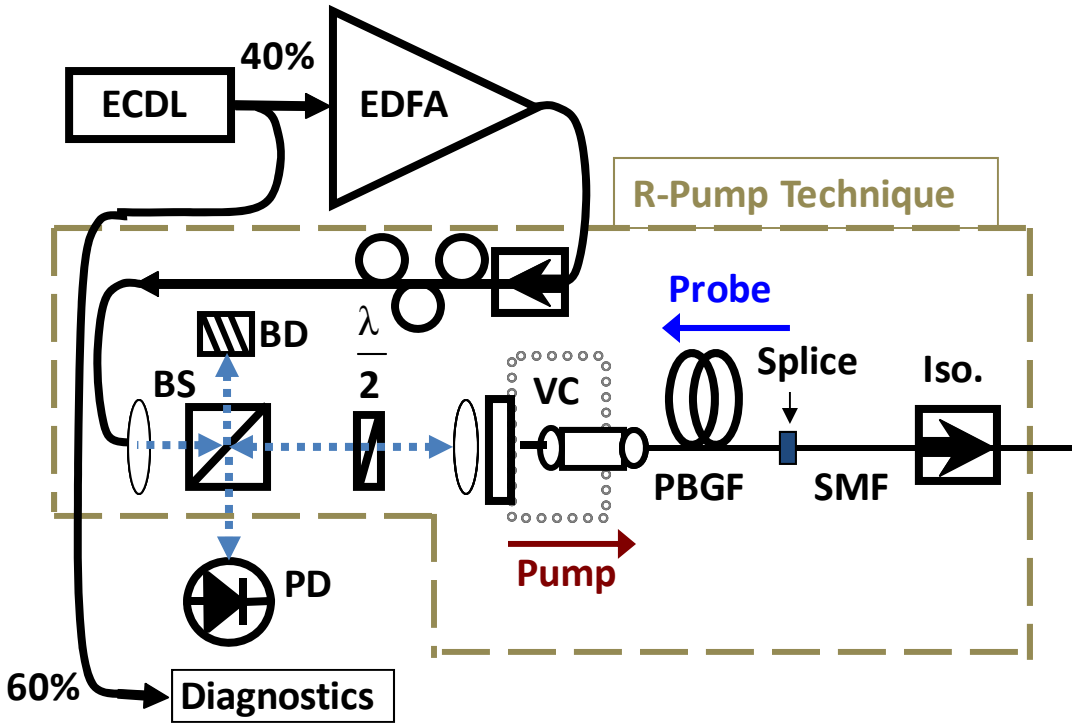

Figure 5.6. Schematic of the reflected pump technique, where the probe beam is created at the splice interface between the PBGF and SMF. Solid lines indicate laser beams contained within fibers, whereas short blue dashed lines indicate beams in free-space. Beam dump (BD), beamsplitter (BS), Isolator (Iso.), Polarization Controller (PC), Photodetector (PD), Vacuum Chamber (VC).

In two beam conventional technique, it is required to optimize careful polarization management and frequency shifting to minimize interference and spurious noise. As we discussed previously in the conventional method (Fig. 4.4), we double pass the AOM and shift the frequency of the probe by ~ 100 MHz so that interference between pump and probe is too fast to detect. Moreover, hollow core PBG fiber acts as a waveplate and creates random polarization to the beam propagating through the fiber, so we arrange wave plates in such a way that the exiting probe beam and any reflected pump light are orthogonally polarized. In contrast

to this, in reflected pump technique, we simply use a non polarizing beam splitter to detect the saturated absorption signal once the probe beam exits the fiber.

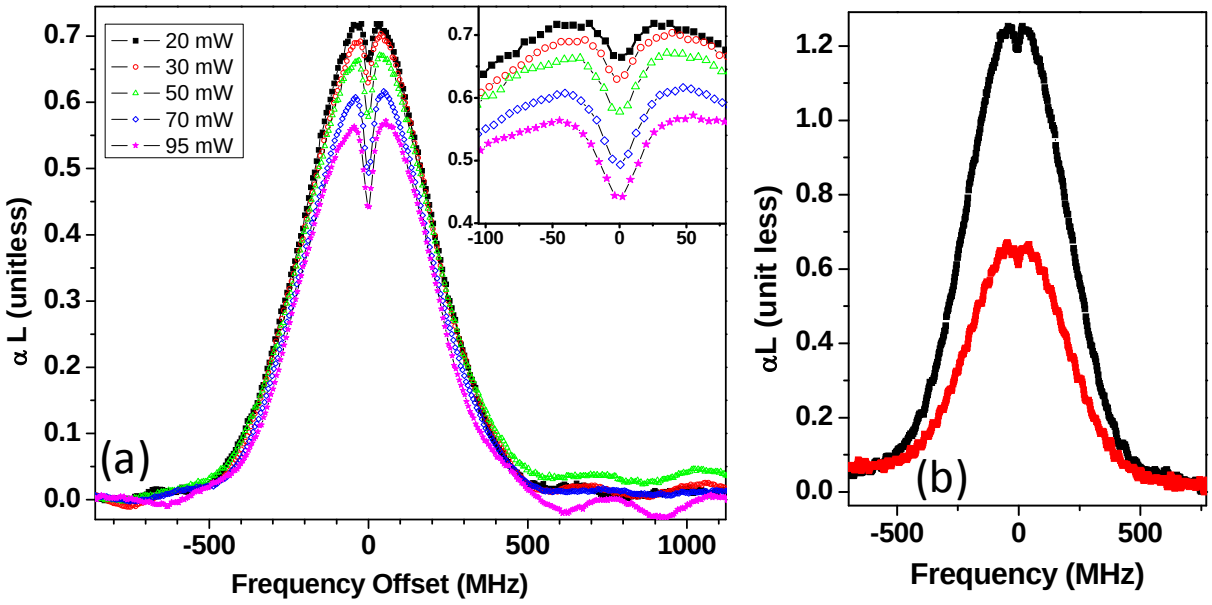

Figure 5.7 (a) Absorption spectra of the C_2H_2 $\nu_1+\nu_3$ P(11) ro-vibrational line at an optical wavelength of ~1.53 µm for 20 µm core PBGF at a pressure of 0.50 Torr for the listed pump powers. The length of the fiber was 40 cm and splice loss as seen from SMF to PBG was 0.3 to 0.5 dB. Each trace is an average of 8 scans while sweeping the frequency at ~4 GHz/s. The inset picture is zoomed-in on the narrow features of the main graph. (b) Comparison of absorption spectra between reflected pump (black) and conventional 2 beam technique (red) under identical conditions (20 µm PBGF, 40 cm long fiber, pressure = 0.93 Torr)

In reflected two beam technique, we characterize and compare these sub-Doppler features with respect to pressure, power with the conventional method in which both the pump and probe beam from same laser sources entered the fiber at opposite end. We expect the amplitude of the Doppler broadened profile to be a factor of 2 larger whereas the amplitude of the narrow feature should be a factor of 2 smaller in the limit of low pump power. This is due to the fact that the probe arises after the pump traverses the length of the fiber, so at low power the probe is absorbed twice as much as in the two beam technique since probe travels twice the length of the fiber in reflected pump setup as compare to 2 beam techniques. But this will not hold in the case when pump power reached the saturation limit. The width of the reflected pump technique for

identical condition is found to be slightly broader than that of two beam technique by approximately 5 to 10 MHz for 20 μm core PBGF.

The unique feature of the reflected pump is its power dependence of the absorption signal. As power increases to more than saturation power, absorption of two beam techniques approaches identical to reflected pump technique. Since width of the narrow feature is similar in both the techniques and discrimination is preserved, reflected pump spectroscopy is as good or better than two beam technique for saturation spectroscopy. The only drawback of the reflected pump technique is the lack of independent control of pump and probe power which may be useful in some circumstances.

CHAPTER 6 - Diode laser locking using frequency modulation spectroscopy

The technique, called Frequency Modulation Spectroscopy or FM spectroscopy, developed by Pound-Drever-Hall [141-143] is very useful for frequency stabilization of CW lasers locked to a molecular transition. This is one of the most popular techniques to achieve sensitive and rapid detection of narrow spectral features such as Doppler free spectra. This method is easy to implement with common RF components and is insensitive to intensity noise to first order. FM spectroscopy can be performed with relatively large band width laser sources.

6.1. Introduction

We use RF modulation techniques to peak-lock a CW laser to the sub-Doppler feature of a P-branch ro-vibrational transition in acetylene. Three different lasers are used for this experiment; the first is a Santec TSL-210 tunable diode laser, which gives up to 5 mW of power, tunable from 1530 nm to 1550 nm; the other two are CW fiber lasers with narrow linewidth (~500 Hz at 100 ms) and higher power (25 mW) purchased from Orbits Lightwave, Inc. We can scan the entire P-branch of the acetylene overtone transition using the diode laser. But this diode laser is a much noisier system as compared to fiber lasers. These fiber lasers are extremely robust and stable CW laser sources but they have little tunability. They can only probe the P(13) line of acetylene line unlike the diode laser. We also have two identical CW laser locking systems. Both of the systems are similar and represented by a single diagram as shown in Fig. 6.1 below. The most notable difference between the two systems is the implementation of polarization maintaining (PM) fiber. The second system uses a PM fiber laser, a PM EDFA, a PM EOM, and all PM optical patch cords. This choice was made to increase polarization control in the second system, and to note any differences between systems due to polarization instabilities. One of the fiber lasers is dedicated to work only for the PM setup and locked to the molecular line of the acetylene. So one of our fiber lasers was locked to a 1.4 m kagome fiber using the non-PM fiber system, while the other laser was locked using the PM fiber system. The setup for the first system is identical to that of Fig. 6.1 except that a fiber laser replaces the diode laser as the source.

6.2. Experimental setup

Figure 6.1 below shows the schematic of the experimental setup. The setup for the saturated absorption technique remains the same as that discussed in Chapter 4, except in this case the probe beam passes through the fiber EOM, which is driven with a digital synthesizer at a frequency of 20 MHz. The EOM distributes the power to monochromatic light into sidebands spaced by the modulation frequency around the original frequency of light. This way we can get almost half of the power into the sidebands. This signal is then passed through a sample containing the spectral feature of interest. In our case, we use $^{12}C_2H_2$ acetylene gas inside Kagome fiber. We then use a high-speed photo detector (PD) to detect the signal.

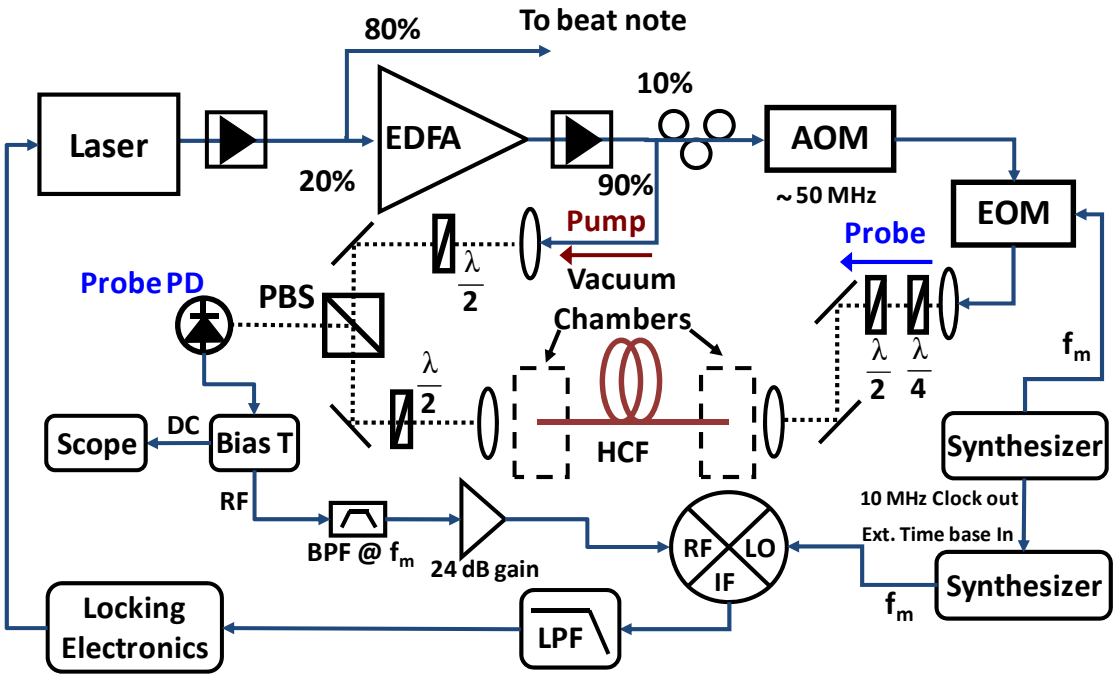

Figure 6.1. Schematic of CW laser locking using FM spectroscopy. This particular setup is for the non-PM setup which is been used to lock either the fiber laser or diode laser separately. This is nearly identical to the PM setup except that we implement polarization maintaining (PM) fiber in most of the place. In the PM setup, we use a PM EDFA, a PM EOM and all optical patch cord are PM.

Next, a Bias-T is used to separate the DC signal, which is the saturated absorption monitor signal, and the RF signal. This RF signal is filtered at 20 MHz and amplified before it is mixed with a second synthesizer modulating at f_{mod}, the phase of which can be adjusted directly on the instrument to reveal the absorption or the dispersion of the acetylene fiber system. One of

the synthesizers shares an internal time base with the other synthesizer so that all modulation shares a common clock. The output from the mixer is then passed through a low-pass filter (< 10 MHz), to get the error signal as shown in Fig. 6.2 below. Sometimes we may need to carefully fine tune the phase of the second synthesizer by observing the error signal to get the flat background. This error signal is then sent to a zero-crossing side-locking servo circuit (Precision Photonics servo box), which in turn is used to feedback to the current in the diode laser or electric transducer (PZT) in the external cavity of the fiber laser. Both the diode laser and fiber laser have a response frequency bandwidth of ~10 kHz. The frequency applied to the EOM can be optimized by monitoring this error signal. We have figured out that the largest error signals occur when the drive frequency is on the order of the FWHM of the sub-Doppler feature.

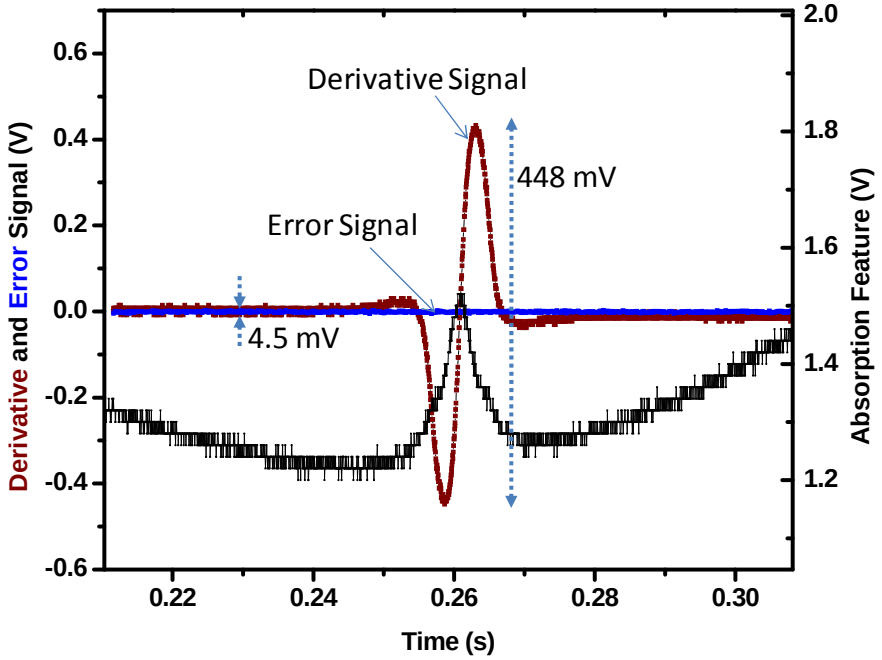

Figure 6.2. The graph shows the derivative signal, error signal and absorption feature as seen in the oscilloscope generated with the FM spectroscopy setup. The length of the fiber was 1.4 m and pressure was ~ 150 mT. We can see that the ratio of the derivative signal to error signal (also called SNR) of our locked signal is almost ~100. We can also roughly estimate the short term stability of our lock from this ratio. If the narrow feature is 10 MHz wide then our lock is stable within 10 MHz/100 = 100 kHz. (Note: the narrow absorption feature and the rest of the signals are taken at two different times and plotted together.)

In fact, a second system has been built to test the short-term stability of these fibers lasers by making direct beat note measurements between them. The second system also enables us to beat the fiber laser and diode laser together so that we can characterize noise in these different laser systems by looking at the width and noise of the beat notes.

6.3. Data analysis

We locked both fiber lasers and counted the beat frequency between them. To compare the noise in these CW laser systems, we compared the heterodyne beat between the non-PM fiber laser system and the PM fiber laser system with that between diode laser system and the PM fiber laser system. The first system is locked to P(13) - ½ $f_{AOM,1}$ and the second is locked to P(13) + ½ $f_{AOM,2}$, where $f_{AOM,i}$ is the drive frequency of the AOM in both systems, and the plus and minus signs are due to the choice of sideband from each AOM. The beat note between the lasers should occur at ½($f_{AOM,1}$ + $f_{AOM,2}$), so the sum of the AOM drive frequencies is counted alongside the beat note. The difference between the beat note and ½($f_{AOM,1}$ + $f_{AOM,2}$), gives the frequency deviations from the expected value, as shown in the black trace of Fig. 6.3a and Fig 6.3b.

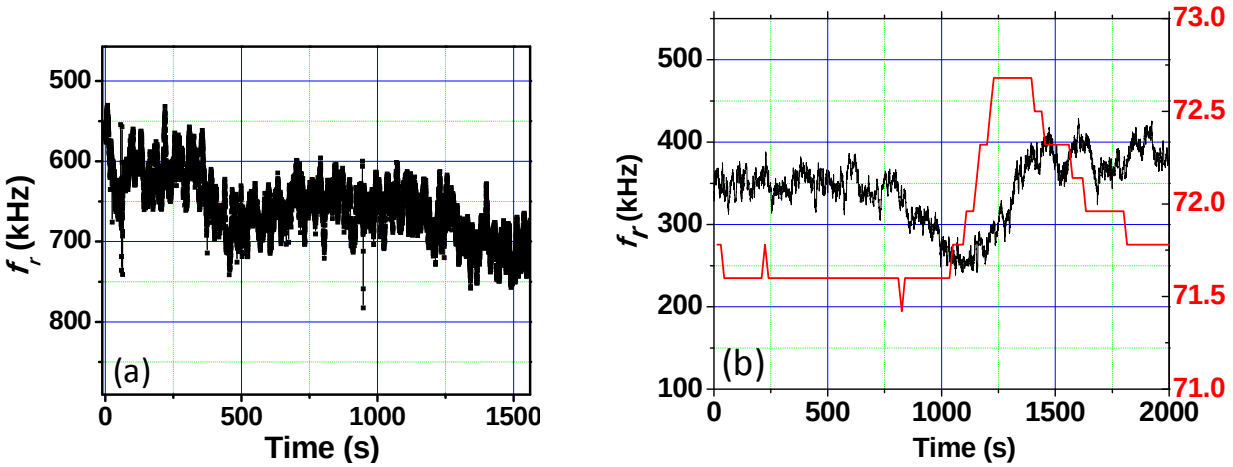

Figure 6.3. Time series measurements of the beat note at 100 ms gate time. (a) This is the count data of the beat note between the diode laser and the PM fiber laser system. Both the systems were locked. We can clearly see the 200 kHz of deviation during 35 minute of count data. (b) This is the count data of the beat note between the Non-PM and PM fiber laser systems. The PM system is in fact more robust and stable in the long run. The red trace is the temperature (°F) measured near the air conditioning unit in our lab. The laser has been locked to better than 200 kHz pk-pk as measured in-loop.

The error signal as well as the saturated absorption feature is shown in Fig. 6.4a and Fig.6.4b. These are real time snap shot of the data as seen on the oscilloscope. We can clearly see that the derivative signal of the diode laser as shown in Fig. 6.4a is not as clean as that of the fiber laser. This must be noise associated with the diode laser.

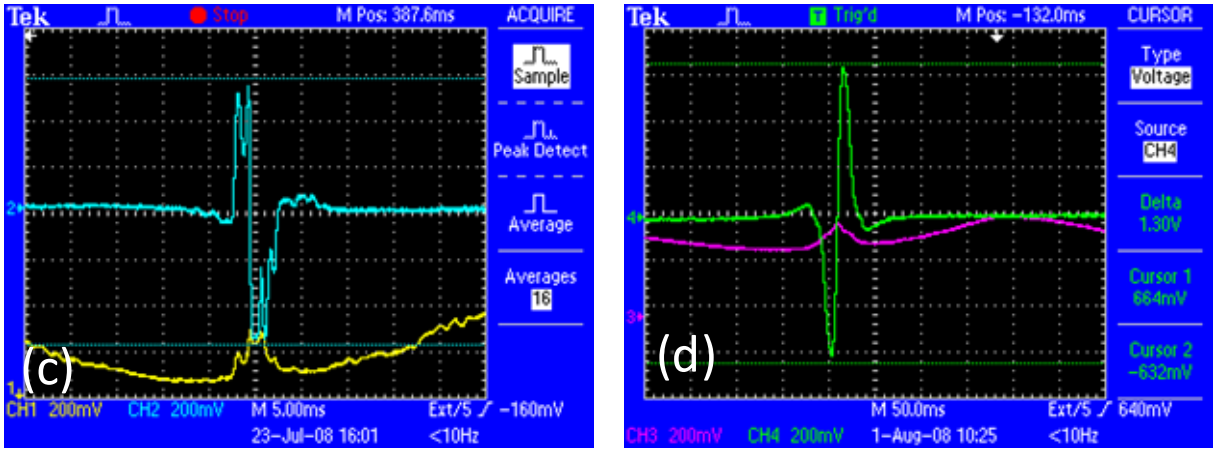

Figure 6.4. Spectra taken at the following parameters: pressure = 175 mT, pump power (exiting fiber) = 150 mW, f_m = 20 MHz. The graph shows real time trace of error signal as seen in the oscilloscope generated with the FM spectroscopy setup. (a) Error signal (sky-color) as well as typical transmission spectrum in saturation spectroscopy (yellow) for the diode laser system. We can also see some high frequency noise in the diode laser. (b)Error signal (green) and transmission spectrum (red) in PM fiber laser locking system.

Noise in the diode laser system can also be clearly seen in the beat note between the diode laser and fiber laser as compared to beat note in between fiber lasers. Figure 6.5 below shows the RF spectrum of the beat note frequency when both the CW laser locking systems are locked. The beat note between the diode laser and fiber laser, shown in the black curve, is much wider, FWHM~1.3 MHz, than that of the beat note between the fiber lasers, FWHM~200 kHz. We can also see considerable high-frequency noise in the beat note between the diode laser and the fiber laser.

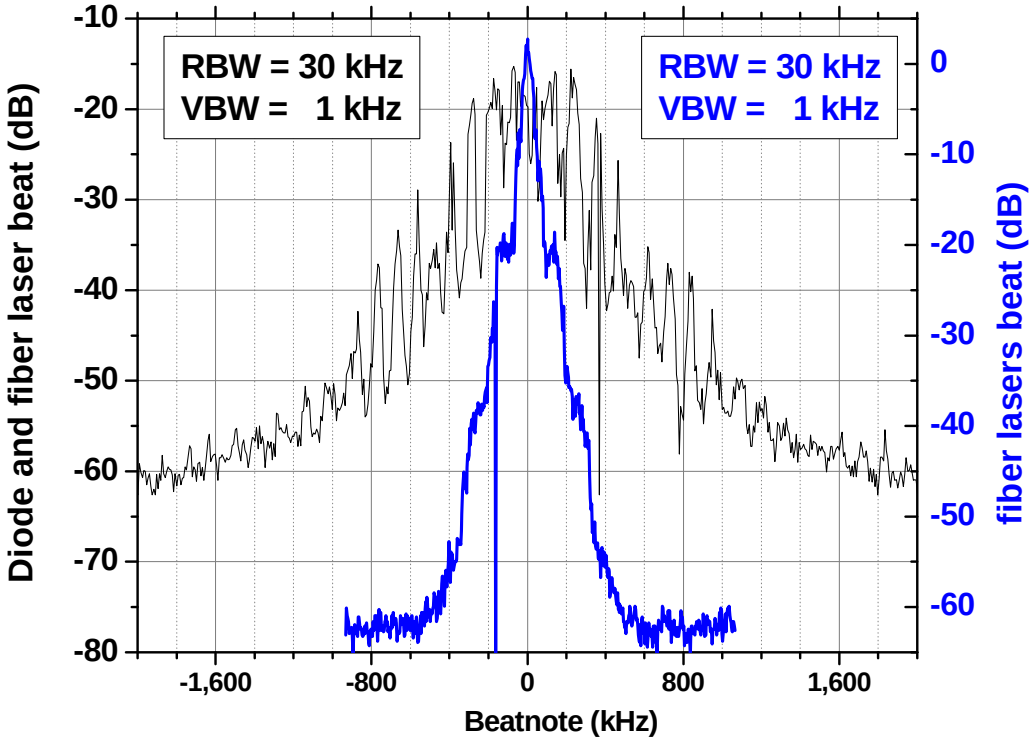

Figure 6.5. RF spectrum of beat note signal with AOM subtracted. Black trace is the beat note between the diode laser locking system and the PM fiber laser locking system. The blue trace is the beat note between the non-PM fiber laser locking systems and the PM fiber laser locking system. The width of the beat note in the former case is much wider, showing the overall noise in the diode laser system. We can also see considerable high-frequency noise in the beat note between the diode laser and fiber laser.

Fractional stabilities are calculated by dividing the Allan deviation of the beat note frequency by the optical frequency of the transition, and the best (average) value obtained for 100 ms gate time is 6.1×10^{-12} (2.3×10^{-11}). There are various factors which cause the beat note to drift and become unstable. We have observed changes in beat note frequency due to temperature, vibration, and polarization and several other environmental perturbation factors. Vibration of the kagome fiber as well as vacuum chamber can have huge effects and may bring the systems out of locking. Our next plan is to make the out-of- loop measurement of the stability of the beat note by making the heterodyne beat between these locked CW fiber lasers with the phase stabilized frequency comb. These are discussed in the next Chapter.

CHAPTER 7 - Absolute frequency measurement: beating comb with CW laser

The simplification, high degree of reliability and precision of frequency combs from mode-locked lasers greatly facilitates optical frequency measurements [2, 144-148]. These combs have become extremely powerful tools for optical frequency metrology [68]. Ti:sapphire lasers broadened in microstructured fiber have been employed to get such precision and reliability. The measured frequencies have been predominantly in the range of 500 nm-1000 nm although this range has been extended to the near infrared spectral region to cover acetylene lines at 1.5 μm using fiber lasers as well as a chirped mirror based Cr:forsterite laser [90]. Here we used a prism-based Cr:forsterite comb as a reference "ruler" to make absolute frequency measurements of molecular lines of acetylene. We measure and characterize the absolute frequency of molecular lines of acetylene inside a hollow core optical fiber to develop a portable frequency reference in the telecommunication band.

7.1. Introduciton

In order to use a frequency comb in metrology, it must be locked to a stable frequency reference. There are several standard references available in RF domain, in microwave domain and in optical domain. Atomic oscillator such as Cesium and Rubidium are the reference standard in RF domain. The cesium transition at 9,192,631,770 Hz serves as the definition of the second and is realized by the US primary standard (NIST-F1). Hydrogen masers use the 1,420,405,752 Hz transition in hydrogen as a reference in microwave domain. Similarly, there are some ions and elements which can serve as a frequency references in the optical domain. Optical atomic standards offer an improvement over their RF counterparts by six orders of magnitude. This is due to much higher optical oscillation frequencies ($\nu_{optical} / \nu_{rf} \approx 10^6$). For example, the neutral calcium standard with an optical transition at 455,986,240,494,158 Hz has demonstrated fractional frequency stability of 1 part in 10^{16} in 1 s. Optical standards based on trapped ions and cold atoms are a promising medium to get better stability [1, 3, 67, 79] . Most of these tests were performed using microwave optical standards with very low phase noise which were subsequently compared in the optical domain. Referencing the femtosecond laser frequency

comb to an optical standard can provide improved stability by allowing shorter averaging time. Recently Long-Sheng Ma *et al* use an optical standard to reference two femtosecond laser frequency combs; the relative uncertainty was measured to be ~$8x10^{-20}$ [149].

These microwave and optical standards are not readily available and they are limited to very few laboratories. Moreover, our goal is to develop fiber-based portable frequency reference devices that are better than what is available right now in the telecommunications band and not to measure the highest precision. We use a GPS disciplined rubidium oscillator as our reference frequency for the our comb [149]. Rubidium oscillators are less expensive, widely available and offer good shot term frequency stability of $5x10^{-11}$ in 1s. For measurements beyond 10s these Rubidium oscillators are better than quartz oscillators found in most of the frequency synthesizers or counters. However, improved stability is realized when GPS receivers are used to steer the Rb local oscillator with accuracy derived from satellite-based Cs clocks. Basically we bought what is called GPS timing receiver which is a commercial unit with a low phase-noise Rb local oscillator. These commercial GPS timing receivers can achieve a typical frequency stability of 10^{-13} when averaged over a week. But these GPS oscillators vary day by day if we count frequency for less than a day due to various factors such as number of satellites in view, GPS signal strength, the time of the day, atmospheric fluctuation, solar activity etc. Others have achieved stability as precise as 10^{-15}, by using a common-view technique [150]. In this common view technique, two GPS receivers are kept some distance apart to observe the same satellite at the same time. All the measurement are similar as a single GPS timing receiver except they make some additional steps to subtract the data point by point after each observation is finished.

Near-IR frequency standards are quite important from a metrological point of view since this region lies somewhere intermediate between the mid-IR and the visible and bridges the gap between them. The near-IR wavelength region is most preferable in telecommunication due to extremely low dispersion and low loss in silica fibers at those wavelengths. Most of the components and a variety of laser sources are available in this region at relatively low cost. It is anticipated that this spectral region will play a continuing important role in optical technology and science. But the 1.5 μm wavelength region corresponds to energies that are below most of the electronic transitions in atoms and molecules and above the fundamental vibration of the molecules. So we need to explore wavelength references based on overtone transitions. Acetylene provides a series of overtone transitions in this range from 1510 nm to 1540 nm which

are also relatively immune to external perturbations and have a comparatively large absorption strength. Therefore acetylene is recognized as a standard reference for the near-IR region [151, 152].

Acetylene has been used as a frequency reference with increasingly precise measurement. After the first demonstration of saturated absorption spectra in acetylene, reported by de Labachelerie *et al* in 1994 [100], quite a number of research group throughout the world used Fabry-Perot cavites for power and effective path length enhancement, and observed the saturated absorption resonance in acetylene [101, 102, 153, 154]. After the invention of femtosecond frequency comb metrology, direct measurement of these transition frequencies were possible with uncertainties of the order of kHz level and instabilities of 10^{-12} at 1s averaging time extending below to 10^{-13} for longer wavelengths [105, 155-161]. Many of these measurement are done using a Ti:sapphire frequency comb and frequency doubled radiation at ~770 nm. But the use of a frequency-doubled source poses a problem due to high power requirement and availability of bandwidth requirement on the doubling crystal to cover the entire C_2H_2 spectrum from 1510 to 1540 nm. Recently, mode-locked erbium doped fiber lasers have attracted significant attention in frequency metrology of acetylene lines [158, 162, 163]. Fiber combs are a highly robust and compact laser light source and their comb spans far enough to measure the entire near-IR spectrum. But these fibers laser are much noisier as compare to solid state lasers. There are currently limitations on the repetition rates they have achieved so far because of the need to exactly manage the fiber lengths necessary for mode-locked operation. Madej *et al* in 2006 used a Cr:YAG laser frequency comb to measure absolute frequencies from 1511 nm to 1545 nm of the $\nu_1+\nu_3$ band of acetylene with uncertainties as low as 2 kHz (~10^{-11}) [156]. Another promising material that offers the appropriate spectral coverage is the gain medium Cr:forsterite (Cr^{+4}:Mg_2SiO_4) which readily covers the 1150-1350 nm region and is capable of producing 14 fs pulses [17] at relatively high output powers. In this Chapter, I would like to talk about the absolute frequency measurement of Doppler free acetylene lines using a Cr:forsterite laser inside the hollow core fiber. This is the first measurement to develop and characterize the portable frequency standard inside a hollow core fiber using a femtosecond frequency comb. This measurement has lot of practical and commercial implication due to extremely low loss and portability of photonic band gap hollow core fibers.

7.2. Principle and experimental setup

A frequency comb has two free parameters: laser repetition frequency (f_r) and the carrier envelope offset frequency (f_0). Any tooth of the comb can be expressed in terms of these two parameters with the simple mathematical expression,

$$f_n = Nf_r \pm f_0 \tag{7.1}$$

Here N refers to the integer mode index which connects the RF-domain to the optical domain. In general, we control f_r by locking the repetition rate of the mode-locked comb laser to a low phase noise laboratory synthesizer by controlling the laser cavity length with a piezoelectric crystal. The synthesizer is referenced by a 10 MHz signal supplied by the GPS timing receiver. To control f_0, we phase lock the frequency f_0 to a known frequency from a laboratory synthesizer by using the pump power to servo f_0. Controlling these two parameters in the RF-domain is sufficient to precisely know every tooth of the comb.

The output from the stabilized comb is then filtered using a ~1532 nm bandpass filter (FWHM ~ 10 nm). The band pass filter is made for 1550 nm of central wavelength but we angle tune it to reach to 1532 nm which can further increase loss by ~3 dB. We also use a combination of a half wave plate and a quarter wave plate to optimize the polarization of the supercontinuum source at ~1532 nm as shown in Fig. 7.1 below. This gives us a heterodyne beat note f_b which is then bandpass filtered, and amplified approximately to -15 dBm before it is monitored by the counter.

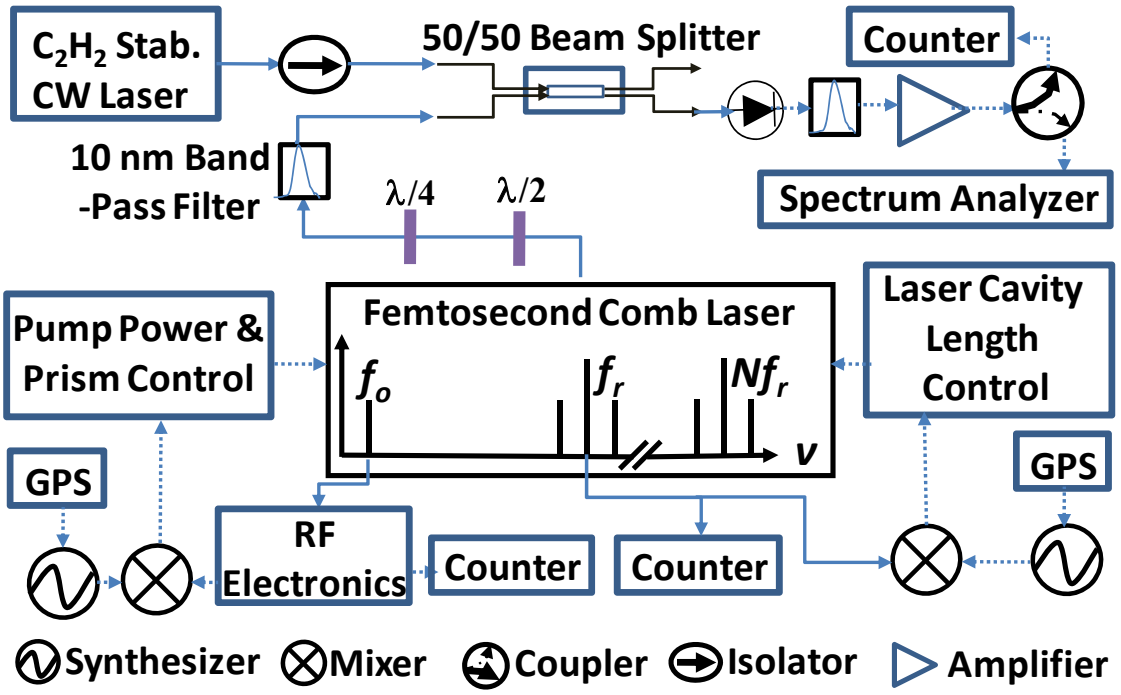

Figure 7.1. Absolute frequency measurement system diagram. Both the f_0 and f_r are referenced to the GPS disciplined Rb clock.

All of the counters and synthesizers shown in the Figure 7.1 are referenced to the GPS disciplined Rb clock. Our heterodyne beat note, f_b, has 25 dB of SNR centered at a frequency of ~30 MHz with a FWHM of 400 kHz.

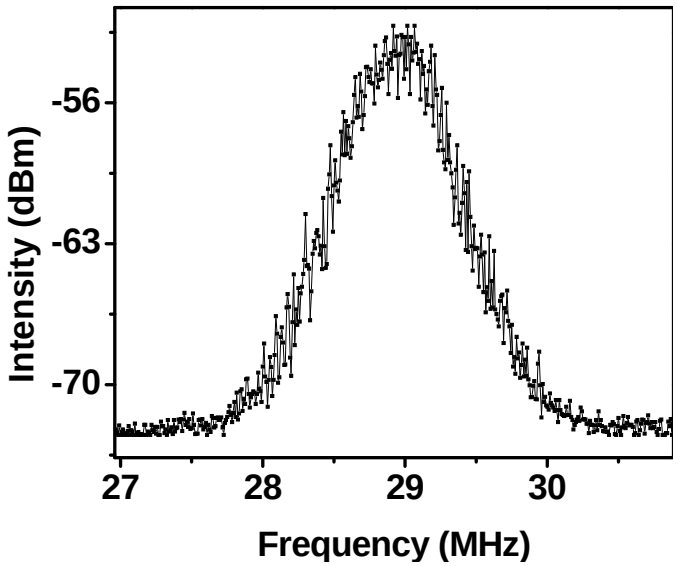

Figure 7.2. Beat note, f_b, in between Cr:f frequency comb and CW fiber laser locked to the molecular transition of acetylene.

The frequency of the acetylene stabilized laser can then be written as,

$$f_n = Nf_r \pm f_0 \pm f_b \tag{7.2}$$

Where the sign of the beat note gives the idea about which side of the n^{th} comb line our unknown frequency lies. The positive sign of the f_b indicated that the C_2H_2-stabilized laser has the frequency higher than the frequency of the comb mode that is involved. The correct sign for the frequencies can also be figured out by slightly changing the respective synthesizer frequencies for f_r and for f_0 and noting the change in f_b. The only quantity not directly measured in this series of measurements is N, which can be deduced in two different approaches: with prior knowledge of the unknown frequency with an uncertainty less than f_r or without prior knowledge of the frequency to be measured as mentioned in reference[164] which will be discussed later in this Chapter.

7.3. Frequency measurements

In Chapter 6, we talked about characterization of the accuracy of the gas-filled PBGF cells by locking a CW fiber laser to the acetylene absorption feature. Now we would like to measure the absolute value of that locked CW laser with the help of our Cr:forsterite laser frequency comb. These measurements are made on acetylene inside the 70 μm core kagome fiber.

After ensuring that the Cr:forsterite laser was running in its optimum condition by looking at the count data of both f_0 and f_r, we then count the heterodyne beat between the Cr:forsterite laser and the acetylene-stabilized CW fiber laser. A number of times during each data run, one of the phase lock loops of the Cr:forsterite laser typically comes out of the lock and we need to manually relock it. This unlock is due to various factors such as thermal drift, pump power fluctuation, temperature of the lab, etc. Most of these data were recorded and removed from the raw data. The time series measurement of the data of f_0, f_r, and f_b is shown in the Fig. 7.3 below. Each of these data sets has been recorded for different gate time of the counter to characterize the stability of the comb and the heterodyne beat note by calculating the Allan deviation. As I mentioned in Chapter 6, we use an AOM in the saturated absorption setup which may drift during the counting of the heterodyne beat and therefore cause the heterodyne beat to drift. To ensure that we are not limited by the AOM drift, we also count the dc offset of the RF signal driving the AOM. We have found that the AOM drift is negligible as compare to the drift

of the heterodyne beat. So we can simply ignore the effect of the AOM drift on the stability of the heterodyne beat. We also monitor the temperature using a temperature sensor just below the vacuum chamber where gas filled fiber is kept. The temperature sensor continuously monitors the temperature every 15 s and records it. The temperature of the lab throughout the measurement of the count data was fairly constant at 22.9 ^{0}C.

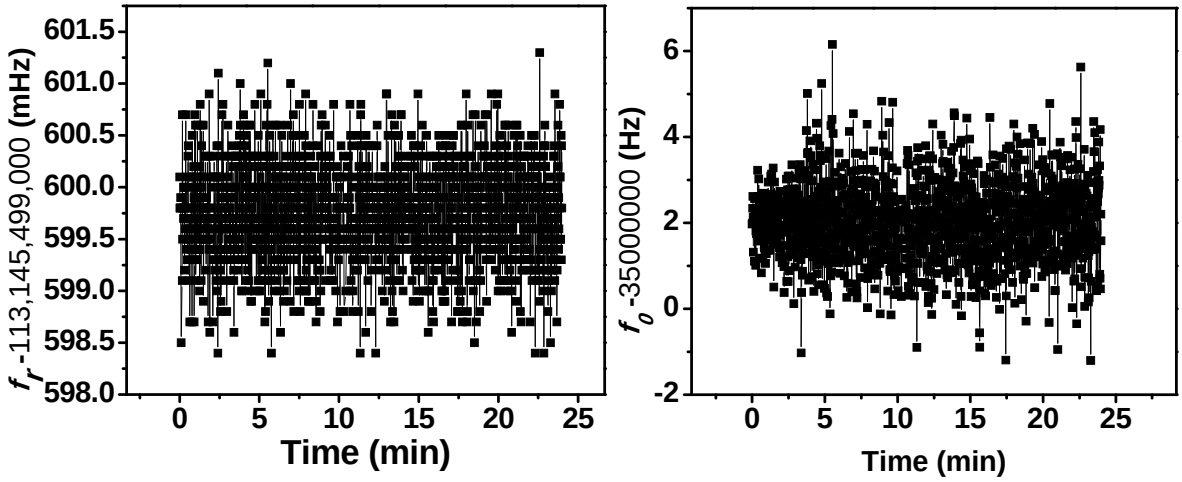

Figure 7.3. Counter frequency measurement of f_r and f_0 with 1-s gate time. Both data sets are plotted by subtracting off a particular frequency value, as indicated in the Y-axis label.

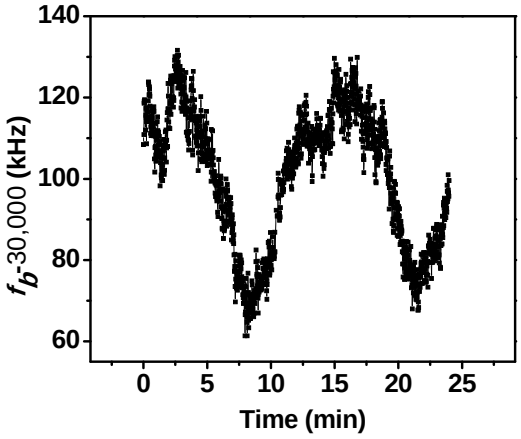

Figure 7.4. Counter frequency measurement of f_b at 1s gate time. We can clearly see the periodic fluctuation of the beat note over a ~15 minute time period. This may be due to temperature fluctuations in a nearby air-conditioning unit, which has a cycling time of ~ 10 minutes; heterodyne beat count exhibits fluctuations between the comb and CW-laser locked to P(13) line of $^{12}C_2H_2$ on the scale of 10 min also. (However, a temperature sensor near by the hollow core fiber did not record a change in temperature during this data set within the resolution of 0.1^{0}C.)

Each of the measurements of f_r, f_0 and f_b consists of count data from three different counters that were monitored and recorded in a computer. We repetitively gate the counter using a different gate time of 10 ms, 100 ms, 500 ms, 1000 ms and 10000 ms in each run to measure long term and short term stability of f_r, f_0 and f_b. The repetition rate data were limited by noise in the counters to approximately $\Delta f/f \approx 5\times10^{-11}$ or 50 mHz at 1-s gate time. We then calculate the Allan deviation to measure the stability of f_r, f_0 and f_b. Figure 7.5 below shows the fractional Allan deviation of the time series measurement of f_r, f_0 and f_b weighted by their respective contributions to stability in optical domain. To calculate the Fractional stability of f_r in optical domain, we multiply uncertainty of f_r by N and then divide by f_x (~195 THz). For f_0 we simply divide the uncertainty of f_0 by N and then divide by f_x (~195 THz).

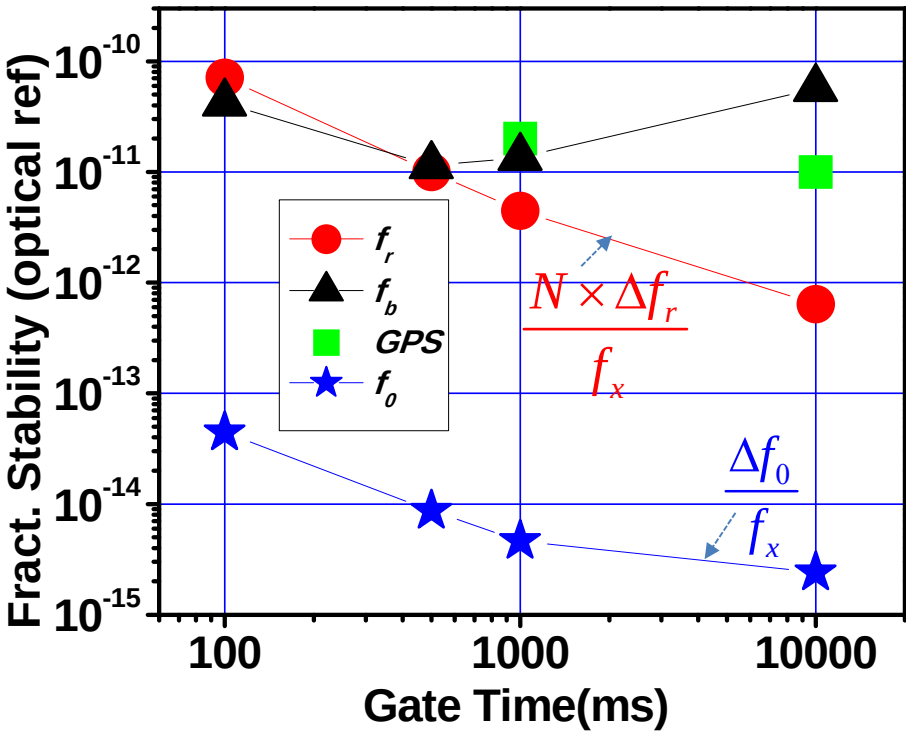

Figure 7.5. Fractional stability of f_0 (star) and f_r (circle) for different gate times in the optical domain. Here f_r is counter- limited. Fractional stability of the beat note (triangle) between the comb and the acetylene stabilized CW laser clearly shows that the short term stability of the locked CW laser is limited by stability of the GPS reference. The GPS/Rb frequency stability (square) is expected to be ~ 2×10^{-11}@ 10-s gate time.

Extensive tests have been done to show the stability of the femtosecond comb to measure the optical frequencies to the ~ 5×10^{-11} level at 1-s gate time when referencing our comb to the GPS disciplined rubidium clock. But this measurement of comb stability is limited by the noise of the counter. The data for f_b averages down to an uncertainty very close or better than GPS limit at 1-s gate time. The value of GPS stability of ~ 2×10^{-11} levels at 1-s gate time is provided by the manufacture specification sheet and is worst case scenario. To measure f_b stability better than ~ 10^{-11} level, measurement duration must be significantly longer, more than 12 hours at larger than 100 s gate time. This seems to be impossible in our current Cr:forsterite laser system providing its inherent complexities in operation with 4 different servo systems, material properties, temperature fluctuation, coupling between f_0 and f_r servo etc. Beat note between comb and CW laser locked to the molecular transition clearly reflects the short term stability of the P13 acetylene line is within 10's of kHz at 1.531μm wavelength. In the long run, lock points of the CW laser locked to the P13 line changes and makes beat note to drift.

7.4. Absolute mode number, N and frequency measurement

There are two different ways to determine the absolute mode number in order to measure the unknown frequency [164]. First is with prior knowledge of the frequency to be determined and second is without prior knowledge of the frequency. In the first case, we need to know the frequency to be measured within an uncertainty that is small relative to the frequency spacing between comb components. For a system of low repetition rate, this can corresponds to a relative accuracy of a few parts in 10^8. However in a large range of applications using diode lasers, solid state lasers and other type of lasers it may be difficult to know the frequency to be determined to that precision. This is not a problem in the case of power build up cavities since acetylene lines have been measured within ~2 kHz. However, to be extra careful and in case the fiber spectroscopy technique caused a large shift (~100 MHz), we employed alternate techniques that did not assume any prior knowledge of the frequency to be measured.

An alternative way of determining the absolute mode number was proposed by Long-Sheng Ma *et al* in 2003[164]. This method does not require the prior knowledge of the unknown frequency. The main idea behind this measurement is to beat the unknown radiation successively using different repetition rates of the femtosecond laser with two or more comb components of

the known difference in mode order. As we discussed, the unknown frequency, f_x to be measured using the frequency comb can be written as,

$$f_x = Nf_r \pm |f_0| \pm |f_b| \tag{7.3}$$

and the sign of the values for of f_0 and f_b are deduced as described later. Let us now change the repetition rate of the laser by a small number, m by carefully counting the comb components. The measured frequency can then be expressed as,

$$f_x = (N \pm m) f_r' \pm |f_0'| \pm |f_b'| \tag{7.4}$$

where all frequencies are now referred as $(N \pm m)^{th}$ components of the comb. Here N and m are both integers. By smoothly changing the repetition rate by changing the voltage on the PZT attached to the end mirror, the change in mode order, m can be controlled and known. The value of m can then be chosen while the repetition rate of the comb is phase locked to the RF synthesizer. Thus, very precise values of the f_b' and f_b are obtained by counting these beats over an appropriate integration time. Experimentally, we change the synthesizer frequency which is phase locked to the repetition rate of the laser while monitoring and counting the beat note, f_b on the screen of an RF spectrum analyzer. As the mode order is changed by m, the repetition rate is roughly changed by m×65 Hz. Figure 7.6 below shows one such measurement where we change the synthesizer frequency by ~600 Hz to change N by 10 in order to count m=10; we paused each time f_b came back to the same value. As we changed f_r, we watched f_b increase until $f_r/2$, then decrease to zero, then increase to starting value. At this point we paused, so the number of steps shown in Fig. 7.6 indicate m, the change in the number of comb teeth.

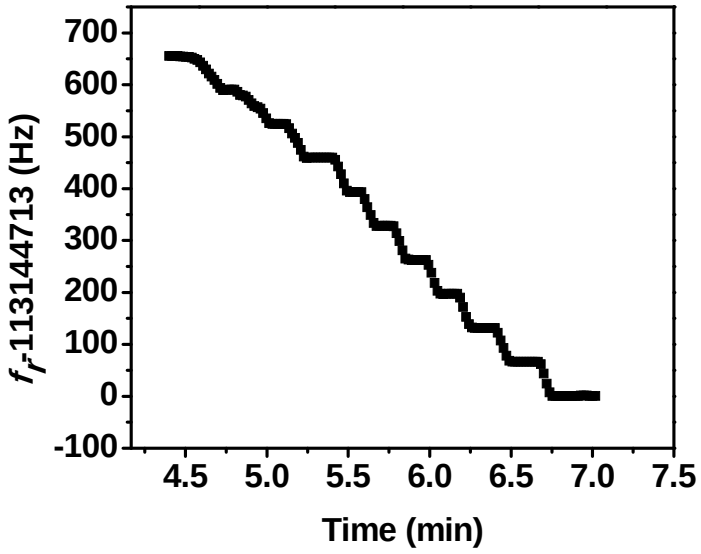

Figure 7.6. Counted repetition frequency while changing the synthesizer frequency to decrease or increase comb tooth by 10. Every step in ladder corresponds to change in m by 1 and total number of steps equals m. We can see change in N by 10. But we cannot change m by more than 10 steps before the laser goes out of lock.

As I mentioned in section 7.2, the correct sign of the beat note term gives the idea if the frequency of the acetylene stabilized laser is higher or lower than the frequency of the comb mode involved. We can figure out the sign by slightly changing the respective synthesizer frequencies and note the change in beat note. Figure 7.7 below shows such a measurement, in which we can clearly see that f_b follows f_r in the same direction whereas f_b follows f_0 in opposite direction. Since f_x is constant, we can easily figure out the correct sign of both the f_0 and f_b. For example, in the case shown in Fig. 7.7 below

$$f_x = Nf_r - |f_0| - |f_b| \quad \text{where, } f_0 = -|f_0| \quad \text{and } f_b = -|f_b|$$

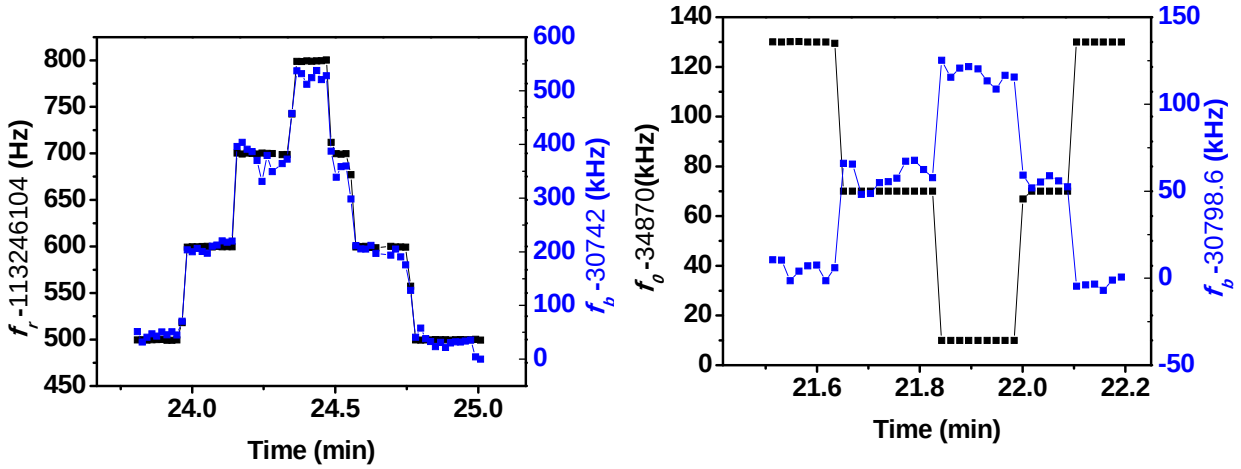

Figure 7.7. Determination of correct sign for f_0 and f_b. f_b follows change in f_r in the same direction whereas f_b follows change in f_0 in opposite direction.

Combining Eq. 7.3 and 7.4, we can easily get N,

$$N = \frac{mf_r^{'} + f_0^{'} - f_0 + f_b^{'} - f_b}{f_r - f_r^{'}} \tag{7.5}$$

Here we have taken all positive sign in Eq. 7.3 and 7.4. Sign of the f_r, f_0 and f_b could be positive or negative depending upon the behavior of f_r vs. f_b and f_0 vs. f_b as discussed above. Equation 7.5 gives the experimental value of the integer N. But N can be determined to a limited precision due to the instability of the laser frequency; the statistical fluctuation of the frequency measurement can be reduced by using a longer measurement time. Since there is uncertainty in the measurement of f_r, f_0 and f_b, the error propagates to the integer N. One of the easiest ways to figure out a rough estimate of error in N is by considering error in f_r, f_0 and f_b as independent of each other. In such case, we can use the expression for error propagation as,

$$\frac{(\delta N)^2}{N^2} = \frac{[\delta(mf_r^{'} + f_0^{'} - f_0 + f_b^{'} - f_b)]^2}{(mf_r^{'} + f_0^{'} - f_0 + f_b^{'} - f_b)^2} + \frac{[\delta(f_r - f_r^{'})]^2}{(f_r - f_r^{'})^2} \tag{7.6}$$

Where, δN is uncertainty in measurement of N. Equation 7.6 can be simplified for δN ,

$$\delta N = \sqrt{\frac{m^2(\delta f_r^{'})^2 + (\delta f_0^{'})^2 + (\delta f_0)^2 + (\delta f_b^{'})^2 + (\delta f_b)^2}{(mf_r^{'} + f_0^{'} - f_0 + f_b^{'} - f_b)^2} + \frac{(\delta f_r)^2 + (\delta f_r^{'})^2}{(f_r - f_r^{'})^2}} \times \frac{mf_r^{'} + f_0^{'} - f_0 + f_b^{'} - f_b}{(f_r - f_r^{'})} \tag{7.7}$$

We can, in fact, approximate Eq. 7.7 in a very simple form as,

$$\delta N = N \frac{2\delta f_b}{m f_r} \tag{7.8}$$

Where, we have considered $mf_r > f_b$, $\delta f_r \ll \delta f_b$, $(\delta f_r)^2 \ll 1$, and $f_0 \approx f_0^{'}$

For the absolute frequency measurement to be useful, $\delta N \leq 1$. To fulfill this criterion beat note, f_b should be less than or equal to $\frac{mf_r}{2N}$,

$$\Rightarrow \delta f_b \leq \frac{mf_r}{2N} \approx 1kHz$$

This shows that we should be able to count f_b within kHz or alternatively, we need to increase step size *m* up to 2000 without losing the phase locking. Both of these conditions seem to be impossible to fulfill in our system since our f_b changes by more than 40 kHz and we cannot count *m* by more than 10. Even in the case when frequency comb is very stable, if acetylene stabilized laser drifts in time, we cannot fulfill the criteria $\delta N \leq 1$. So in the case of measuring N for less stable laser such as ours, single step in *m* does not provide an unambiguous identification of N. The method needs to be repeated for additional *m*'s by choosing a significantly different repetition rate of the cavity. To change the laser cavity length by significant amount, we use the micrometer attached to the end mirror inside the cavity. For each different cavity length, we count *m* by using the synthesizer frequency phase locked to f_r. For each *m*, there exists only one closest reappearing mode order that can be accepted as a possible candidate for absolute mode number. This is also illustrated in Table 7.1. The Table below shows that, for each *m*, there exists only one reappearing mode order, with small values of δ. The first two columns of measurements shown in Table 7.1 were taken 10 days before the measurement shown in last two columns in the same table.

Table 7.1. Compilation of experimentally determined absolute frequency measurement for different mode number N. Calculation gives a unique number in either column, listed in bold type, with minimum frequency difference in each of the first two column or last two column separated by double line. The mode number presented in the table corresponds to the absolute frequency measurement shown in bold type. The f_r frequency shown is the upper value in the step counting. The first two columns of measurement and the last two columns of measurement are taken in ~ 10 days of difference in time

f_r (in MHz) = 113.2467594997 $m = 10$ $N = 1727034$	f_r (in MHz) = 113.0296957997 $m = 10$ $N = 1730350$		f_r (in MHz) = 113.0375351998 $m = 7$ $N = 1730237$	f_r (in MHz) = 113.1922849996 $m = 7$ $N = 1727871$
f_x (P13 of $^{12}C_2H_2$) (Hz)	f_x (P13 of $^{12}C_2H_2$) (Hz)		f_x (P13 of $^{12}C_2H_2$) (Hz)	f_x (P13 of $^{12}C_2H_2$) (Hz)
……	……		……	……
195580486541263	195580374395285		195580035030485	195580599800239
195580599788023	195580487424981		195580148067563	195580712992065
195580713034782	195580600454676		195580261104641	195580826183892
195580826281542	195580713484372		195580374141719	**195580939375718**
195580939528301	195580826514068		195580487178797	195581052567544
195581052775061	**195580939543764**		195580600215874	195581165759371
195581166021820	195581052573460		195580713252952	1 95581278951197
195581279268580	195581165603155		195580826290030	195581392143024
195581392515339	195581278632851		**195580939327108**	195581505334850
195581505762099	195581391662547		195581052364186	195581618526676
195581619008858	195581504692243		195581165401263	195581731718503
……	……		……	……

We use an AOM to shift the frequency of the probe by ½ of the AOM frequency to minimize the interference between the pump and probe. Fig. 7.8 below shows our AOM frequency which is at ~80 MHz. Therefore, we need to add ½ of the AOM frequency (39,999,427 Hz) to the frequency of the P13 line as shown in Table 7.1 to get the absolute

frequency measurement. The drift of the AOM is negligible as compared to the uncertainty of our beat frequency measurement.

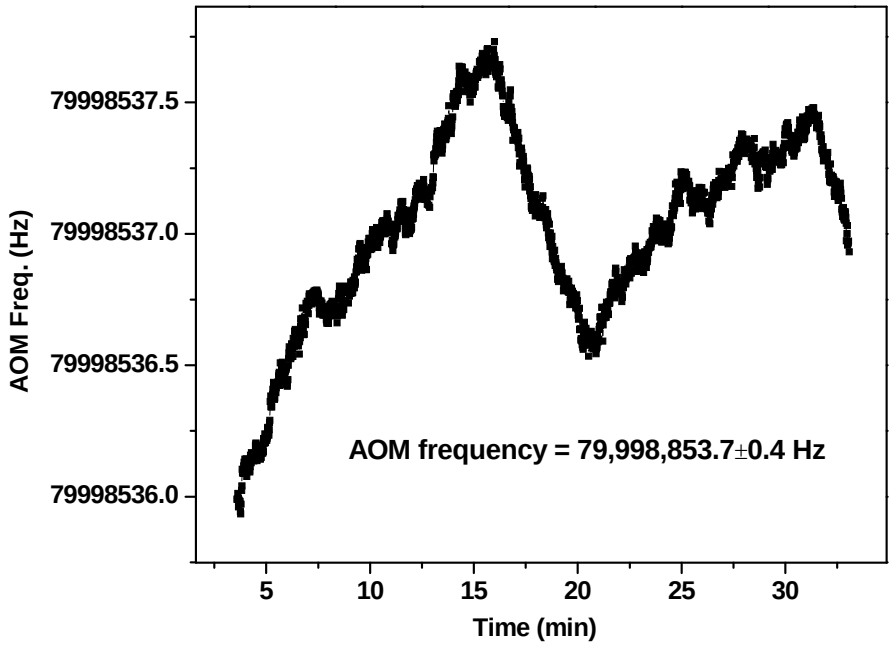

Figure 7.8. AOM frequency measurement

Besides the small drift due to the AOM, there are several other factors such as pressure and power shift which cause the shift of the molecular lines of the acetylene. We have yet to perform these measurements inside the hollow optical fiber. But there are some groups who have already measured these shifts inside the power build up cavity and inside the gas cell for different molecular lines of acetylene [6, 99, 109]. Some of these measurements of pressure and power shifts are tabulated below.

Table 7.2. Pressure and Power shift measuremets

Molecule	lines	Line Center Wavelength (nm)	Pressure Shift (kHz/Torr)	Power Shift (Hz/mW)	Reference
$^{12}C_2H_2$ (In Glass Cell)	P13	1532.83	-270 (±30)		[99]
$^{13}C_2H_2$ (In Fabry-Perot Cavity)	P16	1542.38	-230 (±20)	-11.4 (0.6)	[109]

The measurements shown in Table 7.2 show that pressure and power shift are not major contributing factors to the uncertainty of our measurements inside the hollow core fiber, where the pressure is less than 150 mT, which corresponds to a pressure shift of 40 kHz and power is ~100 mW, which corresponds to a power shift of ~1 kHz.

After we added ½ of the AOM frequency to the measured frequency, we took the mean and standard deviation of these four different measurements. These measurements have resulted in absolute frequency of CW laser locked to the P13 line of acetylene inside 68 μm hollow core Kagome fiber to be 195.580,979,427 THz. Two measurements differed by ~10 kHz in Aug 8 measurement and ~30 kHz in Sept 8 measurement which may indicate a different drift rate of the C_2H_2 stabilization on the two days. Each of these measurements lasts for 30 minute or so. However if we take the standard deviation of these 4 data shown in bold face letter as shown in Table 7.1, the uncertainty of the measurement is found to be ~110 kHz. But for these small data sets, the standard deviation is not a completely reliable way to calculate uncertainty. We can clearly see a difference of ~200 kHz in two different measurements taken at two different times as shown in Table. 7.1 above. So, reproducibility of the measurement was the biggest concern for us since we have seen day to day drift in the absolute frequency measurement.

To understand the source of this drift, we beat the non-PM fiber laser locking system to the PM fiber laser locking system and measured the counted beat note vs. time. At the same time, we also made a heterodyne beat note between the PM-fiber laser locking system and the Cr:forsterite comb and counted the beat note between them. These measurements are shown in Fig. 7.9a below. If we subtract these time series measurements of the two beat notes we can get a very flat signal as shown in Fig. 7.9b. The remaining small fluctuations we see seem to be due to temperature fluctuations inside the lab as shown in the red line in Fig. 7.9b.

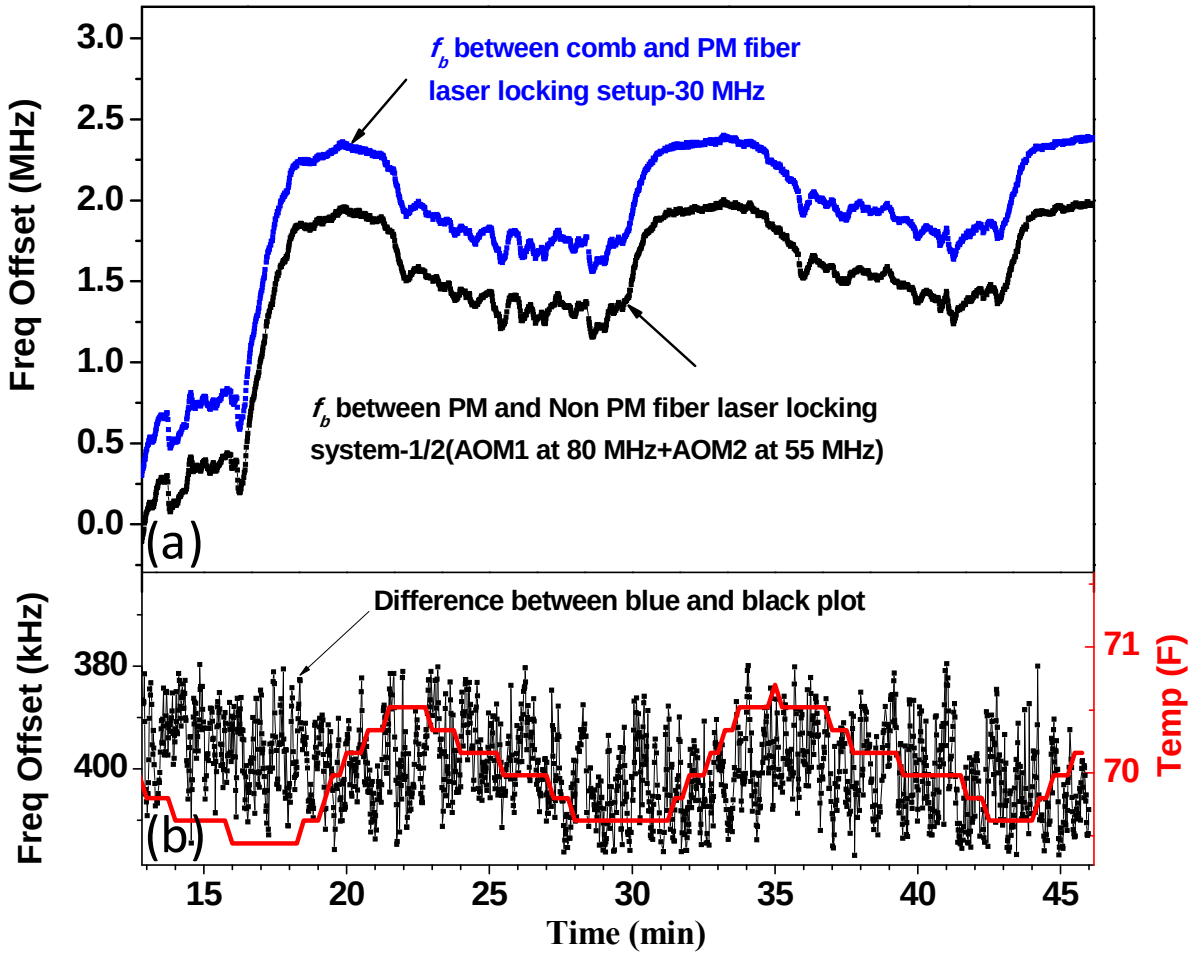

Figure 7.9. (a) Time series measurement data of the beat note between the non-PM and PM fiber laser locking setup (black) and the heterodyne beat between the PM-fiber laser locking system and the Cr:forsterite comb (blue). (b) Difference between blue and black plot shown in (a). Red line is the temperature fluctuation as measured near the PM fiber locking setup. (Note: time axis is same for both the graph a and b

We have recently figured out that there is a large drift caused by the EOM in our "PM fiber laser locking system" that may have led to this difference. (Note: Difference between PM and Non-PM locking system is explained in detail in Chapter 6.). The EOM distributes the power to CW laser light to create sidebands spaced by the modulation frequency around the original frequency of light. Due to the poor quality of the EOM in our PM system, it distributes power in the sidebands unevenly and randomly and gives rise to the imbalance in the wings of the derivative signal and hence contributes a large error in our measurement. This imbalance and drift most likely led to the large frequency offset of our measurement.

A signature of the drift already appeared in the error signal before we carefully made this beat note measurement between the two different systems, so while counting the measurement we were able to change the probe polarization to minimize the effects. Therefore the actual uncertainty of the measurement is difficult to assess without taking additional measurements. Because that drift was not well controlled at the time of measurement, we make a conservative estimate of the error bar to be between 100 kHz and 1 MHz. Our recent measurement of the absolute frequency of the acetylene line in the non-PM setup shows a very promising result in terms of the reproducibility of the measurement.

In fact, several groups have measured the acetylene lines inside a glass cell and power build up cavity [6, 99, 155, 156, 165]. One of the accurate and precise measurements of the P13 line of $^{12}C_2H_2$ was made by Mandej *et al* inside a power build up cavity using a Cr:YAG laser based frequency comb [156]. We compare our measured value of 195580979370±2 kHz for P13 line measured in Ref. [156].

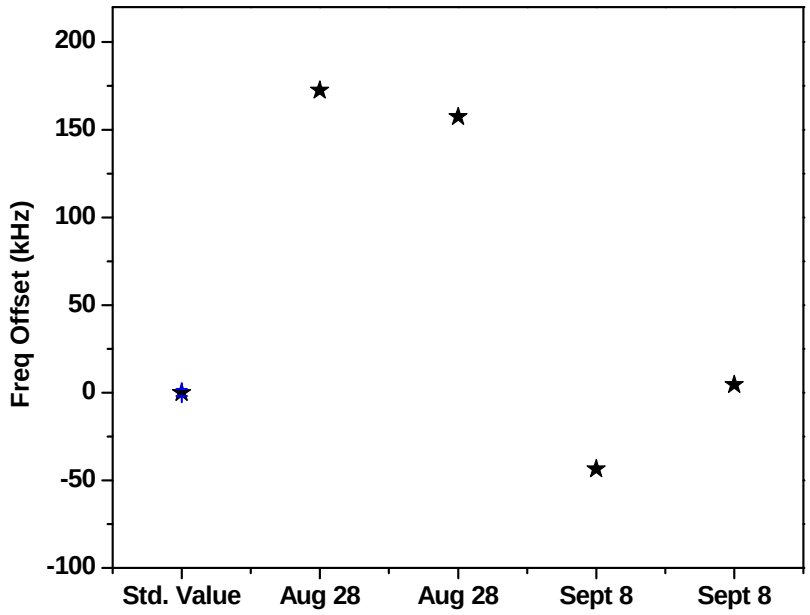

Figure 7.10. Absolute frequency measurement of P13 line of $^{12}C_2H_2$ performed inside hollow core Kagome fiber in Aug 28 and Sept 8. Frequency offset in Y-axis is difference in frequency between our measured frequency and frequency of 195,580,979,370 kHz measured by Mandej *et al* for P13 line of $^{12}C_2H_2$ inside power build up cavity as mentioned in Ref [156].

To conclude our result, we have measured the absolute frequency of the P13 line of acetylene inside the 68 μm hollow core Kagome fiber to be 195,580,939,400 kHz with the

estimated uncertainty somewhere in between 100 kHz and 1 MHz. The uncertainty is derived from the standard deviation of the 4 different measurements taken in two different days which is ~ 100 kHz and estimated uncertainty due to the EOM drifts of ~ 1MHz. We are hoping that within very short period of time, we can track down uncertainty below 10 kHz.

CHAPTER 8 - Conclusion and future direction

While the science of frequency metrology has been transformed, optical fiber technology has simultaneously been revolutionized; we have demonstrated potential to use gas-filled hollow core fibers as an extremely portable frequency reference device in the near-IR region. We are the first group to investigate saturation spectroscopy of acetylene inside photonic band gap fibers. We have recently used larger core kagome fiber to demonstrate much narrower sub-Doppler features of around 10-15 MHz (FWHM). We have characterized saturated absorption features inside these hollow core fibers in terms of pressure, power and fiber geometry. Larger core kagome fiber also gives much higher signal slope of ~5-10/GHz of these narrow sub-Doppler features which is a factor of 3 to 5 larger than in PBG fibers. Higher signal slopes are better since they give higher signal-to-noise ratios to lock the CW laser to these narrow features.

To develop a portable frequency reference we need to get rid of the vacuum chamber to perform pump-probe spectroscopy inside these hollow optical fibers. This is possible if we can seal these hollow fibers. Many applications of PBGF require the fabrication of a PBGF cell, in which a length of PGBF is filled with a gas or liquid and spliced to solid-core single-mode fiber (SMF) on each end. We have developed a repeatable, robust, low-loss and innovative splicing technique to splice a hollow-core PBGF to SMF using a commercial electric-arc splicer. The most unique feature is the non-reciprocity of the splice loss: the splice loss as measured from the SMF to PBGF is different from that measured in the opposite direction from the PBGF to SMF. In the 20 μm HC19-1550-01 fiber, splice loss from SMF to PBGF varies from 0.3 dB to 0.5 dB whereas splice loss from PBGF to SMF is more than 2 dB. The splice loss non-reciprocity is less prominent in 10.9 μm PBGF, because there are fewer modes present.

We have utilized a technique called frequency modulation (FM) spectroscopy for frequency stabilization of a CW laser locked to a molecular transition. We used this technique to peak-lock both the extended cavity diode laser and fiber laser to the narrow sub-Doppler features. The signal to noise of the lock signal in the diode laser is found to be a factor of 3 smaller than that of the fiber laser. We also beat two of the CW fiber laser locked to the narrow sub-Doppler feature in two identical setups and figure out the short term stability of $4\pm2\times10^{-11}$ at 100 ms gate time at a beat note frequency of 68 MHz.

Since the frequencies of these molecular transitions lie in the near-IR region, we have developed and phase stabilized a prism-based Cr:forsterite laser frequency comb to make an absolute frequency measurement of the molecular lines of acetylene. The stabilized Cr:forsterite frequency comb provides a dense grid of reference frequencies which spans a substantial part of the near-IR region from 1000 nm to 2200 nm. We used a GPS-disciplined rubidium oscillator as our frequency reference to our comb. Rubidium oscillators are less expensive, widely available and also offer good short term fractional frequency stability of $5x10^{-11}$. These commercial GPS timing receivers can achieve a typical frequency stability of 10^{-13} when averaged over a week and a stability of $2x10^{-11}$ at 1s. We used 4 different servos, including a prism servo inside the cavity to stabilize the Cr:forsterite laser and successfully managed to stabilize the comb for 2-3 hours to measure the optical frequencies to the ~ 5×10^{-11} level at a 1-s gate time. But this measurement of comb stability is limited by the noise of the counter at 50 mHz since our f_r measurement is counter-limited.

Finally, our goal is to measure the absolute frequency of the CW laser locked to the molecular transition. After ensuring the Cr:forsterite laser was running in its optimum condition by looking at count data of both f_0 and f_r, we then counted the heterodyne beat between the Cr:forsterite laser and acetylene stabilized CW fiber laser. The beat note between the comb and CW laser locked to the molecular transition clearly shows that the short term stability of the P13 acetylene line is within 10's of kHz at 1.531 μm of wavelength; the correspondingly frequency stability of the beat note is better than ~ 10^{-11} level. The value of the GPS stability of ~ 2×10^{-11} levels at 1-s gate time is provide by the manufacture specification sheet and is the worst case scenario. To measure the f_b stability to better than the ~ 10^{-11} level, the measurement duration must be significantly longer. This seems to be impossible in our current Cr:forsterite laser system providing its inherent complexities in operation with 4 different servo systems and some drawback of the Cr:forsterite crystal itself such as poor thermal conductivity, and thermal lensing effects. In long run, the lock point of the CW laser locked to the P(13) line changes and makes the beat note to drift. This drift may be due to various factors such as temperature change inside the lab, polarization drift, power change inside the fiber, pressure shift due to leakage in the vacuum chamber, etc.

To summarize the conclusion, the first stage of development of innovative portable frequency references clearly shows at least one or two order of magnitude improvement in short

term stability over the measurement capabilities of commercially available devices. This measurement can have a significant impact on existing technology due to implication of extremely low loss and portability of photonic band gap hollow core fibers.

The future of these frequency references is very promising, even though there are some subtle challenges. We now have phase-stabilized a very compact and highly stable erbium-doped fiber laser to characterize the long term stability of the frequency reference. Significant progress is going on to characterize the shift in the center frequency of the CW laser locked to the molecular transition due to temperature, gas pressures, power, fiber length, laser polarization, and other parameters that may drift during the operation of such a reference. We will further pursue techniques for narrowing the sub-Doppler line, as necessary, once we have exhausted the approach of trying larger fiber core sizes. Furthermore, we have also started investigating the behavior of the Cr:forsterite laser under a variety of perturbations in order to better understand how to effectively phase-stabilize it for longer time. We are also in the process of characterizing noise in different teeth of the comb by beating the Cr:forsterite laser with the fiber laser. This helps us to minimize noise which may give use some idea of how to minimize the width of the carrier envelope offset frequency. Narrower comb teeth are better for frequency metrology since they can give more precision in a measurement. As described earlier, we have the capability of splicing solid core fiber to PBG fiber using an electric arc splicer, and are developing the capability of sealing two fibers together while they are inside the chamber. One more subtle challenge would be to splice larger-core kagome fibers; this is challenging in part because the microstructured cross-sectional area of the large-core kagome fibers is larger than the entire cross-section of standard solid-core SMF fiber.

References

1. Rosenband, T., et al., *Frequency ratio of Al+ and Hg+ single-ion optical clocks; Metrology at the 17th decimal place.* Science, 2008. **319**(5871): p. 1808-1812.
2. Diddams, S.A., et al., *Femtosecond-laser-based optical clockwork with instability <= 6.3 x 10(-16) in 1 s.* Optics Letters, 2002. **27**(1): p. 58-60.
3. Hollberg, L., et al., *Optical frequency standards and measurements.* Ieee Journal of Quantum Electronics, 2001. **37**(12): p. 1502-1513.
4. Ma, L.S., et al., *Frequency uncertainty for optically referenced femtosecond laser frequency combs.* Ieee Journal of Quantum Electronics, 2007. **43**(1): p. 139-146.
5. Gilbert, S.L., et al., *Optical Metrology for Wavelength-Division-Multiplexed Fiber Communications.* Optics and Photonics News, 2001. **12**(3): p. 44 - 48.
6. Gilbert, S.L. and W.C. Swann, *Acetylene $^{12}C_2H_2$ absorption reference for 1510 nm to 1540 nm Wavelength Calibration -- SRM 2517a*, in *Nat. Inst. Stand.Technol. Spec. Publ. 260-133*. 2001.
7. Swann, W.C. and S.L. Gilbert, *Pressure-induced shift and broadening of 1510 - 1540-nm acetylene wavelength calibration lines.* J. Opt. Soc. Am. B., 2000. **17**: p. 1263 - 1270.
8. Swann, W.C. and S.L. Gilbert, *Pressure-induced shift and broadening of 1560 -- 1630-nm carbon monoxide wavelength-calibration lines.* J. Opt. Soc. Am. B, 2002. **19**(10): p. 2461 - 2467.
9. Tuominen, J., et al., *Gas filled photonic bandgap fibers as wavelength references.* Opt. Commun., 2005. **255**: p. 272-277.
10. *EXFO Burleigh wavemeter*. [cited; Available from: http://documents.exfo.com/specsheets/wa-1500-angHR.pdf.
11. Sasada, H. and K. Yamada, *Calibration lines of HCN in the 1.5-micrometer region.* App. Opt., 1990. **29**(24): p. 3535-3547.
12. Konorov, S.O., et al., *Generation of frequency-tunable radiation within the wavelength range of 350-600 nm through nonlinear-optical spectral transformation of femtosecond Cr : forsterite-laser pulses in submicron fused silica threads of a microstructure fiber.* Laser Physics, 2003. **13**(9): p. 1170-1174.

13. Konorov, S.O., et al., *Second- and third-harmonic generation as a local probe for nanocrystal-doped suppressed optical polymer materials with a breakdown threshold.* Optics Communications, 2003. **224**(4-6): p. 309-320.
14. Benabid, F., et al., *Compact, stable and efficient all-fibre gas cells using hollow-core photonic crystal fibres.* Nature, 2005. **434**: p. 488-491.
15. McKinnie, I.T., et al., *Chromium-doped forsterite: The influence of crystal characteristics on laser performance.* Applied Optics, 1996. **35**(21): p. 4159-4165.
16. Gilbert, S.L., W.C. Swann, and C.M. Wang, *Hydrogen cyanide $H^{13}C^{14}N$ absorption reference for 1530 - 1560 nm wavelength calibration - SRM 2519*, in *Nat. Inst. Stand.Technol. Spec. Publ. 260-137*. 1998.
17. Chudoba, C., et al., *All-solid-state Cr : forsterite laser generating 14-fs pulses at 1.3 mu m.* Optics Letters, 2001. **26**(5): p. 292-294.
18. Wei, Z.Y., Y. Kobayashi, and K. Torizuka, *Relative carrier-envelope phase dynamics between passively synchronized Ti : sapphire and Cr : forsterite lasers.* Optics Letters, 2002. **27**(23): p. 2121-2123.
19. Cregan, R.F., et al., *Single-mode photonic band gap guidance of light in air.* Science, 1999. **285**(5433): p. 1537-1539.
20. Benabid, F., et al., *Stimulated Raman Scattering in Hydrogen-Filled Hollow-Core Photonic Crystal Fiber.* Science, 2002. **298**: p. 399.
21. Ritari, T., et al., *Gas sensing using air-guiding photonic bandgap fibers.* Opt. Express, 2004. **12**(17): p. 4081.
22. Benabid, F., et al., *Ultrahigh Efficiency Laser Wavelength Conversion in a Gas-Filled Hollow Core Photonic Crystal Fiber by Pure Stimulated Rotational Raman Scattering in Molecular Hydrogen.* Phys. Rev. Lett., 2004. **93**: p. 123903-1.
23. Ghosh, S., et al., *Resonant optical interactions with molecules confined in photonic band-gap fibers.* Phys. Rev. Lett., 2005. **94**: p. 093902-1.
24. Benabid, F., et al., *Compact, stable and efficient all-fibre gas cells using hollow-core photonic crystal fibres.* Nature, 2005. **434**: p. 488-491.
25. Ghosh, S., et al. *Nonlinear Optical Interactions with Rubidium Atoms Confined in a Hollow-Core Photonic Crystal Fiber*. in *Conference on Lasers and Electro-Optics (CLEO)*. 2006. Long Beach, Calif.: Optical Society of America.

26. Podoleanu, A.G., *Optical coherence tomography.* British Journal of Radiology, 2005. **78**(935): p. 976-988.
27. Svanberg, S., *Some applications of ultrashort laser pulses in biology and medicine.* Measurement Science & Technology, 2001. **12**(11): p. 1777-1783.
28. Petricevic, V., et al., *Laser Action in Chromium-Doped Forsterite.* Applied Physics Letters, 1988. **52**(13): p. 1040-1042.
29. Moncorge, R., et al., *Fluorescence Analysis of Chromium-Doped Forsterite (Mg2sio4).* Ieee Journal of Quantum Electronics, 1991. **27**(1): p. 114-120.
30. Petricevic, V., S.K. Gayen, and R.R. Alfano, *Laser Action in Chromium-Activated Forsterite for near-Infrared Excitation - Is Cr-4+ the Lasing Ion.* Applied Physics Letters, 1988. **53**(26): p. 2590-2592.
31. Jia, W.Y., et al., *Spectroscopy of Cr3+ and Cr4+ Ions in Forsterite.* Physical Review B, 1991. **43**(7): p. 5234-5242.
32. Petricevic, V., S.K. Gayen, and R.R. Alfano, *LASER ACTION IN CHROMIUM-ACTIVATED FORSTERITE FOR NEAR-INFRARED EXCITATION.* Applied Optics, 1988. **27**(20): p. 4162-4163.
33. Sennaroglu, A., *Broadly tunable Cr4+ doped solid-state lasers in the near infrared and visible.* Progress in Quantum Electronics, 2002. **26**(6): p. 287-352.
34. Togashi, T., et al., *High-peak-power femtosecond Cr : forsterite laser system.* Applied Physics B-Lasers and Optics, 1999. **68**(2): p. 169-175.
35. Carrig, T.J. and C.R. Pollock, *Tunable, Cw Operation of a Multiwatt Forsterite Laser.* Optics Letters, 1991. **16**(21): p. 1662-1664.
36. Sennaroglu, A., T.J. Carrig, and C.R. Pollock, *Femtosecond Pulse Generation by Using an Additive-Pulse Mode-Locked Chromium-Doped Forsterite Laser Operated at 77-K.* Optics Letters, 1992. **17**(17): p. 1216-1218.
37. Demos, S.G. and R.R. Alfano, *UP-CONVERTED LUMINESCENCE FROM NONEQUILIBRIUM VIBRONIC STATES OF CR IONS IN FORSTERITE.* Physical Review B, 1992. **46**(14): p. 8811-8815.
38. Seas, A., V. Petricevic, and R.R. Alfano, *Continuous-Wave Mode-Locked Operation of a Chromium-Doped Forsterite Laser.* Optics Letters, 1991. **16**(21): p. 1668-1670.

39. Seas, A., V. Petricevic, and R.R. Alfano, *Generation of Sub-100-Fs Pulses from a Cw Mode-Locked Chromium-Doped Forsterite Laser.* Optics Letters, 1992. **17**(13): p. 937-939.
40. Seas, A., V. Petricevic, and R.R. Alfano, *Self-Mode-Locked Chromium-Doped Forsterite Laser Generates 50-Fs Pulses.* Optics Letters, 1993. **18**(11): p. 891-893.
41. Pang, Y., et al., *Self-Mode-Locked Cr-Forsterite Laser.* Optics Letters, 1993. **18**(14): p. 1168-1170.
42. Yanovsky, V., et al., *Generation of 25-Fs Pulses from a Self-Mode-Locked Cr-Forsterite Laser with Optimized Group-Delay Dispersion.* Optics Letters, 1993. **18**(18): p. 1541-1543.
43. Ivanov, A.A., et al., *Influence of Cr4+ Ion Concentration on Cw Operation of Forsterite Laser and Its Relation to Thermal Problems.* Optics Communications, 1995. **116**(1-3): p. 131-135.
44. Carrig, T.J. and C.R. Pollock, *Performance of a Continuous-Wave Forsterite Laser with Krypton Ion, Ti-Sapphire, and Nd-Yag Pump Lasers.* Ieee Journal of Quantum Electronics, 1993. **29**(11): p. 2835-2844.
45. Sennaroglu, A. and B. Pekerten, *Determination of the optimum absorption coefficient in Cr4+: Forsterite lasers under thermal loading.* Optics Letters, 1998. **23**(5): p. 361-363.
46. Sennaroglu, A. and B. Pekerten, *Experimental and numerical investigation of thermal effects in end-pumped Cr4+: forsterite lasers near room temperature.* Ieee Journal of Quantum Electronics, 1998. **34**(10): p. 1996-2005.
47. Agnesi, A., E. Piccinini, and G. Reali, *Threshold optimization of all-solid-state Cr : forsterite lasers.* Journal of the Optical Society of America B-Optical Physics, 2000. **17**(2): p. 198-201.
48. Sennaroglu, A., *Analysis and optimization of lifetime thermal loading in continuous-wave Cr4+-doped solid-state lasers.* Journal of the Optical Society of America B-Optical Physics, 2001. **18**(11): p. 1578-1586.
49. Sennaroglu, A., et al., *Compact femtosecond lasers based on novel multipass cavities.* Ieee Journal of Quantum Electronics, 2004. **40**(5): p. 519-528.
50. Read, K., et al., *Law-threshold operation of an ultrashort-pulse mode-locked Ti:sapphire laser.* Optics Letters, 1996. **21**(7): p. 489-491.

51. Kowalevicz, A.M., et al., *Ultralow-threshold Kerr-lens mode-locked Ti : Al2O3 laser.* Optics Letters, 2002. **27**(22): p. 2037-2039.
52. Ling, W.J., et al., *Low-threshold self-starting femtosecond Ti : sapphire laser.* Applied Optics, 2006. **45**(11): p. 2495-2498.
53. Sennaroglu, A., F.X. Kaertner, and J.G. Fujimoto, *Low-threshold, room-temperature femtosecond Cr4+: Forsterite laser.* Optics Express, 2007. **15**(20): p. 13043-13048.
54. Geusic, J.E., H.M. Marcos, and L.G. Vanuitert, *Laser Oscillations in Nd-Doped Yttrium Aluminum Yttrium Gallium + Gadolinium Garnets (Continuous Operation of Y3a15o12 Pulsed Operation of Y3ga5o15 + Gd3ga5o12 Rm Temp E).* Applied Physics Letters, 1964. **4**(10): p. 182-&.
55. Behrens, E.G., et al., *Lasing Properties of Chromium-Aluminum-Doped Forsterite Pumped with an Alexandrite Laser.* Ieee Journal of Quantum Electronics, 1991. **27**(8): p. 2042-2049.
56. Sennaroglu, A., *Continuous-wave broadly tunable intracavity frequency-doubled Cr4+: Forsterite laser.* Ieee Journal of Selected Topics in Quantum Electronics, 2002. **8**(3): p. 474-478.
57. Sennaroglu, A., C.R. Pollock, and H. Nathel, *Generation of 48-Fs Pulses and Measurement of Crystal Dispersion by Using a Regeneratively Initiated Self-Mode-Locked Chromium-Doped Forsterite Laser.* Optics Letters, 1993. **18**(10): p. 826-828.
58. Zhang, Z.G., et al., *Self-starting mode-locked femtosecond forsterite laser with a semiconductor saturable-absorber mirror.* Optics Letters, 1997. **22**(13): p. 1006-1008.
59. Sennaroglu, A., C.R. Pollock, and H. Nathel, *Generation of Tunable Femtosecond Pulses in the 1.21-1.27-Mu-M and 605-635 Nm Wavelength Region by Using a Regeneratively Initiated Self-Mode-Locked Crforsterite Laser.* Ieee Journal of Quantum Electronics, 1994. **30**(8): p. 1851-1861.
60. Zhang, Z.G., et al., *Femtosecond Cr:forsterite laser with mode locking initiated by a quantum-well saturable absorber.* Ieee Journal of Quantum Electronics, 1997. **33**(11): p. 1975-1981.
61. Burshtein, Z. and Y. Shimony, *Refractive index dispersion and anisotropy in Cr4+: Mg2SiO4.* Optical Materials, 2002. **20**(2): p. 87-96.

62. Thomann, I., et al., *Chromium-doped forsterite: dispersion measurement with white-light interferometry.* Applied Optics, 2003. **42**(9): p. 1661-1666.
63. Fork, R.L., O.E. Martinez, and J.P. Gordon, *Negative Dispersion Using Pairs of Prisms.* Optics Letters, 1984. **9**(5): p. 150-152.
64. Hanna, D.C., *Astigmatic Gaussian Beams Produced by Axially Asymmetric Laser Cavities.* Ieee Journal of Quantum Electronics, 1969. **Qe 5**(10): p. 483-&.
65. Penzkofer, A., et al., *Kerr lens effects in a folded-cavity four-mirror linear resonator.* Optical and Quantum Electronics, 1996. **28**(4): p. 423-442.
66. Jones, D.J., et al., *Carrier-envelope phase control of femtosecond mode-locked lasers and direct optical frequency synthesis.* Science, 2000. **288**(5466): p. 635-639.
67. Udem, T., et al., *Absolute frequency measurements of the Hg+ and Ca optical clock transitions with a femtosecond laser.* Physical Review Letters, 2001. **86**(22): p. 4996-4999.
68. Udem, T., R. Holzwarth, and T.W. Hansch, *Optical frequency metrology.* Nature, 2002. **416**(6877): p. 233-237.
69. Morgner, U., et al., *Nonlinear optics with phase-controlled pulses in the sub-two-cycle regime.* Physical Review Letters, 2001. **86**(24): p. 5462-5465.
70. Ell, R., et al., *Generation of 5-fs pulses and octave-spanning spectra directly from a Ti : sapphire laser.* Optics Letters, 2001. **26**(6): p. 373-375.
71. Fortier, T.M., D.J. Jones, and S.T. Cundiff, *Phase stabilization of an octave-spanning Ti : sapphire laser.* Optics Letters, 2003. **28**(22): p. 2198-2200.
72. Matos, L., et al., *Direct frequency comb generation from an octave-spanning, prismless Ti : sapphire laser.* Optics Letters, 2004. **29**(14): p. 1683-1685.
73. Hils, D. and J.L. Hall, *Improved Kennedy-Thorndike Experiment to Test Special Relativity.* Physical Review Letters, 1990. **64**(15): p. 1697-1700.
74. Fritschel, P., et al., *High power interferometric phase measurement limited by quantum noise and application to detection of gravitational waves.* Physical Review Letters, 1998. **80**(15): p. 3181-3184.
75. Prestage, J.D., R.L. Tjoelker, and L. Maleki, *Atomic Clocks and Variations of the Fine-Structure Constant.* Physical Review Letters, 1995. **74**(18): p. 3511-3514.

76. Mabuchi, H., J. Ye, and H.J. Kimble, *Full observation of single-atom dynamics in cavity QED.* Applied Physics B-Lasers and Optics, 1999. **68**(6): p. 1095-1108.
77. Sakai, Y., S. Sudo, and T. Ikegami, *Frequency Stabilization of Laser-Diodes Using 1.51-1.55 Mu-M Absorption-Lines of (C2h2)-C-12 and (C2h2)-C-13.* Ieee Journal of Quantum Electronics, 1992. **28**(1): p. 75-81.
78. Margolis, H.S., et al., *Hertz-level measurement of the optical clock frequency in a single Sr-88(+) ion.* Science, 2004. **306**(5700): p. 1355-1358.
79. Diddams, S.A., et al., *An optical clock based on a single trapped Hg-199(+) ion.* Science, 2001. **293**(5531): p. 825-828.
80. Ye, J., L.S. Ma, and J.L. Hall, *Molecular iodine clock.* Physical Review Letters, 2001. **87**(27): p. -.
81. Jost, J.D., J.L. Hall, and J. Ye, *Continuously tunable, precise, single frequency optical signal generator.* Optics Express, 2002. **10**(12): p. 515-520.
82. Baltuska, A., T. Fuji, and T. Kobayashi, *Controlling the carrier-envelope phase of ultrashort light pulses with optical parametric amplifiers.* Physical Review Letters, 2002. **88**(13): p. -.
83. Shelton, R.K., et al., *Phase-coherent optical pulse synthesis from separate femtosecond lasers.* Science, 2001. **293**(5533): p. 1286-1289.
84. Baltuska, A., et al., *Attosecond control of electronic processes by intense light fields.* Nature, 2003. **421**(6923): p. 611-615.
85. Holman, K.W., et al., *Detailed studies and control of intensity-related dynamics of femtosecond frequency combs from mode-locked Ti : sapphire lasers.* Ieee Journal of Selected Topics in Quantum Electronics, 2003. **9**(4): p. 1018-1024.
86. Holman, K.W., et al., *Intensity-related dynamics of femtosecond frequency combs.* Optics Letters, 2003. **28**(10): p. 851-853.
87. Kim, K., et al., *Stabilized frequency comb with a self-referenced femtosecond Cr : forsterite laser.* Optics Letters, 2005. **30**(8): p. 932-934.
88. Thapa, R., et al. *Phase-stabilized Prism-based Cr:forsterite Laser Frequency Comb for Absolute Frequency Measurements*. in *Conference on Lasers and Electro-Optics*. 2007. Baltimore, MD: Optical Society of America.

89. Thomann, I., et al., *420-MHz Cr : forsterite femtosecond ring laser and continuum generation in the 1-2-mu m range.* Optics Letters, 2003. **28**(15): p. 1368-1370.
90. Corwin, K.L., et al., *Absolute-frequency measurements with a stabilized near-infrared optical frequency comb from a Cr : forsterite laser.* Optics Letters, 2004. **29**(4): p. 397-399.
91. Helbing, F.W., et al., *Carrier-envelope offset dynamics of mode-locked lasers.* Optics Letters, 2002. **27**(3): p. 194-196.
92. Nicholson, J.W., et al., *All-fiber, octave-spanning supercontinuum.* Optics Letters, 2003. **28**(8): p. 643-645.
93. Washburn, B.R., W.C. Swann, and N.R. Newbury, *Response dynamics of the frequency comb output from a femtosecond fiber laser.* Optics Express, 2005. **13**(26): p. 10622-10633.
94. Scott, R.P., et al., *Amplitude and phase noise sensitivity of modelocked Ti : sapphire lasers in terms of a complex noise transfer function.* Optics Express, 2007. **15**(14): p. 9090-9095.
95. McFerran, J.J., et al., *Suppression of pump-induced frequency noise in fiber-laser frequency combs leading to sub-radian f (ceo) phase excursions.* Applied Physics B-Lasers and Optics, 2007. **86**(2): p. 219-227.
96. McFerran, J.J., et al., *Elimination of pump-induced frequency jitter on fiber-laser frequency combs.* Optics Letters, 2006. **31**(13): p. 1997-1999.
97. Newbury, N.R. and B.R. Washburn, *Theory of the frequency comb output from a femtosecond fiber laser.* Ieee Journal of Quantum Electronics, 2005. **41**(11): p. 1388-1402.
98. Newbury, N.R. and W.C. Swann, *Low-noise fiber-laser frequency combs (Invited).* Journal of the Optical Society of America B-Optical Physics, 2007. **24**(8): p. 1756-1770.
99. Swann, W.C. and S.L. Gilbert, *Pressure-induced shift and broadening of 1510 - 1540-nm acetylene wavelength calibration lines.* J. Opt. Soc. Am. B, 2000. **17**(7): p. 1263 - 1270.
100. Labachelerie, M.d., K. Nakagawa, and M. Ohtsu, *Ultranarrow $^{13}C_2H_2$ saturated-absorption lines at 1.5 μm.* Opt. Lett., 1994. **19**(11): p. 840 - 842.
101. Nakagawa, K., et al., *Accurate optical frequency atlas of the 1.5-μm bands of acetylene.* J. Opt. Soc. Am. B, 1996. **13**(12): p. 2718 - 2714.

102. Onae, A., et al., *Optical frequency link between an acetylene stabilized laser at 1542 nm and an Rb stabilized laser at 778 nm using a two-color mode-locked fiber laser.* Optics Communications, 2000. **183**(1-4): p. 181-187.

103. Onae, A., et al. *Optical Frequency Standard at 1.5 μm based on Doppler-free acetylene absorption*. in *6th Sypm on Frequency Standards and Metrology*. 2002: World Scientific, Singapore.

104. Quinn, T.J., *Practical realization of the definition of the metre, including recommended radiations of other optical frequency standards (2001).* Metrologia, 2003. **40**: p. 103.

105. Hong, F.-L., et al., *Absolute frequency measurement of an acetylene-stabilized laser at 1542 nm.* Opt. Lett., 2003. **28**(23): p. 2324-2326.

106. Jiang, J., et al., *Frequency measurement of acetylene-stabilized lasers using a femtosecond optical comb without carrier-envelope offset frequency control.* Optics Express, 2005. **13**(6): p. 1958-1965.

107. Edwards, C.S., et al., *Absolute frequency measurement of a 1.5-μm acetylene standard by use of a combined frequency chain and femtosecond comb.* Opt. Lett., 2004. **29**(6): p. 566-568.

108. Czajkowski, A., et al., *Absolute frequency measurement of acetylene transitions in the region of 1540 nm.* Applied Physics B-Lasers and Optics, 2004. **79**(1): p. 45-50.

109. Czajkowski, A., A.A. Madej, and P. Dube, *Development and study of a 1.5 μm optical frequency standard referenced to the P(16) saturated absorption line in the (v(1)+v(3)) overtone band of $^{13}C_2H_2$.* Optics Communications, 2004. **234**(1-6): p. 259-268.

110. Edwards, C.S., et al., *High-accuracy frequency atlas of $^{13}C_2H_2$ in the 1.5 μm region.* Applied Physics B-Lasers And Optics, 2005. **80**(8): p. 977-983.

111. Onae, A., et al., *Saturation spectroscopy of an acetylene molecule in the 1550 nm region using an erbium doped fiber amplifier.* Optics Communications, 1997. **142**(1-3): p. 41-44.

112. Ritari, T., et al., *Gas sensing using air-guiding photonic bandgap fibers.* Optics Express, 2004. **12**(17): p. 4081.

113. Ghosh, S., et al., *Resonant Optical Interactions with Molecules Confined in Photonic Band-Gap Fibers.* Phys. Rev. Lett., 2005. **94**: p. 093902.

114. Benabid, F., et al., *Electromagnetically-induced transparency grid in acetylene-filled hollow-core PCF.* Optics Express, 2005. **13**(15): p. 5694-5703.
115. Faheem, M., R. Thapa, and K.L. Corwin. *"Spectral Hole Burning of Acetylene Gas inside a Photonic Bandgap Optical Fiber"*. in *Conference on Lasers and Electro-optics*. 2005. Baltimore, MD: Optical Society of America.
116. Henningsen, J., J. Hald, and J.C. Petersen, *Saturated absorption in acetylene and hydrogen cyanide in hollow-core photonic bandgap fibers.* Optics Express, 2005. **13**(26): p. 10475-10482.
117. Demtröder, W., *Laser Spectroscopy*. 1996: Springer.
118. West, J.A., et al., *Surface modes in air-core photonic band-gap fibers.* Opt. Express, 2004. **12**(8): p. 1485-1496.
119. Henningsen, J., J. Hald, and J.C. Petersen, *Saturated absorption in acetylene and hydrogen cyanide in hollow-core photonic bandgap fibers.* Optics Express, 2005. **13**(26): p. 10475.
120. Couny, F., F. Benabid, and P.S. Light, *Large-pitch kagome-structured hollow-core photonic crystal fiber.* Opt. Lett., 2006. **31**(24): p. 3574-3576.
121. Light, P.S., et al., *Electromagnetically induced ransparency in Rb-filled coated hollow-core photonic crystal fiber.* Opt. Lett., 2007. **32**(10): p. 1323.
122. Benabid, F., et al., *Electromagnetically-induced transparency grid in acetylene-filled hollow-core PCF.* Opt. Express, 2005. **13**(15): p. 5694-5703.
123. Henningsen, J., J. Hald, and J.C. Peterson, *Saturated absorption in acetylene and hydrogen cyanide in hollow-core photonic bandgap fibers.* Opt. Express, 2005. **13**(26): p. 10475-10482.
124. Thapa, R., et al., *Saturated absorption spectroscopy of acetylene gas inside large-core photonic bandgap fiber.* Opt. Lett., 2006. **31**(16): p. 2489-2491.
125. Ritari, T., et al., *Gas sensing using air-guiding photonic bandgap fibers.* Opt. Express, 2004. **12**: p. 4081.
126. Ritari, T., G. Genty, and H. Ludvigsen, *Supercontinuum and gas cell in a single microstructured fiber cell.* Opt. Lett., 2005. **30**(24): p. 3380-3382.
127. Yablon, A., *Optical fiber fusion splicing*, ed. W.T. Rhodes. 2005, Heidelberg: Springer.

128. Light, P.S., F. Couny, and F. Benabid, *Low optical insertion-loss and vacuum-pressure all-fiber acetylene cell based on hollow core PCF.* Opt. Lett., 2006. **31**.
129. Bennet, P.J., T.M. Monro, and D.J. Richardson, *Toward practical holey fiber technology: fabrication, splicing, modeling, and characterization.* Opt. Lett., 1999. **24**(17): p. 1203-1205.
130. Bourliaguet, B., et al., *Microstructured fiber splicing.* Opt. Express, 2003. **11**(25): p. 3412-3417.
131. A/S, C.F. *Crystal Fibre A/S*. 2006 [cited; Available from: http://www.crystal-fibre.com/support/faq.shtm.
132. Xiao, L., et al., *Fabrication of selective injection microstructured optical fibers with a conventional fusion splicer.* Opt. Express, 2005. **13**(22): p. 9014-9022.
133. Corning, I. *Corning SMF-28e optical fiber product information*. 2006 [cited; Available from: http://www.corning.com/opticalfiber/.
134. A/S, C.F. *Crystal Fibre A/S HC19-1550-01 product information*. 2006 [cited; Available from: http://www.crystal-fibre.com.
135. A/S, C.F. *Crystal Fibre A/S HC-1550-02 product information*. 2006 [cited; Available from: http://www.crystal-fibre.com.
136. Chong, J.H. and M.K. Rao, *Development of a system for laser splicing photonic crystal fiber.* Opt. Express, 2003. **11**(12): p. 1365-1370.
137. Gloge, D., *Weakly guiding fibers.* Appl. Opt., 1971. **10**(10): p. 2252-8.
138. Pollack, C.R., *Fundamentals of Optoelectronics*. 1995, Chicago: Irwin.
139. Kweon, G.-i. and I.-s. Park, *Splicing losses between dissimilar optical waveguides.* J of Lightwave Tech, 1999. **17**(4): p. 690-703.
140. Weel, M. and A. Kumarakrishnan, *Laser-frequency stabilization using a lock-in amplifier.* Canadian Journal of Physics, 2002. **80**(12): p. 1449-1458.
141. Drever, R.W.P., et al., *Laser Phase and Frequency Stabilization Using an Optical-Resonator.* Applied Physics B-Photophysics and Laser Chemistry, 1983. **31**(2): p. 97-105.
142. Pound, R.V., *Electronic Frequency Stabilization of Microwave Oscillators.* Review of Scientific Instruments, 1946. **17**(11): p. 490-505.

143. Bjorklund, G.C., et al., *Frequency-Modulation (Fm) Spectroscopy - Theory of Lineshapes and Signal-to-Noise Analysis.* Applied Physics B-Photophysics and Laser Chemistry, 1983. **32**(3): p. 145-152.

144. Udem, T., et al., *Absolute optical frequency measurement of the cesium D-1 line with a mode-locked laser.* Physical Review Letters, 1999. **82**(18): p. 3568-3571.

145. Udem, T., et al., *Accurate measurement of large optical frequency differences with a mode-locked laser.* Optics Letters, 1999. **24**(13): p. 881-883.

146. Holzwarth, R., et al., *Optical frequency synthesizer for precision spectroscopy.* Physical Review Letters, 2000. **85**(11): p. 2264-2267.

147. Stenger, J., et al., *Ultraprecise measurement of optical frequency ratios.* Physical Review Letters, 2002. **88**(7): p. -.

148. Zimmermann, M., et al., *Optical clockwork with an offset-free difference-frequency comb: accuracy of sum- and difference-frequency generation.* Optics Letters, 2004. **29**(3): p. 310-312.

149. Fox, R.W., et al., *Optical frequency measurements with the global positioning system: tests with an iodine-stabilized He-Ne laser.* Applied Optics, 2005. **44**(1): p. 113-120.

150. Levine, J., *Time and frequency distribution using satellites.* Reports on Progress in Physics, 2002. **65**(8): p. 1119-1164.

151. Felder, R., *Practical realization of the definition of the metre, including recommended radiations of other optical frequency standards (2003).* Metrologia, 2005. **42**(4): p. 323-325.

152. Sarah L. Gilbert, W.C.S., *Acetylene $_{12}C_2H_2$ Absormtion Reference for 1510 nm to 1540 nam Wavelength Calibration-SRM 2517a.* 2001.

153. Delabachelerie, M., et al., *High-Frequency-Stability Laser at 1.5 Mu-M Using Doppler-Free Molecular Lines.* Optics Letters, 1995. **20**(6): p. 572-574.

154. Czajkowski, A., A.A. Madej, and P. Dube, *Development and study of a 1.5 mu m optical frequency standard referenced to the P(16) saturated absorption line in the (v(1)+v(3)) overtone band of (C2H2)-C-13.* Optics Communications, 2004. **234**(1-6): p. 259-268.

155. Edwards, C.S., et al., *High-precision frequency measurements of the v(1) + v(3) combination band of (C2H2)-C-12 in the 1.5 mu m region.* Journal of Molecular Spectroscopy, 2005. **234**(1): p. 143-148.

156. Madej, A.A., et al., *Accurate absolute reference frequencies from 1511 to 1545 nm of the v(1)+v(3) band of (C2H2)-C-12 determined with laser frequency comb interval measurements.* Journal of the Optical Society of America B-Optical Physics, 2006. **23**(10): p. 2200-2208.

157. Madej, A.A., et al., *Accurate absolute frequencies of the nu(1) + nu(3) band of (C2H2)-C-13 determined using an infrared inode-locked Cr : YAG laser frequency comb.* Journal of the Optical Society of America B-Optical Physics, 2006. **23**(4): p. 741-749.

158. Jiang, J., et al., *Measurement of acetylene-d absorption lines with a self-referenced fiber laser frequency comb.* Journal of the Optical Society of America B-Optical Physics, 2007. **24**(10): p. 2727-2735.

159. Moon, H.S., W.K. Lee, and H.S. Suh, *Absolute-frequency measurement of an acetylene-stabilized laser locked to the P(16) transition of (C2H2)-C-13 using an optical-frequency comb.* Ieee Transactions on Instrumentation and Measurement, 2007. **56**(2): p. 509-512.

160. Musha, M., et al., *Practical optical frequency measurement system around 1.5 mu m based on an acetylene-stabilized laser-locked optical frequency comb.* Optics Communications, 2007. **272**(1): p. 211-216.

161. Balling, P. and P. Kren, *Absolute frequency measurements of wavelength standards 532 nm, 543 nm, 633 nm and 1540 nm.* European Physical Journal D, 2008. **48**(1): p. 3-10.

162. Inaba, H., et al., *Long-term measurement of optical frequencies using a simple, robust and low-noise fiber based frequency comb.* Optics Express, 2006. **14**(12): p. 5223-5231.

163. Ryu, H.Y., et al., *Absolute frequency measurement of an acetylene stabilized laser using a selected single mode from a femtosecond fiber laser comb.* Optics Express, 2008. **16**(5): p. 2867-2873.

164. Ma, L.S., et al., *A new method to determine the absolute mode number of a mode-locked femtosecond-laser comb used for absolute optical frequency measurements.* Ieee Journal of Selected Topics in Quantum Electronics, 2003. **9**(4): p. 1066-1071.

165. Nakagawa, K., et al., *Accurate optical frequency atlas of the 1.5-mu m bands of acetylene.* Journal of the Optical Society of America B-Optical Physics, 1996. **13**(12): p. 2708-2714.